SYNTHESIS AND CHARACTERIZATION OF 2D MATERIALS FOR SENSING APPLICATION

THESIS

Submitted to

Delhi Technological University

In fulfillment of the requirements for the degree of

DOCTOR OF PHILOSOPHY

in

PHYSICS

By

PRIYA

(2K18/PHDAP/501)

Under the Supervision of

Prof. Vinod Singh

DEPARTMENT OF APPLIED PHYSICS

DELHI TECHNOLOGICAL UNIVERSITY

DELHI-110042, INDIA

2024

Dedication

This dissertation is dedicated to my husband.

DELHI TECHNOLOGICAL UNIVERSITY

(Govt. of National Capital Territory of Delhi)

Shahbad Daulatpur, Bawana Road, Delhi-110042

CERTIFICATE

This is to certify that the thesis entitled **"Synthesis and Characterization of 2D Materials for Sensing Application"** submitted by **Ms. Priya (2K18/PHDAP/501)** to Delhi Technological University (DTU), Delhi, India for the degree of Doctor of Philosophy, is a bonafide record of the research work carried out by her under my supervision and guidance. This work embodied in this thesis has been carried out in the Nanofabrication Laboratory (NFL), Department of Applied Physics, Delhi Technological University (DTU), Delhi, India. This work of this thesis is original and has not been submitted in parts or fully to any other institute or University for the award of any other degree or diploma.

Prof. Vinod Singh
Supervisor
Delhi Technological University
Delhi-10042, India

Prof. A.S. Rao
Head of the Department
Department of Applied Physics
Delhi Technological University

DELHI TECHNOLOGICAL UNIVERSITY

(Govt. of National Capital Territory of Delhi)

Shahbad Daulatpur, Bawana Road, Delhi-110042

CANDIDATE'S DECLARATION

I, **Ms. Priya**, hereby certify that the thesis entitled ***"Synthesis and Characterization of 2D Materials for Sensing Application"*** submitted in the fulfillment of the requirements for the award of the degree of Doctor of Philosophy is an authentic record of my research work carried out under the supervision of **Prof. Vinod Singh.** This work in the same form or any other form has not been submitted by me or anyone else earlier for any purpose. Any material borrowed or referred to is duly acknowledged.

Priya
(2K18/PHDAP/501)
Department of Applied Physics
Delhi Technological University
Delhi-110042, India

ACKNOWLEDGEMENTS

The journey of this PhD thesis might have been a flight of fancy without the support and contribution of many inspiring people who contributed to achieving my goal. I hope this acknowledgment serves as a token of my deep gratitude and appreciation to everyone who helped me through this journey.

Primarily, I owe it all to the Almighty God for granting me the wisdom, health, and strength to complete this task and enabling me to complete it.

I wish to acknowledge my sincere gratitude towards my supervisor **Prof. Vinod Singh**, for his valuable support, patience, and guidance throughout the entire duration of this project. His positivity and plentiful experience have encouraged me in all the time of my academic research and daily life. He has always been so keen to help me in every possible way to expand my academic network and provide a free hand to navigate new experiences which has been really helpful in my professional growth. The allegiance with which he handles such a large group, always willing to accept new ideas, and provides support to implement them is highly motivational. He has always motivated me and has given me moral support during my thesis work.

I would like to extend my sincere gratitude to **Hon'ble Vice Chancellor, DTU**, and other officials for their valuable support and for providing the research environment and financial assistance during my PhD journey. I would also thank **Prof. Rinku Sharma**, Dean (Academic-PG), DTU, **Prof. A.S. Rao**, Head of the Department of Applied Physics, DTU, and all other faculty and staff members for their help and cooperation during my research. Thanks to the Department of Applied Physics, Delhi Technological University (DTU), for providing the research facilities so that I can work within the time limit.

I am also grateful to **Dr. Bharti Singh** for her valuable guidance and the insightful discussion she shared during my research work.

I feel fortunate to be associated with Nano Fabrication Laboratory (NFL), which brings along an immense history of research and innovation and for this, I express my thanks

to my fellow lab mates **Dr. Umang, Jasveer Singh, Naima, Ramesh Kumar, Shivani, Praveen Kumar, Surya Pratap, and Ankita** for the selfless support and for providing me with the environment around, that kept me going in this challenging yet beautiful journey.

A special thanks to all my friends within and outside DTU for keeping me sane. To my DTU companions: **Dr. Vishal Singh, Shivani, Sharad, Vinay, and Naveen**, a heartfelt thanks to you, without you I wouldn't have enjoyed this journey. I extend a special heartfelt thanks to **Shivani** for consistently being there and assisting me with strength at every possible step throughout these years. She made me cherish every moment and achievement in every possible way with her presence and positivity. To **Dalip Saini**, you are a gem, and thank you for always being there to support me! I would also thank my colleagues and hostel mates **Km. Komal, Jyoti, and Durvesh** for their endearing presence and fun times which I will cherish forever.

I express my heartfelt gratitude to **Prof. Mahesh Kumar**, Department of Electrical Engineering, IIT Jodhpur, for providing me necessary facilities and **Mr. Sumit Kumar**, IIT Jodhpur for the needful assistance. I would also like to thank **Dr. Prashant Bisht** (Post Doctoral Fellow, Sungkyunkwan University, South Korea) for all his help with scientific discussions.

I am very grateful to my grandfather, **Mr. Suraj Bhan Yadav,** and my grandmother **Mrs. Vidya Devi** for always encouraging me to do better throughout my journey and in life. I want to pay high regard to my father, **Mr. Pradeep Kumar Yadav**, and my mother. **Mrs. Krishna Devi** for being the significant pillar of strength and motivation with constant care during these years. I would like to express my deep gratitude towards my parents for always supporting me in everything and providing the best facilities possible for me to reach there. I would not have made this far without their belief and confidence in me. A big thanks to my siblings **Ms. Pooja Yadav** and **Mr. Yaduvender Yadav** who encouraged and helped me at every stage of my personal and academic life and longed to see this achievement come true. I would also express my special thanks to my nephew **Akshat** and niece **Aarunya** for their company which was an important support to relieve any stress during this journey. My deep and sincere thanks to my

father-in-law **(Mr. Omprakash Yadav)** and my mother-in-law **(Mrs. Rajbala)** for always being there for me as a consistent support and strength, this journey would not have been possible without their encouragement. I am forever indebted to them for giving me the opportunities and believing in my belief. And, I would like to express my deep gratefulness and thanks to my son, **Anantvijay,** for being a clandestine supporter in my last fine moments of this journey.

Lastly, I wish to extend heartfelt thanks and gratitude to my husband, **Mr. Amit Kumar Yadav**, for his enduring affection, support, and patience. I am grateful to him for believing in me long after I had lost belief in myself, this accomplishment honestly would have been impossible without his unrelenting support and the sacrifices he has made in the past few years. His support has been the greatest source of encouragement throughout my doctorate journey.

Priya

ABSTRACT

Rapid industrialization and urbanization are causing harm to the environment and human health owing to the emission of harmful gases. The fast detection of the emission of such harmful gases and the emitted concentration has become an important task that has brought high-performance gas sensors into huge demand. Most gas sensors work efficiently at higher operating temperatures, which also require higher power consumption and degrade the sensor quality after some time. However, the majority of the existing gas sensors suffer from poor selectivity and low portability. Advances in low-powered gas sensors, wireless sensors, and miniaturization of gas sensing technology have attracted the attention of the digital world. Over the last decade, researchers have been working on many new materials and have discovered several new materials for developing efficient gas sensors. Metal oxides have been the most widely used materials for commercial gas sensing, but high-temperature operation has been the major setback in their commercial applications. In addition, two-dimensional (2D) materials have emerged as new and improved sensing materials owing to their inherited chemical, physical, and electronic properties. 2D materials especially transition metal dichalcogenides (TMDCs) based gas sensors are currently gaining considerable attention because of their longer environmental stability and ambient conditions; however, the low limit of detection and longer response and recovery times are still issues. To overcome these issues, when a 2D material is coupled with another 2D material such as a metal oxide or metal, the combined effects of these two materials appear. This combined effect demonstrates the possibility of improving the sensing performance of gas sensors by forming hybrid nanostructures. The present thesis involves the synthesis of nanocomposites based on 2D materials with metal oxides and other dimensional materials, and subsequent investigations have been performed on their utilization in gas detection.

For this purpose, a hydrothermal method was primarily used to synthesize large-area, few-layered nanostructures and to synthesize the nanocomposites thermal vapor deposited was also employed. These materials mainly belong to distinct families of 2D materials, namely transition metal dichalcogenide (MoS_2), and transition metal oxides (MoO_3 and SnO_2). Active carbon black (CB) was synthesized using chemical vapor deposition (CVD). MoS_2 with different nanocomposites was synthesized, and the effect of SnO_2, MoO_3, and MoS_2-

based composites, on the sensing performance of the fabricated gas sensors was investigated to achieve highly selective sensors at ambient conditions for NO_2 and NH_3 gases.

To begin with, a mixed phase of 1T/2H-MoS_2 has been synthesized with varying concentrations of Mo precursor in order of 1 M, 1.4 M, and 1.8 M using NH^{4+} intercalation by keeping the other experimental conditions the same. out of all the prepared nanostructures, 1.8M-1T/2H-MoS_2 showed the maximum 1T character, indicating a higher amount of metallic character with a 1.5 eV bandgap. This enhancement in the 1T character and decrease in the bandgap value were achieved by increasing the concentration of NH^{4+} ions in the solution. The enhanced metallic character was also responsible for the enhanced optical absorption, indicating a direct excitonic transition from the valence band to the conduction band. Because 1T-MoS_2 is not environmentally stable, the synthesis of mixed 1T/2H-MoS_2 with a higher 1T character without any external aid is a good result. The variation in the morphology corresponding to the mixed phase also increased the surface-to-volume ratio and available active sites, which could be suitable for gas sensing.

After studying the properties of the mixed phase of MoS_2, the effect of SnO_2 nanoparticles on the gas-sensing properties of MoS_2 nanosheets was studied. Then to further improve the sensing performance, the active carbon black was also incorporated in SnO_2/MoS_2 and the output performance of the device was determined. To determine the optimum concentration of the SnO_2, we have synthesized the different nanostructures with varying weight percentages of SnO_2 (0.6 %, 0.8%, and 1%). Based on microstructural and electronic properties, MoS_2/SnO_2 with 0.8 % concentration was chosen as suitable for studying gas sensing performance. Further, different devices based on bare MoS_2, SnO_2/MoS_2, and CB/SnO_2/MoS_2 were fabricated and their gas-sensing properties for NO_2 around room temperature were evaluated. The gas sensing response of MoS_2 for NO_2 gas was found to be increased due to the incorporation of SnO_2. Further, the ternary heterostructure interface of CB/SnO_2/MoS_2 also showed an increased and effective adsorption of NO_2 gas molecules. The ternary hetero-interface of the CB/SnO_2/MoS_2 sensor showed a maximum sensing response of around 46 % for 100 ppm of NO_2 gas, which is higher than the binary heterojunction of SnO_2/MoS_2 (43%) and bare MoS_2 (42 %). Along with better sensor response, the response (26 s) and recovery times (73 s) are also faster than SnO_2/MoS_2 heterostructure and bare MoS_2. This enhanced sensing performance of CB/SnO_2/MoS_2 is

dedicated to the p-n heterojunctions and Schottky barriers generation at the interface, which has been justified by the electrical measurements.

To further determine the efficiency of MoS_2-based gas sensors with other oxides, MoS_2/MoO_3 heterostructures were synthesized with different reducing agents using the hydrothermal method and followed by thermal annealing in an Ar environment at 500 ˚C for 1h. The hydrothermal synthesis at 200 ˚C resulted in MoO_xS_y, which was confirmed by XRD and then thermal annealing was performed at 300˚ and 500 ˚C. The better crystallinity and identified phases were obtained at 500 ˚C and used further for gas sensing studies. In this work, the gas sensing properties of different MoS_2:MoO_3-based gas sensors have been studied and it turned out that MoS_2:MoO_3 based sensors showed dual detection for NO_2 and NH_3 gases. Here, three different heterostructures were prepared using hydrazine hydrate (HH-MoS_2:MoO_3), L-ascorbic acid (LA-MoS_2:MoO_3), and without reducing agent (MoS_2:MoO_3). The MoS_2:MoO_3-based sensor showed n-type sensing behavior dominated by MoO_3 charge carriers for NH_3 gas, whereas the same sensor showed p-type sensing behavior on exposure to NO_2 gas. The HH-MoS_2:MoO_3 showed higher adsorption sites and more active sites resulting in a higher response for NH_3 and NO_2 gases but the incomplete recovery and longer recovery time proved to be the major drawbacks for this sensor. Besides that, MoS_2:MoO_3 showed a good sensing response for 5 ppm concentration of NO_2 (36 %) and NH_3 (52.3 %) gas with complete recovery and good response time. More importantly, one sensing surface has contributed to the selective detection of NO_2 and NH_3 at 50˚C with different sensing behavior. Interestingly, different conducting channels and adsorption sites play an important role in opposite sensing behavior, possibly due to the synergistic effects at the heterojunction interface. Here, in this work, the effect of different reducing agents on various MoS_2:MoO_3 based sensors has resulted in the availability of different adsorption sites and different morphology. It has been proved that HH-MoS_2:MoO_3 heterostructures are more prone to oxidation and clearly show higher response, but rapid oxidation may be the major cause of incomplete recovery. In contrast, MoS_2:MoO_3 contained the least sulfur vacancies on the surface, which played an important role in the complete recovery.

LIST OF PUBLICATIONS

Publications in Peer-Reviewed Journals:

1. **Priya Pradeep Kumar** and Vinod Singh, "Enhanced dual gas sensing performance of MoS_2/MoO_3 nanostructures for NH_3 and NO_2 detection", *Ceramics International*, Volume 50, Issue 12, 15 June 2024.

2. **Priya Pradeep Kumar,** Sumit Kumar, Mahesh Kumar, and Vinod Singh, "Utilization of Active Carbon Black with SnO_2/MoS_2 Nanocomposites for the Efficient Detection of NO_2 Molecules", *IEEE Sensors Journal*, Vol. 23, No. 23, 1 December 2023.

3. **Priya Pradeep Kumar** and Vinod Singh, "Effect of Precursors' Concentration on Structural and Electronic Properties of Ammonium Ions (NH^{4+}) Intercalated 1T/2H Phase MoS_2", *Indian Journal of Engineering & Materials Sciences*, Vol. 30, October 2023, pp. 719-723.

Publication not included in this thesis:

4. Vinod Singh, Pawan K. Kulriya, Ashok Kumar, Ramesh Kumar, **Priya Pradeep Kumar,** Umang Berwal, Jasveer Singh, Kailash Chandra, Kedar Singh, "Hydrogen induced structural modifications in size selected Pd-Carbon core-shell NPs: Effect of carbon shell thickness, size and pressure", *International Journal of Hydrogen Energy,* Volume 47, Issue 25, 22 March 2022, Pages 12642-12652

Publications in Conferences:

1. Vinay Yadav, **Priya Pradeep Kumar** and Vinod Singh, "Effect of different precursors on the morphology of CVD synthesized $MoSe_2$", Materials Today: Proceedings, (2021), 56(7).

2. **Priya Pradeep Kumar** and Vinod Singh, "Investigation of Microstructural, Optical, and Electronic Properties of Hydrothermally Synthesized MoS_2 Decorated SnO_2", Recent Advances in Nanomaterials, November 2023, http://dx.doi.org/10.1007/978-981-99-4878-9_1 **(Book Chapter)**

3. **Priya Pradeep Kumar** and Vinod Singh, "Selective Detection of NH_3 using MoS_2/MoO_3 Nanocomposites Around Room Temperature", Communicated in Springer Nature.

Conference-Poster Presentations:

1. **Priya Pradeep Kumar** and Vinod Singh, "Selective Detection of NH_3 using MoS_2/MoO_3 Nanocomposites Around Room Temperature", ICAMNOP 2023, at Delhi Technological University, Delhi, 20^{th} - 22nd December 2023.
2. **Priya Pradeep Kumar** and Vinod Singh, "Effect of Precursors' Concentration on Structural and Electronic Properties of Ammonium Ions (NH^{4+}) Intercalated 1T/2H Phase MoS_2", ICAMET-2023, at Netaji Subhash University of Technology, New Delhi, 4^{th}-6^{th} May 2023.
3. **Priya Pradeep Kumar** and Vinod Singh, "Investigation of Microstructural and Optical Properties of hydrothermally synthesized SnO_2 decorated MoS_2 nanosheets", IUMRS-ICA 2022, Indian Institute of Technology Jodhpur, India, 19^{th} -23^{rd} December 2022.
4. **Priya Pradeep Kumar** and Vinod Singh, "Investigation of Microstructural, Electronic and Optical Properties of hydrothermally synthesized SnO_2 decorated MoS_2 nanosheets", International Conference on Nanotechnology: opportunities and challenges (ICNOC-2022), Department of Applied Sciences & Humanities, Faculty of Engineering & Technology, Jamia Millia Islamia, New Delhi, India, 28^{th}-30^{th} November 2022.

TABLE OF CONTENTS

LIST OF FIGURES

LIST OF TABLES

LIST OF ABBREVIATIONS

Acronyms	**:**	**Meaning**
NO_x	:	Nitrogen Oxide Derivatives
NH_3	:	Ammonia
H_2	:	Hydrogen
SO_2	:	Sulfur Dioxide
CH_2O	:	Formaldehyde
MOS	:	Metal Oxide Semiconductors
MO_x	:	Metal Oxides
2D	:	Two Dimensional
TMDC	:	Transition Metal Dichalcogenides
MoS_2	:	Molybdenum Disulfide
SnO_2	:	Tin Oxide
CB	:	Active Carbon Black
MoO_3	:	Molybdenum Trioxide
HH	:	Hydrazine Hydrate
LA	:	L-ascorbic acid
$MoSe_2$	:	Molybdenum Diselenide
R_g	:	Resistance in the Presence of Gas
R_a	:	Resistance in Air
τ_{res}	:	Response Time
$\tau_{recovery}$	:	Recovery Time
SiO_2	:	Silicon Dioxide
Si	:	Silicon
ppm	:	Parts Per Million
rpm	:	Revolutions Per Minute
M	:	Molar Concentration
wt%	:	Weight Percentage

Chapter – 1
Introduction

CHAPTER – 1

INTRODUCTION

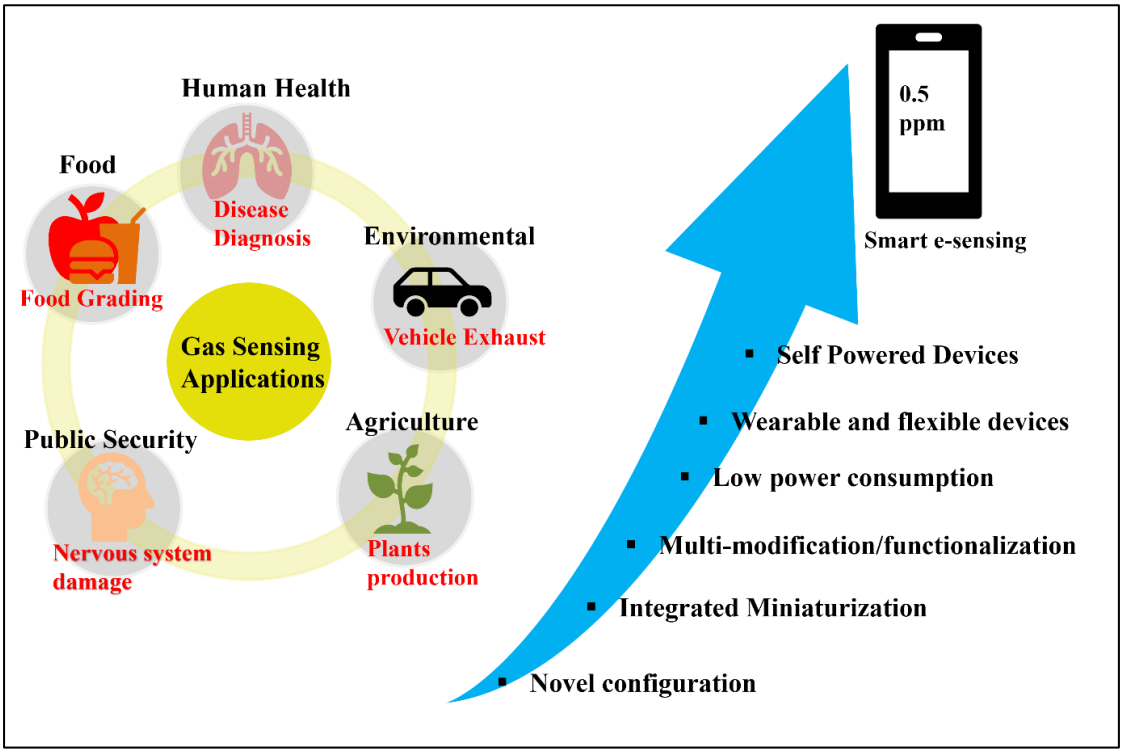

1.1 Overview

Air is the most important element for living beings to survive. The average human breathes around 10,000 liters of air every day [1]. Rapid industrialization and urbanization have increased the problem of air pollution [2]. Air pollution consists of many toxic chemicals, which directly or indirectly cause damage to not only the environment but at a low level to human health. For instance, every year approximately 3.8 million people deal with severe illness due to air pollution, which may prove to be fatal. Moreover, about 20 % of cardiovascular deaths and nearly 20 % of deaths due to stroke can be credited to household pollution [3]. Specifically, severe air pollution can cause abnormalities in lung surfactant composition and damage the lungs, making humans more prone to ailments such as COVID-19 [4]. Therefore, household or indoor air quality has naturally grabbed attention from both the general public and research communities. The most common causes of indoor air pollution are NO_x, NH_3, CO, CO_2, H_2, SO_2, CH_2O, volatile organic compounds (VOCs), and smog (PM2.5). These volatile

gases come from a variety of human activities, tainted ventilation systems, and inadequate air exchange in enclosed areas. World Health Organization (WHO) has claimed that household air pollution leads to about 3.8 million deaths per annum including 50 % of pneumonia deaths in children under five years of age.

As a result, gas sensors are now necessary for measuring and identifying a variety of gases in diverse settings [5]. A gas sensor is a chemical sensor-based equipment that produces a regulated, readable signal from chemical data. The two parts of a chemical sensor are referred to as the transducer and receptor. Chemical information is transformed into an energy form by the receptor, which is then detected and converted into an electrical form by the transducer. The way the receptor functions allows for multiple classifications of chemical sensors. Chemical, biological, and physical sensors are examples of this type of sensor. Whereas the target molecules in chemical sensors are the reaction between the target molecules and the receptor, the target molecules in biological sensors are biomolecules, such as DNA, proteins, and vitamins. Finally, in physical sensors, there is no chemical reaction at the receptor part. Temperature, mass, refractive index, and absorbance constitute the majority of the signal [6].

1.2 History of Gas Sensors

Lives have been badly affected by the toxic and harmful gases. To prevent accidents, early detection of harmful gases is now essential. The early detection methods in the sensors that were available up until this point were not as precise. The first detectors were elementary ways of detecting toxic gases. For example, the ancient Romans used canaries to detect toxic gases in mines. If the canary stopped chirping, meaning the presence of toxic gases and in case, the canary succumbed, the miner knew it was the time to leave the place. In the 17^{th} century, an Italian scientist used a device that could detect toxic gases using candles. If the candle went out, meaning the availability of hazardous gases. Further, in the 18^{th} century, a Swedish chemist laid the foundation for more sophisticated detection by identifying more toxic gases, including ammonia (NH_3), sulphur dioxide (SO_2), and chlorine gas. At the end of the 19^{th} century, the invention of electricity as an energy source paved the way for efficient new gas detection technologies. In 1903, the German physicist Walter Nernest developed the

Nernest gas detector, based on the electrical properties of metal oxides in the presence of the gas. This device was the forerunner of modern electrochemical gas detectors. Until then, there were few gas detectors, but they could not detect gases at precisely low concentrations. In 1926-1927, Dr Oliver Johnson's invention of catalytic combustion sensors marked the beginning of the contemporary era of gas detection. Depending on the user's experience, this sensor can estimate the quantities of flammable gases with an accuracy of 25–50%. The idea behind how it worked was that when gas interacts with something, the temperature changes. A reference cell and a detector cell constitute the sensor. The carrier is connected to a platinum (Pt) wire coil, which serves as the detection cell. An oxidization catalyst, like alumina, is applied to the detector cell. The gas burns when it comes into contact with the powered sensor. In essence, the reference cell is a Pt coil that has been treated to stop flammable gas from igniting when it comes into contact. A Wheatstone-Bridge circuit, with one part being active and the other serving as a reference, is used to measure the gas concentration. The catalyst-embedded Pt coil's temperature increases in response to combustible gas exposure because the active region's resistance increases. In contrast, the reference part's resistance doesn't change. As a result, a change in resistance overall will raise the device's temperature, and the Wheatstone-Bridge's output voltage is used to determine the target gas concentration. Following that, the field of gas sensors had a significant surge in interest when scientists discovered in 1962 that metal oxide semiconducting materials (MOS) might be used as a sensing layer to identify flammable gases. Zinc oxide (ZnO) semiconducting thin film was used by Seiyama et al. to construct a novel gas detector. The device's electrical conductivity changes at high temperatures (400 ˚C) due to the adsorption and desorption of gases [7]. In 1971, At Figaro Engineering Inc., Taguchi and his colleagues created gas sensors based on tin oxide. They also used noble metals to increase the sensor’s sensitivity. Subsequently, in order to gain a deeper understanding, other researchers began studying this field with additional metal oxide semiconductors and the suggested sensing mechanism. Later, the automotive industry encouraged the use of solid-state electrochemical sensors to lessen smoke and pollution, but these sensors weren't effective until higher temperatures, and thus couldn't detect pollutants during the crucial engine start-up and warm-up phase. The ion-selective field effect transistor (ISFET) was developed around the same period in the 1970s. It had an

insulating membrane and the same construction as a MOSFET but without a gate region. Target ions were sensed using this insulating membrane, and the signal from them was expressed in terms of current. The notion of electronic nose technology gained widespread acceptance as an efficient tool for detecting and quantifying olfaction after it emerged and went into commercialization in 1993 [8]. In addition to MOS, other materials have been investigated for use in the fabrication of gas sensors, including conducting polymers, solid electrolytes, two-dimensional (2D) nanostructured materials, and carbon nanomaterials. Every one of these materials has benefits and drawbacks. The search for novel gas sensing materials with high response and selectivity at room temperature has been sparked by the shortcomings of MOS-based gas sensors, which, while offering high sensitivity and low cost of detection of the target gas molecules, also come with large power consumption and high operating temperature. Conducting polymer-based gas sensors can function at ambient temperature, but humidity can quickly deteriorate them, resulting in a slow response and unstable recovery period [9]. Two-dimensional nanostructured materials are good candidates for electrically transducing gas sensors because of their special physical and chemical properties. Their thicknesses range from a few to tens of nanometers, and their lateral dimensions can reach several centimeters. Ever since graphene, an extraordinary two-dimensional material, was discovered, the variety of 2D nanomaterials that are available has been expanding per year. These include polymers, MXenes, hexagonal boron nitride (h-BN), graphite carbon nitride (g-C_3N_4), black phosphorous (BP), and transition metal dichalcogenides (TMDs, such as MoS_2, $MoSe_2$, and WS_2), as well as inorganic graphene analogs [10]. In an effort to increase the sensitivity of gas sensors around ambient temperature, a number of heterostructures, including 2D-1D, 2D-3D, and 2D-2D materials, have been investigated recently [11].

1.3 Different Types of Gas Sensors

Types of gas sensors have been classified on the basis of different detection methods and sensing principles [12]. The physical and chemical characteristics of the sensing material change when the target gas is present, which affects the sensing techniques used to detect gases. Certain sensing techniques rely on the response of the sensing material with the target gas to ascertain the gas concentration, while other techniques

compare physical attributes like wave propagation and velocity between the ideal mean and the gas being detected.

1.3.1 Optical-Based Gas Sensors

In order to detect the target gas, optical gas sensors rely on variations in optical characteristics such as absorbance, refractive index, fluorescence, and optical path length. Toxic gases can be detected using a variety of optical-based gas sensors, including as surface plasmon resonance, infrared spectroscopy, ultraviolet-visible spectroscopy, and others. The fact that optical gas sensors can function at ambient temperature is one of its benefits. A light-emitting element, a photo-detecting element, a gas-sensing element that reacts to light, and a filter that detects fluorescence or phosphorescence make up an optical gas sensor. Palladium (Pd) or chemochromic oxide thin films coated along an optical fiber's length are the basis for the majority of optical sensors. Butler (1984) revealed the first optical gas sensor, which is an optical fiber coated with titanium and palladium, can detect hydrogen gas [13]. A study by H. Manap et al. used an open optical path technique to construct an optical fiber sensor for the detection of ammonia gas. To determine how CO_2 and O_2 affected ammonia gas, cross-sensitivity tests were also conducted [14]. Optical gas sensors are easy to operate without oxygen with a wide monitoring range and are not affected by electromagnetic interference. Despite these, they get easily affected by ambient light interference causing the monitoring not to be reliable.

1.3.2 Quartz Crystal Microbalance (QCM) Based Gas Sensor

The Quartz Crystal Microbalance (QCM) sensor operates at room temperature with great sensitivity and precision because it is a piezoelectric device that is highly sensitive to changes in molecular mass [15]. A typical quartz crystal microbalance (QCM) can be made by utilizing gold electrodes to select the required precise orientation for ultrafine quartz discs. The physical and chemical makeup of the sensing material deposited on the active electrode of the QCM greatly influences the sensor's features. A shift in the direction of a certain frequency happens when an electrical input is applied to the quartz crystal [16]. At this specific frequency, there is also a shift in mass on the quartz crystal's surface. Because of its exceptional sensitivity to mass changes in the

nanoscale regime per unit area, the QCM acoustic wave sensor has become more well-known. A standard QCM has a center sensor and an AT-cut quartz resonator disc positioned between metal electrodes constructed like keyholes. The thin wafer known as AT-cut quartz is cut from a rod at a 35° angle with respect to the x-axis. The crystal provides stability at high frequencies and low temperatures [17]. QCM-based sensors offer optimized and prospective ways to enhance the sensor's sensitivity and selectivity to detect biological and molecular targets. They are employed in a variety of biological and chemical applications. Improving the crystal coating process, however, is one of the major obstacles to producing a consistent deposition layer that allows for reusability. Extreme frequency drift in liquid phase applications, which impacts oscillator circuit sensitivity, is another significant difficulty. To minimize this effect, more functional components like filters, inductors, amplifiers, etc. should be added to work efficiently in gas and liquid phases.

1.3.3 Electrochemical-Based Gas Sensor

The Clark Cell, which was developed in 1956 to measure oxygen levels, was the first example of an electrochemical gas sensor. The product and rate of the reaction are related to the gas concentration, and these sensors use chemical reactions to detect the target gas. The electrolyte, which is mostly made up of a liquid compound of acids or bases, the electrodes that are used up in the electrochemical process, and a membrane that isolates the electrolyte solution from surrounding gases make up the sensors. Depending on the sensing technique, which might be potentiometric (measures voltage), conductimetric (measures conductivity), or amperometric (measures current), the electrode polarization and output parameter measurement differ. Accuracy and sensitivity can be increased by limiting interaction with undesired gases by placing a filter between the membrane and ambient gases. The target gas and reaction temperature affect the materials employed in the sensors [18]. Electrochemical sensors operate straightforwardly and consume little electricity. Electrochemical gas sensors have a limited shelf life of six months to a year, depending on the target gas and environment. However, once calibrated to a known gas concentration, the sensor will read a repeated target gas with exceptional precision. Low humidity, high temperatures,

and cross-sensitivity to gas can dry out the electrolyte and deplete the gas sensors, which turns out to be the major concern for electrochemical sensors [19].

1.3.4 Field Effect Transistor (FET) Based Gas Sensor

The field effect transistor (FET) is a modern electric signal-based sensing platform that can quickly detect a variety of analytes, such as gases, ions, organics, and biomolecules. A FET is a low-power device that operates by controlling transfer performance with a small amount of gate potential. The source, drain, gate, semiconducting channel, and gate dielectric layer make up a FET device [20]. Based on their gate voltage-dependent FET behavior, a back gate and top gate comprise a conventional FET configuration. The physics of the dielectric, the doping level of the substrate semiconductor, the gate (top- or back-gate), source/drain electrodes, and the ohmic or Schottky contact between electrode and channel, and these are the inherent characteristics of FETs [21]. The basis of sensing applications is the measurement of FET electrical properties, which includes output characteristics (e.g., I-V measurements between source-drain current I_{ds} with a voltage sweep between contact channel and electrodes) and transfer characteristics (drain current Id measured under constant drain-source bias V_{ds} and gate potential sweep, which provides switching behavior that includes the on/off ratio and subthreshold swings) [22]. Analytes are found using the semiconducting sensing channel's variation in I_{ds} (conductance changes). The modifications that result from the deposited target gas molecules on the semiconductor surface provide the basis of the gas sensing principle.

1.3.5 Chemiresistor-Based Gas Sensors

One of the most common types of electric sensors is the chemiresistive gas sensor, which is widely employed because of its affordable price, ease of exact measurement, and predictable electrical characteristics [23]. By measuring the electrical resistance of the equipment, these sensors are utilized to determine the gas concentration of a target gas [24]. Three primary components constitute most chemiresistive gas sensors: an insulating substrate such as silicon dioxide, alumina, etc., sensing material, and interdigitated electrodes [25]. To achieve the ideal operating temperature, some of the gas sensors are either connected to a heater or coated with a micro hot plate. For better

compatibility of chemiresistors, several approaches are used, including solvothermal synthesis, hydrothermal, sol-gel, and self-assembly wet chemical processes to incorporate the sensing materials. The most researched method for chemiresistor gas sensors is the wet chemical method, which offers the benefits of mass production, a wide variety of morphologies with high surface area to volume ratios and porosity for easy and precise measurements, exceptionally low power requirements, and room temperature use [26][16].

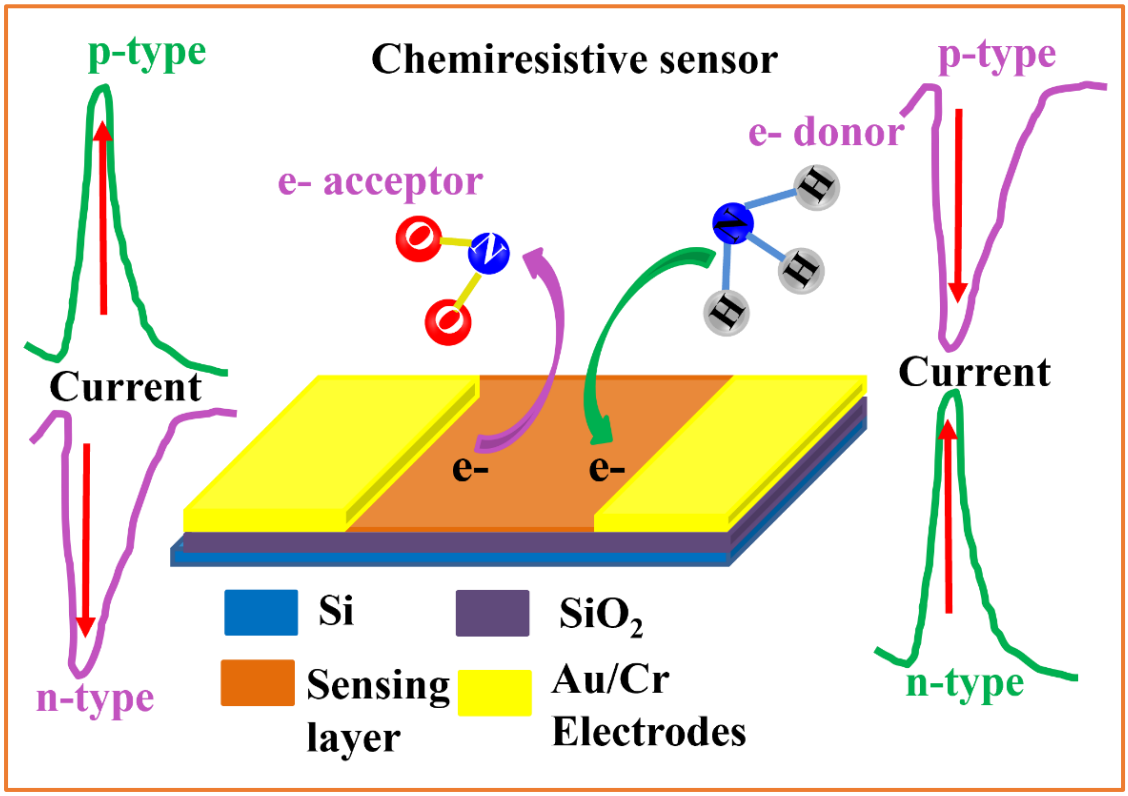

Fig. 1.1: Schematic illustration of a typical Chemiresistive gas sensor in the presence of NO_2 and NH_3 gases

1.4 Characteristics of a Gas Sensor

A Chemiresistive gas sensor's response, selectivity, sensitivity, operating temperature, response and recovery time, detection limit, and stability are the most often utilized features to assess its gas sensing performance. The features are discussed below as follows:

Sensor Response The resistance changes when the target gas is exposed, and this is represented by the sensor response. The ratio of the sensor's resistance in the presence of air (R_a) to that of the target gas (R_g) is its defined value. The target gas is decreasing in nature when this definition of response is applied. When an oxidizing gas is present, the response transforms into R_g/R_a.

$$\text{For oxidizing gas} \quad \text{Response } R_a/R_g \tag{1}$$

$$\text{For reducing gas} \quad \text{Response } R_g/R_a \tag{2}$$

In terms of relative response,

$$\text{For oxidizing gas} \quad \text{Relative Response (\%)} \left(\frac{Rg-Ra}{Ra}\right) \times 100 \tag{3}$$

$$\text{For reducing gas} \quad \text{Relative Response (\%)} \left(\frac{Ra-Rg}{Ra}\right) \times 100 \tag{4}$$

Selectivity A sensor can produce the maximum sensing response corresponding to a certain analyte, whereas the sensor should not recognize undesired gases simultaneously under similar conditions.

Sensitivity The lowest concentration of a target gas that a sensor can detect is known as sensitivity. It is expressed as a change in a sensor's measured signal per unit of gas concentration. A good sensor should have a high sensitivity, implying the response should be greater for each unit of gas concentration.

Operating Temperature is the required temperature at which the sensor produces the highest sensing response to the target gas.

Response Time is the required time to reach 90 % of the maximum response from the baseline**.**

Recovery Time is the time required to obtain 10 % of the base value of the response from the maximum response.

For an ideal sensor, the response and recovery times should be minimal at a particular gas concentration.

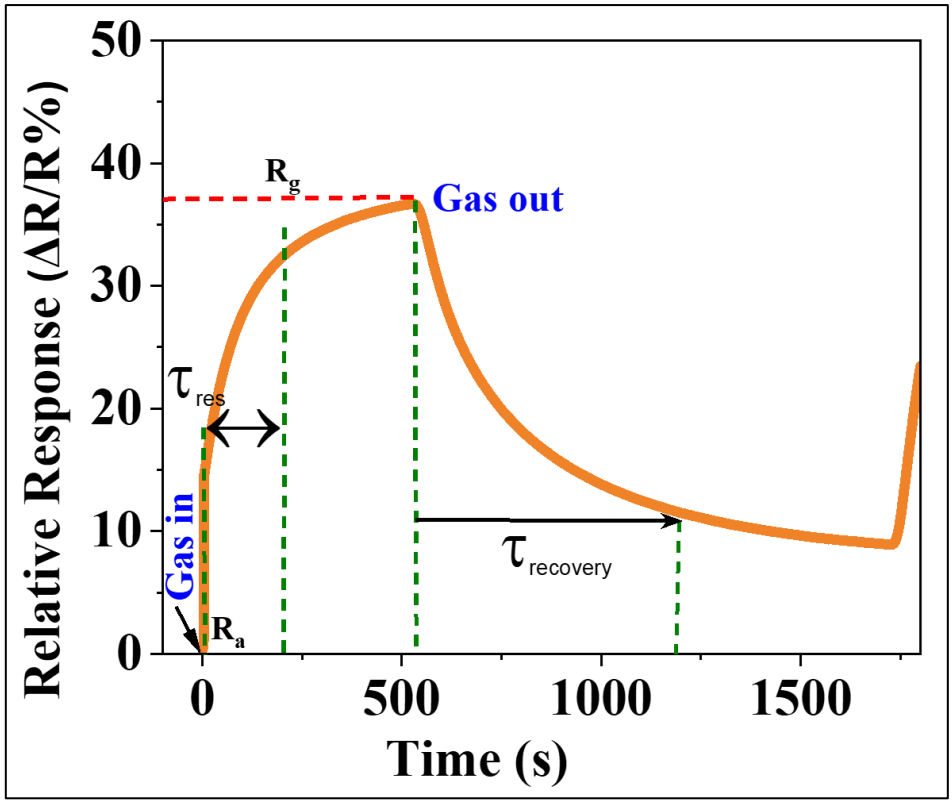

Fig. 1.2: Typical representation of response and recovery curves for chemiresistive gas sensor. Response (τ_{res}) and Recovery ($\tau_{recovery}$) times are marked on the plot

Limit of Detection (LOD) is the least concentration of the target gas that be reliably measured by the gas sensor under certain conditions.

Stability The ability of a sensor to produce the same sensing output under the same operating conditions for a longer time.

Reproducibility The sensor should produce the same sensing output under the same experimental conditions as the same sensor.

1.4.1 Factors Affecting Chemiresistive Gas Sensing

Three key parameters affect the gas sensing performance of chemisresistive gas sensors: transducer function, utility factor, and reception function.

The interaction between the detecting surface and the gas molecules is referred to as the receptor function. When exposed to gas, the increased surface area promotes surface disturbance and offers the most adsorption sites for gas molecules. Furthermore, the

response of a chemiresistive sensor is precisely proportional to the changes in resistance caused by gas adsorption. Moreover, defects are also introduced on the sensing surface to enhance adsorption for the surface modifications. Further, defects can be easily modified by simple functionalization and surface decoration methods[27].

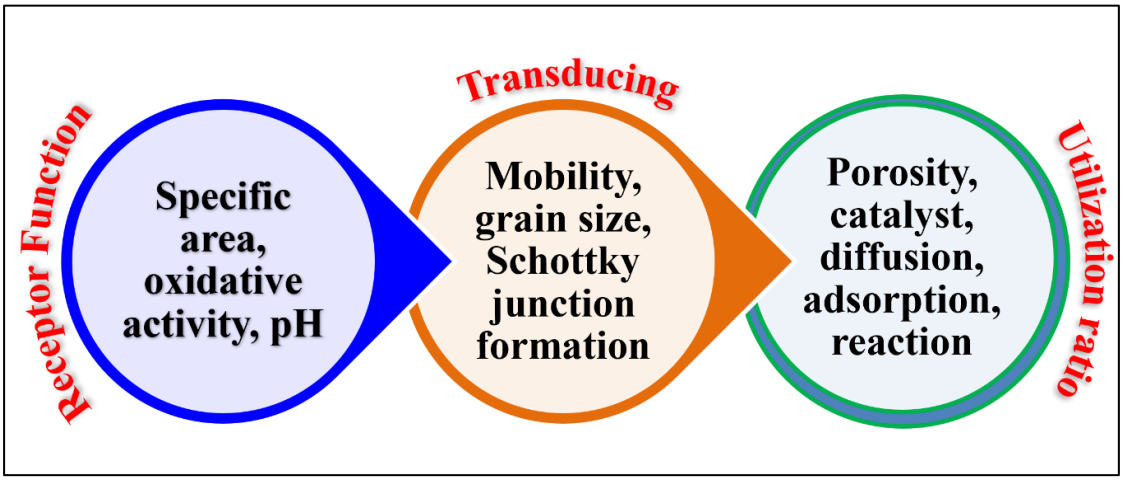

Fig. 1.3: Main factors of the gas sensors in sensing phenomenon for the sensing layer: Receptor function, transduction, and utilization ratio

The transducer function explains the capability of the sensor to transform the signal generated by gas adsorption into an electrical signal like resistance and current. The morphology of the sensing material can affect the transducer function. In chemiresistive gas sensors, gas adsorption affects the sensing material's charge concentrations and carrier density. The surface charge transfer mechanism can be altered by the schottky barrier height (SBH) created between the metal contact and the sensor surface [28]. Band bending at the space charge region for charge carrier separation and metal and semiconductor energy level alignment for charge carrier injection determine the band structure of the sensing surface, which leads to the modulation of the Schottky barrier, which is advantageous for gas sensing [29].

Utility factor is the capability of the inner sites of the sensing materials to access the target gas. For instance, if the sensing layer is too thick resulting in the diffusion path of gas molecules being too long and the pore size being too small at the time, then gas molecules cannot pass through the sensing layer. Reduction in the thickness or reducing the distance between the adsorbed gas molecule and the sensing surface can increase adsorption energy by improving the charge transfer.

1.5 Materials as Chemiresistive Gas Sensors

Chemiresistive gas sensors based on semiconducting materials have been considered the most suitable candidates for their applications in the Industrial Internet of Things (IIoT) era [30]. Metal oxides (MO_x) from the family of semiconducting materials, are the most explored materials to fabricate gas sensors [31]. Further, a variety of materials such as carbon nanomaterials [32], two-dimensional (2D) nanostructured materials[33], solid electrolytes[34], and conducting polymers [35] have been explored. Each of these materials has its advantages and disadvantages. MO_x offers highly sensitive, low-cost detection of target gas molecules, but their lack of selectivity and high-temperature operation causing larger power consumption have triggered the search for novel and efficient gas-sensing 2D nanostructured materials.

After the discovery of graphene (Gr), an exceptional 2D layered material, discovered by Geim and Novoselov in 2004, various 2D materials have gained exceptional research interest in many fields including gas and chemical sensing [36], due to their extraordinary 2D geometry, atomic level thickness, high surface activities, unique thickness-dependent chemical and physical properties[37]. Graphene-based gas sensors have been widely studied owing to their high carrier mobility, mechanical strengths greater than steel, and remarkable electronic and optical properties. Despite having impressive sensor response and response time, Graphene-based NO_2 gas sensors suffered from long recovery time due to the high adsorption energy of gas molecules with graphene [38]. Also, the synthesis and production of graphene is very costly with the use of toxic chemicals at high temperatures. The limitations of graphene turn the research direction to discover new non-zero bandgap 2D materials. Moreover, the carbon material-based sensors provide a high sensor response but the room temperature desorption rate of gas molecules is too slow causing low recovery time [39].

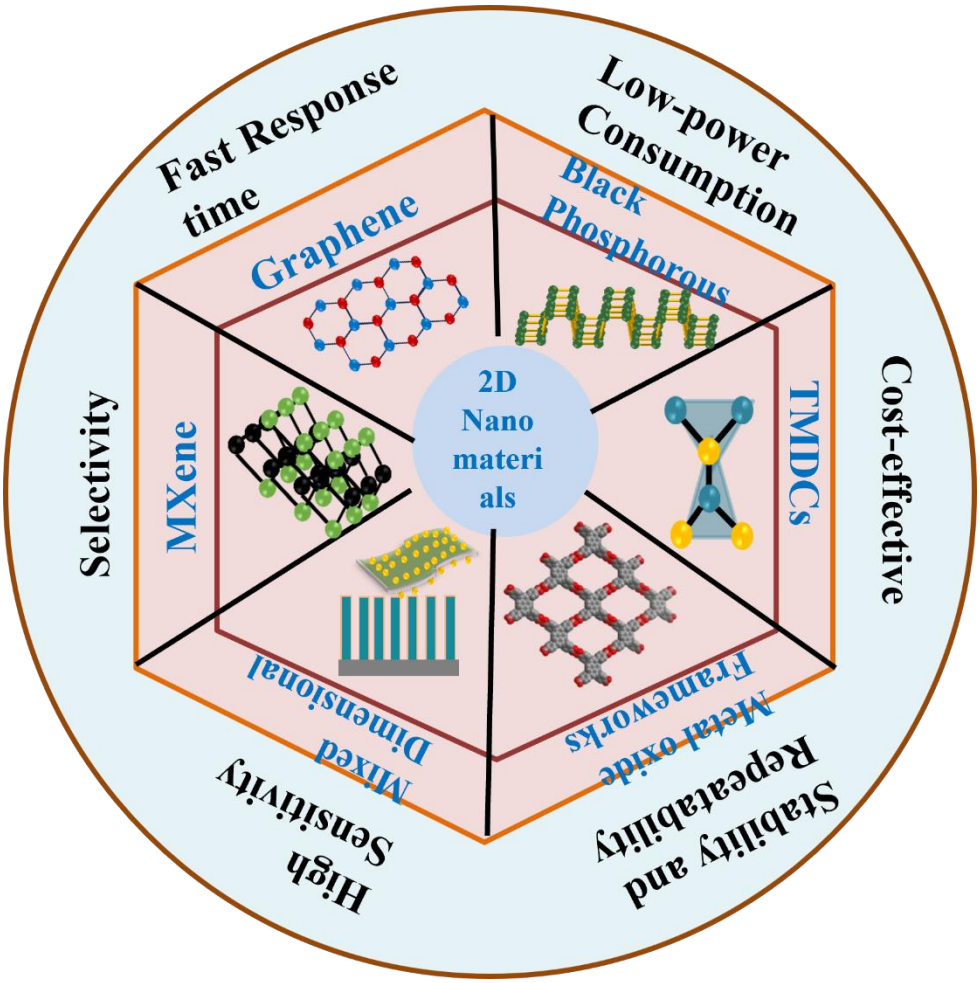

Fig. 1.4: An overview of various 2D nanomaterials utilized in gas sensing applications

The issues associated with metal oxides and carbon-based sensors have demanded the development of new materials with advanced gas-sensing properties. However, an ideal gas sensor should have a higher sensor response and lower response/recovery times near room temperature. Therefore, there is a huge demand to develop low-temperature, highly sensitive, and fast-responding sensors.

1.5.1 2D TMDCs

Transition metal dichalcogenides (TMDCs) are MX_2-type inorganic compounds where M is a transition metal such as Mo, W, Nb, Zr, Ti, V, or Re in groups IV, V, and VI of the periodic table and X is an element of chalcogen family such as S, Se, or Te. Single or few layered TMDCs have shown extraordinary electronic properties in comparison

to graphene [40]. The 2D layered structure of TMDCs consists of strong molecular intralayer bonding and weak Van der Waals interlayer interaction. This weak interlayer interaction allows the exfoliation of TMDCs down to single- or multi-layers using mechanical exfoliation or electrochemical intercalation [41]. Usually, the thickness of layered TMDCs is about 6-7 Å and the bond length of M-M typically varies between 3.15 to 4.03 Å, depending on the size of metal and chalcogen atoms [42]. Higher specific surface area and functionalities driven by such structure make 2D TMDCs promising candidates for sensor applications.

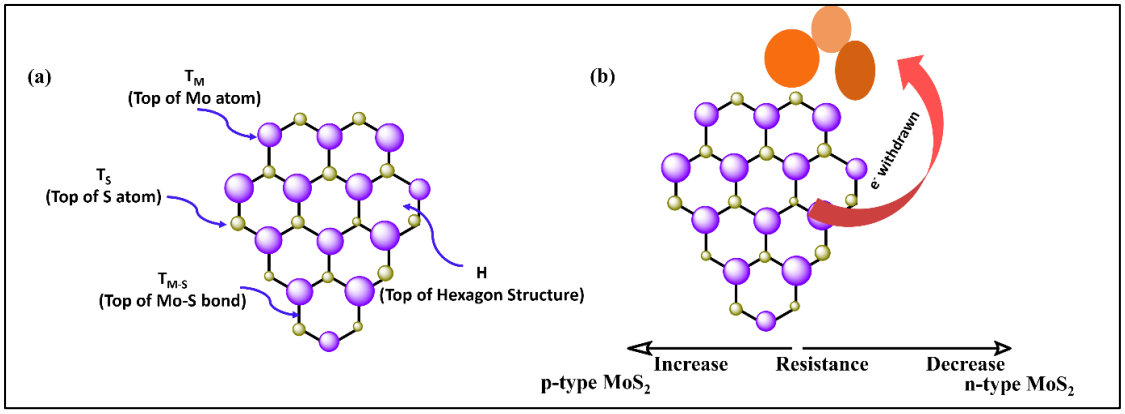

Fig. 1.5: Schematic representation of (a) possible interaction sites on the MoS_2 surface, and (b) effects of NO_2 gas interaction on the MoS_2 surface

In TMDCs, MoS_2 is at the forefront of the race for an ideal gas-sensing material. Most of the research with MoS_2 in the gas sensing field has been carried out on NO_2 detection. In MoS_2, the arrangement of atoms of each layer, Mo atoms are sandwiched between covalently bonded S atoms, with layer height of about 0.65 nm. MoS_2 has two crystal phases, trigonal (1T) and hexagonal (2H), where 1T is metallic while 2H is semiconducting. During the exfoliation or intercalation, the indirect bandgap of bulk MoS_2 is converted into a direct bandgap of monolayers from 1.2 eV to 1.8 eV [43]. The absence of dangling bonds provides stability to pristine MoS_2 in liquid and gaseous media in the presence of oxygen. The high on/off ratio (10^8), the high carrier mobility of 400 $cm^2V^{-1}s^{-1}$ at room temperature, and the low electron effective mass (0.48 m_e) are advantageous for developing fast gas sensors [44]. MoS_2 nanosheets have four Raman active modes (E_{1g}, E^1_{2g}, A_{1g}, E^2_{2g}). Chakraborty et al. studied that for monolayer MoS_2,

E^1_{2g} is not sensitive to electron doping but the A_{1g} mode is very sensitive to electron doping. The A_{1g} mode gets softened with high electron concentration due to the stronger electron-phonon coupling mode than the E^1_{2g} mode [45]. These vibrational characteristics are ideal for chemiresistive gas sensors where charge concentration is an important parameter. Excellent gas molecule detection capability, abundant active sites, large surface-to-volume ratio, and availability of favorable adsorption sites have validated MoS_2 as the unique sensing material.

The 2D TMDCs have been inclined towards room temperature sensing but they show poor recovery. So, to achieve high performance, thermal assistance or UV illumination is provided, which causes an issue of higher power consumption [41]. For full gas desorption i.e. complete recovery, MoS_2 is heated to 100 ˚C but the sensitivity is lowered. So, to overcome this difficulty with improved sensitivity around room temperature, MoS_2 surfaces were functionalized with dopants and metal oxides. Gas diffusion and adsorption in 2D TMDCs were greatly facilitated owing to the low dimensional morphologies and catalytic effect of the additive components respectively.

1.6 Sensing Mechanism of Chemiresistive Gas Sensors

In the context of chemiresistive gas sensors, the two primary aspects to take into account are usually the identification of the target gas molecules and the subsequent transformation of their signal into a measurable reaction. The adsorption and desorption of the gas molecules onto the gas sensor's active surface is the main focus of the sensing process. Charge transmission occurs within the molecules of the target gas and on the gas sensor's surface, depending on the detecting material and the nature of the gas—that is, whether it is oxidizing or reducing. Consequently, the sensor's resistance varies in response to variations in gas concentrations at a specific working temperature, enabling the detection of gas molecules using this method. However, as soon as the gas molecules desorb from the active layer, the sensor returns to its initial state [46].

1.6.1 Sensing Mechanism of Metal Oxides (MO_x)-based Gas Sensors

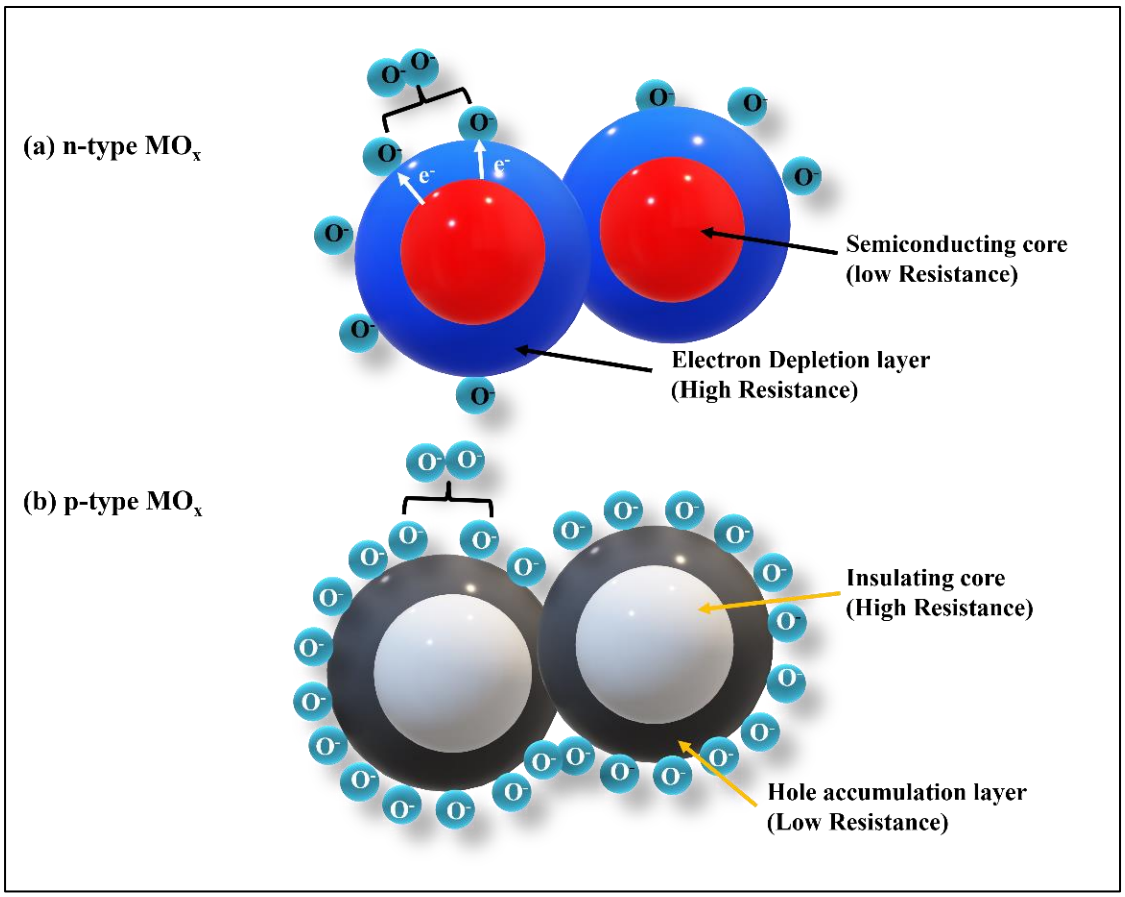

Fig. 1.6: Schematic illustration of the development of core-shell structure and basic gas sensing reaction in n-type and p-type MO_x

Compared to other TMDC materials, MO_x-based sensors function differently. The deposited oxygen ions on the oxide surface play a major role in the metal oxide-based sensors' detecting mechanism. By removing electrons from the metal oxide's conduction band, oxygen ions can be formed. Depending on the operating temperature, different types of oxygen ions are produced. The oxygen molecules have electrons bonded to them below 200 ˚C. By removing electrons from metal oxides, oxygen molecules disintegrate above 250 ˚C producing oxygen ions that carry an electric charge. This phenomenon is explained in the equations shown below.

$$O_2\ (gas) + e^- \leftrightarrow O_2^-\ (adsorbed) \quad [< 200\ ^\circ C] \qquad \text{Eq. (1)}$$

$$\tfrac{1}{2}\ O_2 + e^- \leftrightarrow O^-\ (adsorbed) \quad [> 250\ ^\circ C] \qquad \text{Eq. (2)}$$

$$\tfrac{1}{2}\ O^2 + 2e^- \leftrightarrow O^{2-}\ (adsorbed) \quad [> 250\ ^\circ C] \qquad \text{Eq. (3)}$$

Depending on if the majority carriers as electron or hole are involved, the interaction between the oxygen ions and the molecules of the target gas can be categorized into two basic groups. A metal oxide can be described as a p-type semiconductor when the bulk of its charge carriers are holes, and as an n-type semiconductor when the bulk of its charge carriers are electrons. In the case of n-type metal oxides, the reactions (1-3) that are described cause the metal oxide's conduction band to lose electrons. This is because the adsorbed oxygen molecule takes electrons from the metal oxide's detecting surface and transforms them into oxygen ions, which increases resistance. The potential barrier at the interface of the grains and electron depletion layer on the metal oxide surface is created by an upward band bending caused by the change in electronic states. In the case of p-type metal oxides, a downward band bending and hole accumulation layer form on the surface of MO_x, producing an opposite effect that reduces the sensor's resistance [47]. When n-type MO_x is exposed to a target gas, such as an oxidizing gas (NO_x), the oxidizing gas will take electrons out of the metal oxide's conduction band and increase the sensor's depletion layer and resistance. In contrast, when reducing gas (NH_3) is used, the electrons are transferred to the metal oxide's conduction band, and the sensor's depletion layer and resistance decrease. In contrast, in p-type MO_x, the width of the hole accumulation layer reduces with exposure to the target gas molecules if the gas is oxidizing in nature. This leads to a decrease in resistance, and the opposite effect is evident upon exposure to reducing gas. Because there are unpaired electrons available around the N atom, NO_x functions as an oxidizing gas, whereas NH_3 is regarded as a reducing gas because it has a single pair of electrons. Because oxygen ions play such a major role in metal oxide sensors, they are often operated at higher temperatures [48].

1.6.2 Sensing Mechanism of 2D Materials-Based Gas Sensors

The sensing mechanism of 2D materials (graphene, TMDCs, and MXene, etc.) is popularly based on the adsorption of gas molecules and charge transfer process, but the participation of adsorbed oxygen species (O_2^-, O^-, O^{2-}) is not necessary, yet the role of oxygen functional groups should not be neglected. The adsorption of the target gases on the surface of 2D material causes resistance and charge carrier concentration modifications [49]. The 2D materials with the interaction of the gas molecules can either behave like p-type with a decrease in resistance or n-type with an increase in

resistance for target gas molecules. The physisorption or chemisorption of gas molecules on the sensing materials leads to the development of the charge transfer mechanism. The gas molecules and the sensing material interact through the physiorption process when using pristine 2D material, such as TMDCs, as a sensing layer. With their pristine TMDCs material, the gas molecules have a long adsorption distance, high binding energy, and weak adsorption energy. This leads to minimal charge transfer and a nearly unchanged electronic structure, which causes the gas sensor to recover quickly and has a low sensing response. Defects are created during the production of 2D material in the chemisorption process. With low binding energy and a small adsorption distance between the gas molecules and the adsorption sites during the gas contact, there is a large shift in the electronic states, high charge transfer, and a longer recovery time [50]. Charge transfer takes place from 2D materials to the target gas molecules when the fermi level of the 2D materials is greater than the lowest unoccupied molecular orbital (LUMO) state of the target gas molecules. This process further lowers the fermi level of the 2D materials. Conversely, charge transfer from target gas molecules to 2D materials occurs when the fermi level of 2D materials is less than the highest occupied molecular orbital (HOMO) state, which elevates the fermi level of 2D materials [51].

1.6.3 Sensing Mechanism of 2D Materials/MO_x Composite Based Sensors

It has been observed that a pristine form of either metal oxide or 2D materials is not sufficient for high sensing response, thus the development of 2D/MO_x composite-based gas sensors is implemented. The combined effect of both metal oxides and 2D materials is possible due to their different geometry, electronic states, and chemical states.

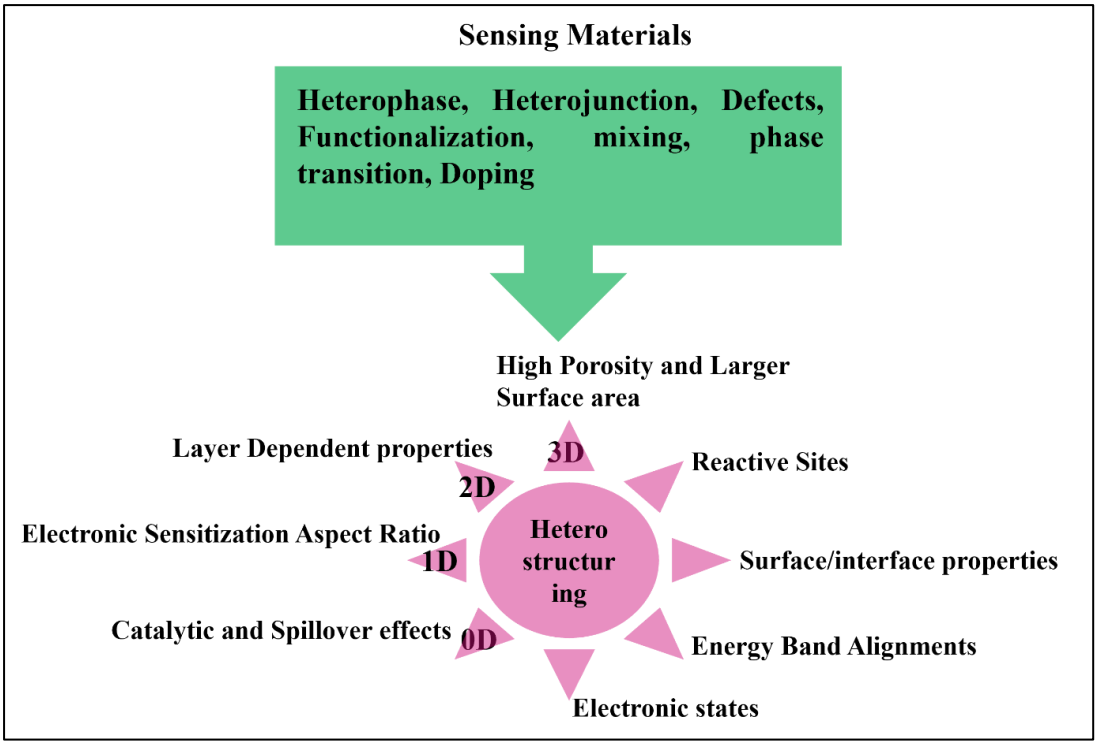

Fig. 1.7: Different types of nanostructuring employed in gas sensing and their contributions

1.6.3.1 Geometrical Effects

As Metal oxides with controlled growth and porous nanostructures are incorporated into 2D nanomaterials, gas adsorption and desorption become easy, increasing in sensor response and this is possible due to the high number of active sites available on the surface of 2D materials. Similarly, when 2D nanomaterials are incorporated into MO_x sites, the separation of 2D nanosheets takes place, increasing surface area and also modifying the electrical resistance of the nanocomposite during target exposure and facilitating the gas diffusion leading to improved response and recovery.

1.6.3.2 Electronic Effects

It is possible to achieve the heterostructure generation in a p-p/n-n or p-n/n-p type architecture. Band bending, which is caused by charge transfer at the interface between MO_x and 2D material during the adsorption/desorption of target gas molecules, can be used to understand the gas sensing mechanism. A built-in potential (V_{bi}) is created at the interface as a result of the charge transfer that brings the fermi energy of the 2D material and MO_x to the same level. This causes an electron depletion or hole

accumulation layer to form. V_{bi}'s primary function is to impede additional charge carrier transit across the heterojunction, raise the sensor's resistance until charges are transferred from the target gas molecule to the sensor, and enhance the sensor's selectivity and reaction time.

1.6.3.4 Chemical Effects

By reducing the activation energy and speeding up the response and recovery time, the creation of a nanocomposite modifies the chemical bonding between the metal oxide and 2D materials, causing the formation of a charge transfer bridge during the adsorption or desorption of the target gas molecules. The presence of oxygen functional groups on the surface of 2D materials results in more adsorption active sites and a greater sensor response. The superior analyte characteristics of MO_x also contribute to an improvement in selective adsorption.

1.7 Challenges and Strategies in the Application of 2D Materials

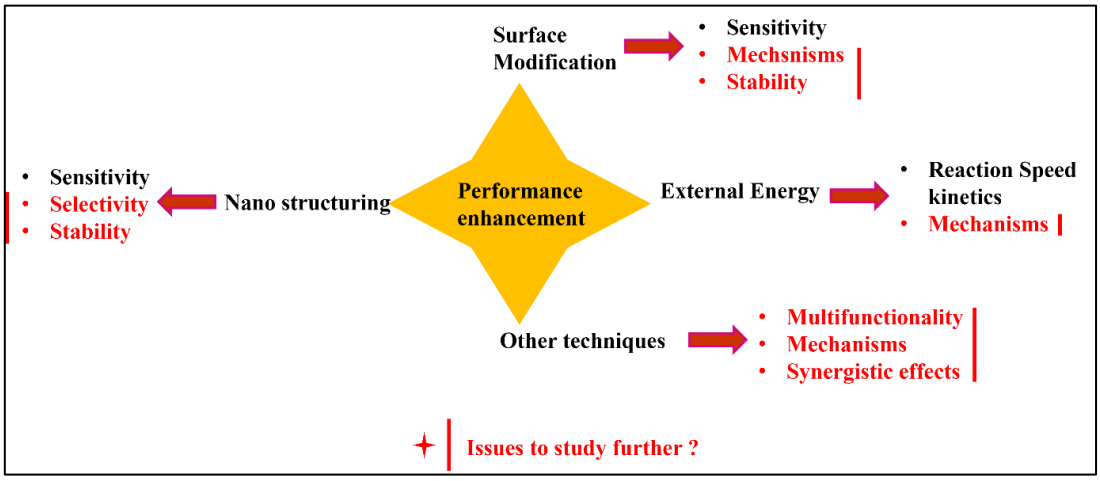

Fig. 1.8: Strategies to enhance sensor performance using various techniques

Despite significant advances in the development of gas sensors with good selectivity and sensitivity, there is still a significant gap in the research. The special surface geometries of 2D materials make them suitable with controllable gas sensing attributes and to enhance the gas sensing efficiency, the integration of them with other nanostructured materials. Other aspects such as atomic layers, composition, quality, and existence of functional groups are responsible for influencing their sensing behavior. Apart from the discussed

materials, other 2D materials such as MXenes, metal-organic frameworks (MOFs), g-C_3N_4, and other similar materials are now in the budding phase and several research have been performed to investigate their gas-sensing properties. Further, it is important to acquire a thorough understanding of the geometrical, electronic, and chemical effects of hybridization. The Fermi energy and work functions of each material, as well as the other characteristics of the sensing materials, are crucially considered while developing a heterostructure. The dominant sensing mechanism as well as the direction of charge carrier transport at the interface plays a vital role in the sensing mechanism. Additionally, proper attention is needed to be paid to selecting the metal electrode, which is responsible for collecting generated charges. The selection of high-performance metal contacts is the additional benefit of utilizing the full performance of the 2D materials-based sensor. Furthermore, enhancement in selectivity and stability is of vital importance. Cross-response to the gases is one of the attributes exhibited by the gas sensors that possess similar chemical and physical characteristics. To confront this issue, it is important to apply strategies like the integration of sensors with tailored catalysts, surface modifications, and the advancement of efficient processing methodologies such as spin/drop coating or vapor phase growth. Further, to minimize the fluctuations in baseline resistance due to variable humidity at low-temperature operation, surface engineering, creating novel gas sensing materials that are naturally tolerant to humidity or hydrophobic materials are introduced.

1.8 Thesis Problem

The current thesis aims to improve the sensing capabilities of MoS_2-based gas sensors and explores the impact of various heterostructures on the gas sensors' overall performance. The study looks at several synthesis techniques, especially in terms of cost effectiveness and environment friendly, for creating heterostructures that serve as the gas sensing device's sensing layer. It also looks at how well various manufactured gas sensors function in terms of gas sensing for various gases, such as NO_2 and NH_3. Additionally, a large section of the thesis emphasises the benefits of creating heterojunctions to improve sensing performance at room temperature and ambient settings, hence extending the application of 2D materials in gas sensing. The novelty of the present work mainly involves the fabrication of the gas sensing devices using the materials which are environmentally stable and present in abundance in the nature.

1.8.1 Objectives of Present Work

This thesis is largely concerned with the synthesis of nanocomposites based on two-dimensional materials and the subsequent exploration of their sensing applications, particularly gas sensing. The following are the key objectives of the thesis:

1. To study the gas sensing response of fabricated gas sensors based on transition metal dichalcogenides as a function of chalcogen atoms (S, Se, Te).
2. To study the effect of different transition metals (Mo, W) in transition metals for gas sensing.
3. To synthesize the different heterostructures with 2D materials such as 2D /2D heterostructures, and 2D/1D heterostructures and study the difference in their gas sensing performances in ambient conditions.
4. To investigate the gas sensing performance of fabricated different TMDCs (MoS_2, $MoSe_2$, WS_2) gas sensors for various gases (NO_2, NH_3, CO, etc.)
5. To study the influence of various light illuminations on the gas-sensing device's sensing behavior.

1.8.2 Thesis Overview

In this thesis, a comprehensive set of experiments and in-depth analyses have been conducted following the aforementioned goals. The findings of the current thesis are explained in the subsequent chapters:

Chapter 1: Introduction

A brief overview of the need for and several approaches to developing sustainable gas sensors that operate at room temperature to identify dangerous contaminants in the environment is provided in Chapter 1. The importance of gas sensors and suggestions for improving their effectiveness and performance are covered in this chapter. Over the last several years, a wide range of applications such as wireless sensor networks, smart homes, health monitoring, artificial intelligence, human-machine interface, and the Internet of Things have seen an increase in the popularity of portable electronic devices. The creation of quick and dependable gas sensors is facing significant challenges due

to the growing demands for technology and growth. Conventional gas sensors in wearable and wireless devices are prone to several limitations due to their elevated working temperatures. It is strongly desired that wearable technologies respond quickly and practically to room temperature gas sensors in order to address this problem. Many materials, including electrochemical, photonic, and chemiresistive gas sensors, have been developed over time based on various methods to provide good gas sensors. Although there are other available sensors based on different mechanisms that also exhibit phenomenon response, such as optical and infrared gas sensors, chemiresistive gas sensors have attracted a lot of attention because of their affordability, simplicity of use, versatility, miniaturization, and selectivity—especially when used in arrays that function as electronic noses. Chapter 1 contains a comprehensive literature overview of the various materials and gas sensors that have developed over time in this subject.

Chapter 2: Synthesis and Characterization Techniques

The synthesis and analysis of the produced samples have been done using a variety of experimental techniques, which are described in Chapter 2. Due to their distinct mechanical, optical, and electrical characteristics as well as their non-toxic nature, 2D transition metal dichalcogenides (TMDCs) have drawn the attention of researchers. The usage of TMDCs in the production of gas sensors has increased due to their low weight, environmental stability, affordability, and ease of processing. The hydrothermal method for the synthesis of MoS_2 has been covered in this chapter initially, after the discussion of the hydrothermal method and thermal annealing with chemical vapor deposition for the synthesis of nanocomposites. A brief discussion has also been held regarding the process of drop casting in the creation of nanocomposite films. The produced materials were examined using characterization techniques such as powder X-ray diffraction, SEM, Raman, UV-Vis Spectroscopy, and XPS, among others, which are reported in detail.

Chapter 3: Effect of varying the precursors' concentration on structural and electronic properties of 1T/2H phase MoS_2 for gas sensing application

In this chapter, we have attempted to synthesize a mixed phase of 1T/2H-MoS_2 using the simple hydrothermal method with the ammonium ions (NH^{4+}) intercalation. MoS_2

consists of two majorly discussed phases: 2H-MoS_2 and 1T-MoS_2. 2H-MoS_2 is environmentally stable and semiconducting whereas 1T-MoS_2 is metallic and not stable in the environment. In the previous research, to synthesize the 1T phase, usually Li^+ ion intercalation has been used. In this work, we have prepared a mixed phase 1T/2H-MoS_2 at 200 ˚C using the hydrothermal method. During the synthesis, keeping the 1:2 molar ratio, the concentrations of the precursors have been changed in the order of 1 M, 1.4M, and 1.8M, and the samples have also been labeled as MoS_2-1, MoS_2-1.4, MoS_2-1.8. it has been observed that as the concentration of NH^{4+} ions in the mixture increases, the 1T phase increases, which has been confirmed by the Raman Spectra. With the increase in NH^{4+} ion concentration from 1-1.8M, the morphology changes widely, the nanoflowers turn into smaller sticks and seem to be aggregated in the form of bundles for MoS_2-1.8. From UV-Vis Spectroscopy, it has been observed that MoS_2-1 with more 2H-nature shows the least absorption in the region of 400-700 nm whereas MoS_2-1.4 and MoS_2-1.8 show a sudden rise in the absorption indicating the presence of more metallic character. The indirect bandgaps have also been calculated using tauc plots. A fall in the bandgap value has been observed as the 1T character improves. The percentage character of 1T present in the mixed phase has also been calculated using the deconvolution peak of Mo 3d obtained from the XPS curve fittings. As the precursor concentration increased from 1-1.8M, the 1T character in MoS_2 evolved to 27.9% (1 M), 36.3% (1.4 M), and 45.8% (1.8 M), while the 2H character appeared to diminish. Additionally, as concentrations increased, so did the peak's area percentage and intensity associated with Mo6+ accessible at 236.2 eV, suggesting incomplete sulfurization of the Mo precursor. The sharply edged microflower form and reduction in band gap suggest that NH^{4+} ions intercalated 1T/2H MoS_2 may have advantages for gas sensing applications.

Chapter 4: Investigation of the NO_2 gas sensing response of MoS_2-based gas sensors with SnO_2/MoS_2 and CB/SnO_2/MoS_2 heterostructures in ambient conditions

Although we looked at the advantages of the characteristics of MoS_2 for gas sensing in Chapter 3, the performance of the device's output could also be impacted by the way MoS_2 forms nanocomposites with other metal oxides or materials. We created various gas sensors based on SnO_2-MoS_2 to observe changes in sensing performance. Additionally, active

carbon black (CB) was added to observe device performance further. Three devices were created and their gas sensing capabilities for NO_2 gas at room temperature were tested. These devices were labeled as bare MoS_2, SnO_2/MoS_2, and $CB/SnO_2/MoS_2$. When SnO_2 nanoparticles were added to the MoS_2 surface, it was discovered that the material's ability to sense gas improved. Additionally, the addition of CB improved the gas sensing performance of $CB/SnO_2/MoS_2$, which may have been brought about by the CB's increased electrical conductivity. When exposed to NO_2 gas, the bare MoS_2 exhibited p-type behavior and demonstrated a gas sensing response of about 42% with a response time of 61 s at a concentration of 50 ppm NO_2. Gas sensors based on SnO_2/MoS_2 demonstrated an enhanced response of approximately 46% with a significantly shorter response time of 26 s and recovery time of 73 s at 50 ppm of NO_2 gas concentration at room temperature, in contrast to the bare MoS_2 gas sensor, which showed a sensor response of approximately 43% with a response time of 52 s. When exposed to NO_2 gas, the charge transfer process between the components powers the ternary composite's gas-sensing mechanism. Since SnO_2 exhibits n-type conductivity and MoS_2 is a p-type material, most of the high-energy spots on the surface of MoS_2 are occupied by SnO_2 nucleation during the composite production process. When electrophilic NO_2 is exposed to heterostructures, the electric resistance decreases, indicating that both $CB/SnO_2/MoS_2$ and SnO_2/MoS_2 exhibit p-type semiconducting behaviors. The resistance curves show that MoS_2 has a lower starting resistance than SnO_2, indicating that holes have moved from p-type MoS_2 to n-type SnO_2. Additionally, because their work functions differ, the direction of electron flow in MoS_2 is opposite. When SnO_2/MoS_2 forms, an equilibrium state is reached at the heterojunction. Electron-hole recombination and band-level bending result in the broadening of the depletion layer, which prevents carrier transfer at the p-n heterogeneous region and creates a potential barrier. Band bending results from the electrons from SnO_2 NPs being captured by NO_2 gas molecules, which lowers their electron concentration and causes the adsorption mostly induced by the defects to be restricted. Additionally, the electrical effect created by the p-n-junction becomes dominant. A greater number of holes form at the MoS_2 surface during adsorption, which dramatically lowers the resistance of SnO_2/MoS_2 heterostructures and depletes the potential barrier. The sensitivity of the $CB/SnO_2/MoS_2$ sensor to NO_2 is significantly higher than that of SnO_2/MoS_2 and MoS_2. This is not only because of the formation of a p-n junction between MoS_2 and SnO_2, but also because of CB, which gives

the sensing material with a bandgap of 1.96 eV p-type semiconducting behaviour and higher electrical conductivity. The Schottky barrier between CB and SnO_2 is also a major contributing factor. A potential barrier is created at the interface when NO_2 molecules come into contact with the CB/SnO_2/MoS_2 surface because the work function of SnO_2 (4.85 eV) is higher than that of CB (4.5 eV). As a result, the holes will accumulate on the SnO_2 side until the Fermi level reaches equilibrium, at which point the resistance will dramatically decrease. The sensor response to NO_2 gas is accelerated by the p-n heterojunctions between CB-SnO_2 and MoS_2-SnO_2, as well as the Schottky barrier between CB and SnO_2/MoS_2, according to the sensing processes for NO_2 gas that have been studied.

Chapter 5: Investigation of the gas sensing performance of MoS_2/MoO_3-based gas sensors for NO_2 and NH_3 gases simultaneously at ambient conditions

In this chapter, the hydrothermal approach was used to synthesise MoS_2/MoO_3 nanocomposites, which were then thermally annealed in the presence of Ar gas to further improve the efficiency of the gas sensors after the performance of the MoS_2 gas sensors with SnO_2 was analysed. Initially, MoS_2 was made by the hydrothermal approach, which involved changing the reducing agent while keeping the same primary precursors. The synthesised materials were compared to the sample made without the use of any reducing agents. Hydrazine Hydrate (HH) and L-ascorbic acid (LA) were the reducing agents utilised. This synthesis method has a significant impact on the generated materials' morphological and structural characteristics as well. One technique for creating mixed-morphology nanocomposites is controlled thermal annealing, which has applications in environmental engineering, biomedical, defence & security, healthcare, and energy production. Consequently, the MoS_2:MoO_3 based gas sensor, which was manufactured without the use of any reducing agent, shows a good sensor response and a repeatable, full recovery sensing performance. An increased number of oxygen adsorption sites and active edges on the surface are critical for improved gas sensing capability. The dual gas sensing capabilities of the synthesized materials (MoS_2:MoO_3, HH-MoS_2:MoO_3, and LA-MoS_2:MoO_3) for NH_3 and NO_2 gas have been examined in this chapter. We have demonstrated that adding MoO_3 nanoparticles can significantly enhance the MoS_2-based gas sensors' ability to detect NH_3 gas. When NH_3, NO_2, CO, H_2S, and other gases were present, the performance of MoS_2:MoO_3-based

gas sensors was first compared to that of HH- & LA-MoS_2:MoO_3-based gas sensors. It was found that MoS_2:MoO_3 is exhibiting good recovery for NH_3 and NO_2 gas around room temperature with a better sensor response. Subsequently, the synthesized materials were subjected to NH_3 and NO_2 gas at concentrations of 1–10 ppm at room temperature to conduct detailed research. Sensing responses were then recorded. The reactivity to NH3 gas was stronger for HH-MoS_2:MoO_3, notwithstanding their incomplete recovery. The sensing response observed for NH_3 gas was in the following order: MoS_2:MoO_3 > LA-MoS_2:MoO_3 > HH-MoS_2:MoO_3. Conversely, only MoS_2:MoO_3 among these three composites offered full recovery for the NH_3 gas. The contact of gas molecules on the gas-sensing material's upper surface has already been shown to activate the gas response of the sensor. According to the XPS spectra, HH-MoS_2:MoO_3 has more adsorption sites and oxygen vacancies, suggesting that rapid adsorption leads to a greater sensing response while insufficient desorption from the oxygen sites results in partial recovery. When it came to NO_2 gas detection, LA-MoS_2:MoO_3 responded more strongly to the gas. In addition to having superior relative responses, the LA- and HH-MoS_2:MoO_3-based sensors had the same problem with partial recovery since there was less NO_2 molecule desorption. The resistance dropped when exposed to NH_3 gas, demonstrating n-type behavior. The conductivity behavior should ideally be the same when the same material comes into contact with gas. However, in our instance, the resistance dropped when the produced materials were exposed to NO_2 gas, demonstrating the p-type behavior. The primary variation in conductivity can be attributed to the distinct adsorption sites functioning as conductive pathways for various gases. Since NH_3 is a reducing gas and exhibits an n-type sensing response, MoO_3 appears to be the main source of NH_3's adsorption sites. The p-type sensing behavior in the case of NO_2 gas suggests that sulfur vacancies present on the surface of p-type MoS_2 may serve as the primary conductive routes for NO_2 gas sensing. This peculiar behavior can be due to the different NH_3 and NO_2 adsorption sites on the sensing material's surface. Resistance variation demonstrated that MoO_3, not MoS_2, dominated the NH_3 gas-sensing mechanism in composites. Surface alteration and hetero-interface-induced superposition effect were linked to improved NH_3-sensing performance. Even though the sensor response to MoS_2:MoO_3 was enhanced, the higher concentration of O_v and $O^{2-}_{(ads.\ sites)}$ in HH-MoS_2:MoO_3 and LA-MoS_2:MoO_3

negatively led to accumulation on the MoO_3 surface, which made it harder to desorb from. This resulted in incomplete recovery and unsatisfied sensitivity.

Chapter 6: Conclusions and Future Prospectives

A brief overview of all the research findings is given in this chapter, along with a comparison with existing literature on various gas sensors. The challenges and future scope of this study action are also covered in this chapter.

References

[1] C. M. Huang *et al.*, "A multi-gas sensing system for air quality monitoring," *Proc. 4th IEEE Int. Conf. Appl. Syst. Innov. 2018, ICASI 2018*, pp. 834–837, 2018, doi: 10.1109/ICASI.2018.8394393.

[2] S. M. Majhi, A. Mirzaei, H. W. Kim, S. S. Kim, and T. W. Kim, "Recent advances in energy-saving chemiresistive gas sensors: A review," *Nano Energy*, vol. 79, no. July 2020. 2021, doi: 10.1016/j.nanoen.2020.105369.

[3] D. E. Schraufnagel *et al.*, "Air Pollution and Noncommunicable Diseases," *Chest*, vol. 155, no. 2, pp. 409–416, Feb. 2019, doi: 10.1016/j.chest.2018.10.042.

[4] Z. Zhang, T. Xue, and X. Jin, "Effects of meteorological conditions and air pollution on COVID-19 transmission: Evidence from 219 Chinese cities," *Sci. Total Environ.*, vol. 741, pp. 1–7, 2020, doi: 10.1016/j.scitotenv.2020.140244.

[5] A. Kushwaha, R. Kumar, and N. Goel, "Chemiresistive gas sensors beyond metal oxides: Using ultrathin two-dimensional nanomaterials," *FlatChem*, vol. 43, no. July 2023, 2024, doi: 10.1016/j.flatc.2023.100584.

[6] A. Hulanicki, S. Glab, and F. Ingman, "Chemical sensors definitions and classification," *Pure Appl. Chem.*, vol. 63, no. 9, pp. 1247–1250, 1991, doi: 10.1351/pac199163091247.

[7] T. Seiyama, A. Kato, K. Fujiishi, and M. Nagatani, "A New Detector for Gaseous Components Using Semiconductive Thin Films," *Anal. Chem.*, vol. 34, no. 11, pp. 1502–1503, 1962, doi: 10.1021/ac60191a001.

[8] J. W. G. and P. N. Bartlett, "Electronic Noses. Principles and Applications," *Meas. Sci. Technol.*, vol. 11, no. 7, pp. 1087–1087, Jul. 2000, doi: 10.1088/0957-0233/11/7/702.

[9] H. Yoon, "Current Trends in Sensors Based on Conducting Polymer Nanomaterials," *Nanomaterials*, vol. 3, no. 3, pp. 524–549, Aug. 2013, doi: 10.3390/nano3030524.

[10] C. Tan *et al.*, "Recent Advances in Ultrathin Two-Dimensional Nanomaterials," *Chem. Rev.*, vol. 117, no. 9, pp. 6225–6331, 2017, doi: 10.1021/acs.chemrev.6b00558.

[11] A. Bag and N. E. Lee, "Gas sensing with heterostructures based on two-dimensional nanostructured materials: A review," *J. Mater. Chem. C*, vol. 7, no. 43, pp. 13367–

13383, 2019, doi: 10.1039/c9tc04132j.

[12] X. Liu, S. Cheng, H. Liu, S. Hu, D. Zhang, and H. Ning, "A Survey on Gas Sensing Technology," *Sensors*, vol. 12, no. 7, pp. 9635–9665, Jul. 2012, doi: 10.3390/s120709635.

[13] T. Hübert, L. Boon-Brett, G. Black, and U. Banach, "Hydrogen sensors – A review," *Sensors Actuators B Chem.*, vol. 157, no. 2, pp. 329–352, Oct. 2011, doi: 10.1016/j.snb.2011.04.070.

[14] H. Manap, R. Muda, S. O'Keeffe, and E. Lewis, "Ammonia Sensing and a Cross Sensitivity Evaluation with Atmosphere Gases using Optical Fiber Sensor," *Procedia Chem.*, vol. 1, no. 1, pp. 959–962, Sep. 2009, doi: 10.1016/j.proche.2009.07.239.

[15] F. Fauzi, A. Rianjanu, I. Santoso, and K. Triyana, "Gas and humidity sensing with quartz crystal microbalance (QCM) coated with graphene-based materials – A mini review," *Sensors Actuators A Phys.*, vol. 330, p. 112837, Oct. 2021, doi: 10.1016/j.sna.2021.112837.

[16] V. Balasubramani, S. Chandraleka, T. S. Rao, R. Sasikumar, M. R. Kuppusamy, and T. M. Sridhar, "Review—Recent Advances in Electrochemical Impedance Spectroscopy Based Toxic Gas Sensors Using Semiconducting Metal Oxides," *J. Electrochem. Soc.*, vol. 167, no. 3, p. 037572, Jan. 2020, doi: 10.1149/1945-7111/ab77a0.

[17] N. Alanazi, M. Almutairi, and A. N. Alodhayb, "A Review of Quartz Crystal Microbalance for Chemical and Biological Sensing Applications," *Sens. Imaging*, vol. 24, no. 1, p. 10, Mar. 2023, doi: 10.1007/s11220-023-00413-w.

[18] J. B. A. Gomes, J. J. P. C. Rodrigues, R. A. L. Rabêlo, N. Kumar, and S. Kozlov, "IoT-Enabled Gas Sensors: Technologies, Applications, and Opportunities," *J. Sens. Actuator Networks*, vol. 8, no. 4, p. 57, Dec. 2019, doi: 10.3390/jsan8040057.

[19] C. Ferrag and K. Kerman, "Grand Challenges in Nanomaterial-Based Electrochemical Sensors," *Front. Sensors*, vol. 1, Sep. 2020, doi: 10.3389/fsens.2020.583822.

[20] S. Mao *et al.*, "Two-dimensional nanomaterial-based field-effect transistors for chemical and biological sensing," *Chem. Soc. Rev.*, vol. 46, no. 22, pp. 6872–6904, 2017, doi: 10.1039/C6CS00827E.

[21] X. Chen, C. Liu, and S. Mao, "Environmental Analysis with 2D Transition-Metal Dichalcogenide-Based Field-Effect Transistors," *Nano-Micro Lett.*, vol. 12, no. 1, p. 95, Dec. 2020, doi: 10.1007/s40820-020-00438-w.

[22] C. R. Kagan, "Molecular Monolayers as Semiconducting Channels in Field Effect Transistors," 2011, pp. 213–237.

[23] B.-Y. Kim *et al.*, "Highly Selective Xylene Sensor Based on NiO/NiMoO 4 Nanocomposite Hierarchical Spheres for Indoor Air Monitoring," *ACS Appl. Mater. Interfaces*, vol. 8, no. 50, pp. 34603–34611, Dec. 2016, doi: 10.1021/acsami.6b13930.

[24] Z. Yunusa, M. N. Hamidon, A. Kaiser, and Z. Awang, "Gas sensors: A review," *Sensors and Transducers*, vol. 168, no. 4, pp. 61–75, 2014, doi: 10.13074/jent.2015.12.153163.

[25] S. Kumar *et al.*, "Nanoparticles anchored strategy to develop 2D MoS2 and MoSe2 based room temperature chemiresistive gas sensors," *Coord. Chem. Rev.*, vol. 503, p. 215657, Mar. 2024, doi: 10.1016/j.ccr.2024.215657.

[26] H. Shin *et al.*, "Surface Activity-Tuned Metal Oxide Chemiresistor: Toward Direct and Quantitative Halitosis Diagnosis," *ACS Nano*, vol. 15, no. 9, pp. 14207–14217, Sep. 2021, doi: 10.1021/acsnano.1c01350.

[27] K. Barthelmi *et al.*, "Atomistic defects as single-photon emitters in atomically thin MoS2," *Appl. Phys. Lett.*, vol. 117, no. 7, Aug. 2020, doi: 10.1063/5.0018557.

[28] M. Zhu *et al.*, "Photo-induced selective gas detection based on reduced graphene oxide/Si Schottky diode," *Carbon N. Y.*, vol. 84, pp. 138–145, Apr. 2015, doi: 10.1016/j.carbon.2014.12.008.

[29] K. K. N. S.M. Sze, "Metal-Semiconductor Contacts," in *Physics of Semiconductor Devices*, Wiley, 2006, pp. 134–196.

[30] R. Purbia, Y. M. Kwon, H.-D. Kim, Y. S. Lee, H. Shin, and J. M. Baik, "Zero-dimensional heterostructures: N-doped graphene dots/SnO 2 for ultrasensitive and selective NO 2 gas sensing at low temperatures," *J. Mater. Chem. A*, vol. 8, no. 23, pp. 11734–11742, 2020, doi: 10.1039/D0TA03037F.

[31] A. Dey, "Semiconductor metal oxide gas sensors: A review," *Mater. Sci. Eng. B*, vol. 229, pp. 206–217, Mar. 2018, doi: 10.1016/j.mseb.2017.12.036.

[32] E. Llobet, "Gas sensors using carbon nanomaterials: A review," *Sensors Actuators B Chem.*, vol. 179, pp. 32–45, Mar. 2013, doi: 10.1016/j.snb.2012.11.014.

[33] X. Liu, T. Ma, N. Pinna, and J. Zhang, "Two-Dimensional Nanostructured Materials for Gas Sensing," *Adv. Funct. Mater.*, vol. 27, no. 37, Oct. 2017, doi: 10.1002/adfm.201702168.

[34] T. Ritter, J. Zosel, and U. Guth, "Solid electrolyte gas sensors based on mixed potential principle – A review," *Sensors Actuators B Chem.*, vol. 382, p. 133508, May 2023, doi: 10.1016/j.snb.2023.133508.

[35] J. Janata and M. Josowicz, "Conducting polymers in electronic chemical sensors," *Nat. Mater.*, vol. 2, no. 1, pp. 19–24, Jan. 2003, doi: 10.1038/nmat768.

[36] Z. Meng, R. M. Stolz, L. Mendecki, and K. A. Mirica, "Electrically-Transduced Chemical Sensors Based on Two-Dimensional Nanomaterials," *Chem. Rev.*, vol. 119, no. 1, pp. 478–598, Jan. 2019, doi: 10.1021/acs.chemrev.8b00311.

[37] S. Z. Butler *et al.*, "Progress, Challenges, and Opportunities in Two-Dimensional Materials Beyond Graphene," *ACS Nano*, vol. 7, no. 4, pp. 2898–2926, Apr. 2013, doi: 10.1021/nn400280c.

[38] J. Ma *et al.*, "Gas sensor based on defective graphene/pristine graphene hybrid towards high sensitivity detection of NO2," *AIP Adv.*, vol. 9, no. 7, Jul. 2019, doi: 10.1063/1.5099511.

[39] Z. Zanolli and J.-C. Charlier, "Defective carbon nanotubes for single-molecule sensing," *Phys. Rev. B*, vol. 80, no. 15, p. 155447, Oct. 2009, doi: 10.1103/PhysRevB.80.155447.

[40] B. Radisavljevic, A. Radenovic, J. Brivio, V. Giacometti, and A. Kis, "Single-layer MoS2 transistors," *Nat. Nanotechnol.*, vol. 6, no. 3, pp. 147–150, Mar. 2011, doi: 10.1038/nnano.2010.279.

[41] T. Kim, Y. Kim, S. Park, S. Kim, and H. Jang, "Two-Dimensional Transition Metal Disulfides for Chemoresistive Gas Sensing: Perspective and Challenges," *Chemosensors*, vol. 5, no. 2, p. 15, May 2017, doi: 10.3390/chemosensors5020015.

[42] D. M. Andoshe, J. M. Jeon, S. Y. Kim, and H. W. Jang, "Two-dimensional transition metal dichalcogenide nanomaterials for solar water splitting," *Electron. Mater. Lett.*, vol. 11, no. 3, pp. 323–335, 2015, doi: 10.1007/s13391-015-4402-9.

[43] G. Eda, H. Yamaguchi, D. Voiry, T. Fujita, M. Chen, and M. Chhowalla, "Photoluminescence from Chemically Exfoliated MoS 2," *Nano Lett.*, vol. 11, no. 12, pp. 5111–5116, Dec. 2011, doi: 10.1021/nl201874w.

[44] Z. Yin *et al.*, "Single-Layer MoS 2 Phototransistors," *ACS Nano*, vol. 6, no. 1, pp. 74–80, Jan. 2012, doi: 10.1021/nn2024557.

[45] B. Chakraborty, A. Bera, D. V. S. Muthu, S. Bhowmick, U. V. Waghmare, and A. K. Sood, "Symmetry-dependent phonon renormalization in monolayer MoS_2 transistor," *Phys. Rev. B*, vol. 85, no. 16, p. 161403, Apr. 2012, doi: 10.1103/PhysRevB.85.161403.

[46] A. Kushwaha, R. Kumar, and N. Goel, "Chemiresistive gas sensors beyond metal oxides: Using ultrathin two-dimensional nanomaterials," *FlatChem*, vol. 43, p. 100584, Jan. 2024, doi: 10.1016/j.flatc.2023.100584.

[47] H. J. Kim and J. H. Lee, "Highly sensitive and selective gas sensors using p-type oxide semiconductors: Overview," *Sensors Actuators, B Chem.*, vol. 192, pp. 607–627, 2014, doi: 10.1016/j.snb.2013.11.005.

[48] E. Lee, Y. S. Yoon, and D. J. Kim, "Two-Dimensional Transition Metal Dichalcogenides and Metal Oxide Hybrids for Gas Sensing," *ACS Sensors*, vol. 3, no. 10, pp. 2045–2060, 2018, doi: 10.1021/acssensors.8b01077.

[49] S. J. Choi and I. D. Kim, "Recent Developments in 2D Nanomaterials for Chemiresistive-Type Gas Sensors," *Electronic Materials Letters*, vol. 14, no. 3. The Korean Institute of Metals and Materials, pp. 221–260, 2018, doi: 10.1007/s13391-018-0044-z.

[50] A. V. Agrawal, N. Kumar, and M. Kumar, "Strategy and Future Prospects to Develop Room-Temperature-Recoverable NO2 Gas Sensor Based on Two-Dimensional Molybdenum Disulfide," *Nano-Micro Letters*, vol. 13, no. 1. Springer Singapore, 2021, doi: 10.1007/s40820-020-00558-3.

[51] D. Wang *et al.*, "Enhanced formaldehyde sensing properties of hollow SnO 2 nanofibers by graphene oxide," *Sensors Actuators B Chem.*, vol. 250, pp. 533–542, Oct. 2017, doi: 10.1016/j.snb.2017.04.164.

Chapter – 2

Synthesis and Characterization Techniques

CHAPTER – 2

SYNTHESIS AND CHARACTERIZATION TECHNIQUES

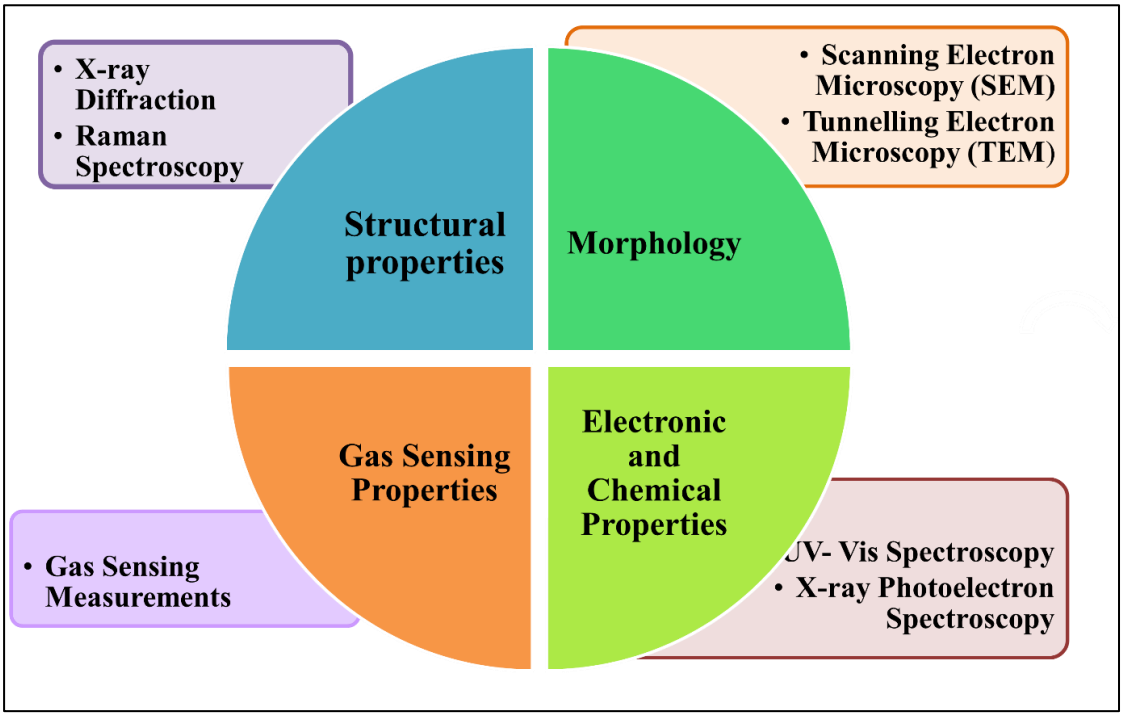

This chapter gives an extensive understanding of the preparation of nanostructured materials and various characterization techniques used in this research field. Additionally, it delves into the synthesis of the nanocomposite materials and the fabrication process of the gas-sensing devices, and instruments used for the electrical characterization and gas-sensing measurements of the fabricated devices. This chapter begins with a detailed description of the hydrothermal method and thermal chemical vapor deposition employed to obtain various nanostructures, and further the drop-casting process is used to prepare nanocomposite films. Followed by this, a brief description of various characterization techniques that are implemented for evaluating the different properties of the synthesized composites. X-ray diffraction (XRD) and Raman Spectroscopy are used to identify the crystal structure and different vibrational modes of the prepared nanostructures respectively. Scanning electron microscopy (SEM) and Transmission electron microscopy (TEM) are used to explore the surface morphology of the synthesized materials. X-ray photoelectron Spectroscopy (XPS) is used to determine the different chemical states of the synthesized nanocomposites.

Thermal evaporation is employed to deposit metal electrodes on the prepared thin films to prepare gas-sensing devices. This chapter also discusses the measures and setup used for gas-sensing measurements of the fabricated devices. All these routes are concisely discussed in this chapter.

2.1 Synthesis of 2D Materials

The central objective of this thesis is to synthesize large-area two-dimensional materials and understand the basics of gas sensing behavior to obtain highly selective gas sensors with lower operating temperatures. Special emphasis is given to the synthesis of nanocomposites of two-dimensional materials with different two-dimensional materials and variations in the growth orientation. Different synthesis techniques have been employed to obtain nanocomposite samples with different morphology. Various techniques are employed for the preparation and modification of two-dimensional materials, allowing the tuning of structures and properties to converge a wide range of applications. The synthesis techniques are mainly split into two categories: 1) Top-down, and 2) Bottom Up. The top-down method involves the exfoliation of bulk materials into layers by minimizing the interlayer interactions by applying different methods such as mechanical exfoliation, chemical reduction, or ultrasonic methods. On the other hand, the bottom-up method involves the production of 2D materials using atomic or molecular precursors that are proficient in reacting and growing to prepare a 2D material or self-assembled into a complex structured 2D material. Bottom-up approaches are more competent in producing 2D materials in large amounts in comparison to top-down [1]. The selection of a suitable synthesis route is important prior to exploring the properties of the desired applications. Synthesis techniques that were used to prepare the nanocomposite samples and gas sensing devices are as follows:

Hydrothermal Method

Chemical Vapour Deposition

2.1.1 Hydrothermal METHOD

A hydrothermal method is a type of bottom-up synthesis approach. It is one of the most widely used approaches for producing high-quality metallic, semiconducting

nanocrystals and nanomaterials. The hydrothermal technique is primarily a solution-based method, where nanomaterials can be developed in a wide range of temperatures from the room to a very high temperature. Depending on the vapor pressure of the main composition involved in the reaction, whether low-pressure or high-pressure conditions, a direct effect on the morphology of the prepared materials is observed. Using this approach, many nanomaterials can be successfully synthesized by controlling the morphology. Using high vapor pressure, nanomaterials with minimal loss of materials can be produced and along with this, the composition of synthesized nanomaterials can be well managed through liquid phase or multiphase chemical reactions in hydrothermal synthesis [2]. This method is most suitable for the thrifty and large-scale production of nanomaterials.

Under specific pressure and temperature conditions, hydrothermal synthesis takes place inside a Teflon-lined, sealed stainless-steel autoclave filled with chemicals dissolved in water or a combination of water and ethanol. The Teflon beaker is filled with a specific volume of aqueous reagents to provide the pressure needed to create the nanomaterials with the appropriate morphology and characteristics. Additionally, it's critical to maintain the regents' volume at a specific level to prevent Teflon overflow during the reaction.

By adjusting the reaction parameters in the high-temperature oven—such as pressure, temperature, and reaction duration—a considerable quantity of well-crystallized nanomaterials can be synthesized [3]. Figure 2.1 depicts the hydrothermal autoclave arrangement used for this purpose.

The components that contributed to the hydrothermal reaction are explained as follows:

1. **Precursors:** These substances are the reactants that are used in chemical reactions with appropriate solvents to yield the desired end product.
2. **Supplementary Agents:** Different acids and bases are added to the reaction to bring the pH level up to the desired level. These substances are called stabilizers, chelating agents, capping agents, reducing agents, and other additional agents. These agents are primarily in charge of providing the nanomaterials with their required morphology.

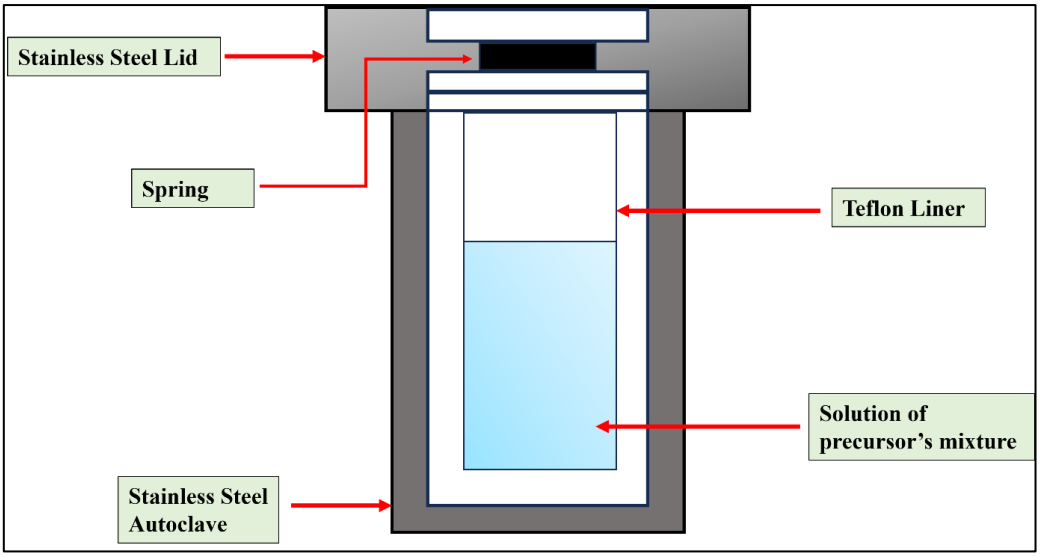

Fig. 2.1: Schematic of Teflon-lined stainless-steel autoclave used for hydrothermal synthesis

2.1.2 Chemical Vapor Deposition

CVD, or chemical vapor deposition, is a prime example of a bottom-up method. The primary goal of the CVD technique is to create large area, low defect density 2D materials with exact control over their morphology, thickness, and number of layers. To produce solid phase materials, a CVD process typically entails excitation of precursors to the necessary vaporous state, transit of reactant gaseous species, and heterogeneous surface reaction on the substrates [4]. Utilizing certain precursors transported by or combined with inert gases like argon (Ar), nitrogen (N_2), or hydrogen (H_2) gas to deposit these materials on substrates at high temperatures is a common method for the CVD development of 2D materials.

For the synthesis of 2D materials, CVD reactors are usually cylindrical and positioned horizontally inside a heated furnace. To maintain the high temperature during synthesis, quartz is the typical tube material utilized in the reactor to build 2D materials. The insulated boiler has one or three heating zones, and each zone can have a different temperature programmer. In addition to having distinct temperature programmers, three-zone furnaces may have heat transfer across the zones, which could cause the ultimate temperature to deviate from the setpoints that were programmed. Depending on whether the vapor phase precursors enter the reactor or are created inside the reactor, two types of CVD techniques are employed for 2D materials. First-type reactors are

filled with gas phase precursors (such as toluene or methane for carbon nanotubes), whereas second-type reactors are filled with solid phase precursors (such as sulfur and molybdenum trioxide for MoS_2). The solid precursors subsequently sublimate and condense into a vapor phase within the reactor's high-temperature zone. Depending on the temperature, growth duration, precursor concentrations, and carrier gas flow rates inside the reactor, growth is observed in both processes on the substrate and the quartz tube. The flow rates are typically quantified in standard cubic centimeters per minute (sccm)[5]. Figure 2.2 represents the basic phenomenon occurring during the deposition and shows the chemical vapor deposition setup.

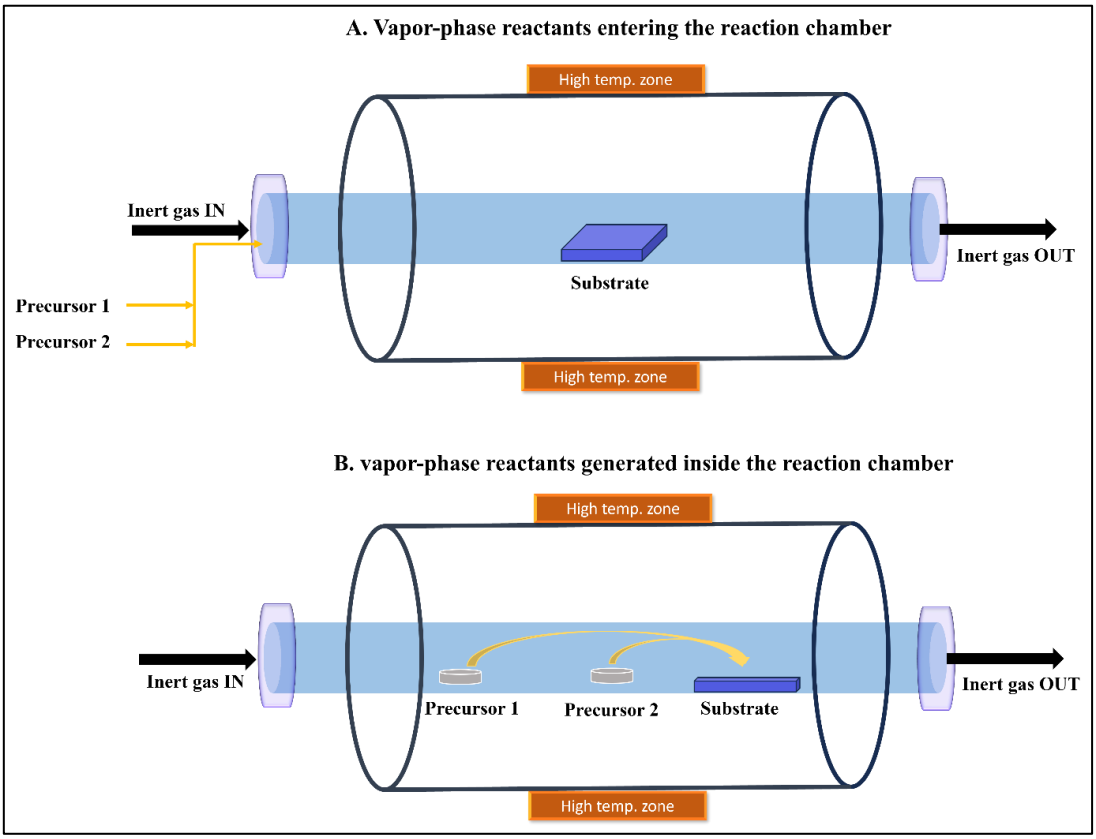

Fig. 2.2: Schematic illustration of CVD for A. gaseous precursor and B. solid precursors

2.2 Deposition of Thin Films

To fabricate the gas sensing devices, the electrodes on the SiO_2/Si substrate were deposited using the thermal evaporation technique, and after that drop casting technique was used to deposit the material as a thin film on the substrate.

2.2.1 Thermal Evaporation Technique

The sensing devices were fabricated using a shadow mask deposition of interdigitated electrodes of Au/Cr by thermal evaporation of Cr and Au wire (purity > 99.999 %) on the SiO_2/Si substrates by using photolithography which requires thermal evaporation of contact metallization. Thermal evaporation is one of the most extensively used pulse vapor deposition (PVD) techniques used for depositing thin films. The basic working principle of the thermal evaporation technique is the resistive heating of the Molybdenum (Mo) or Tungsten (W) boats to high temperatures which leads to the evaporation of the source material placed inside the boat.

The evaporated material further nucleates on the substrate and a thin film is deposited. This whole process requires high vacuum conditions inside the deposition chamber (< 10^{-6} mbar) to obtain a longer mean free path of the evaporated atoms compared to the distance between the evaporation source and the substrate. Initially, a rough vacuum (10^{-3} mbar) is achieved inside the chamber using a rotary pump, and then a high vacuum of 2× 10^{-6} mbar is attained through a diffusion pump. The main aim to attain high vacuum is to reduce the vapor pressure which is required to raise the vapor cloud of material inside the chamber.

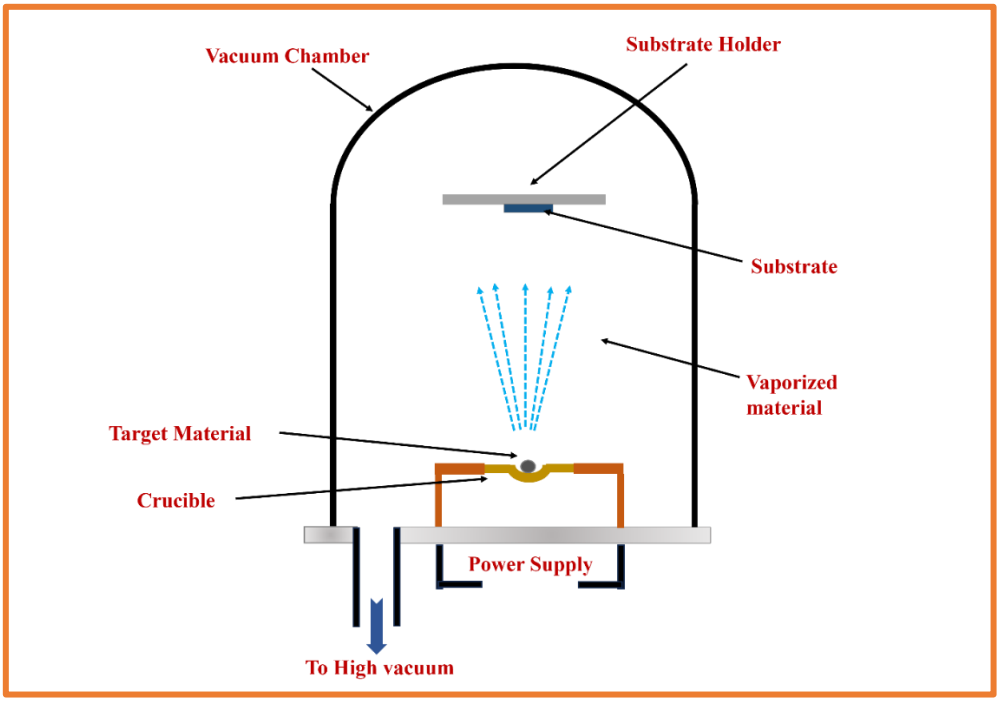

Fig. 2.3: Schematic representation of thermal evaporation technique

There are two gauges attached to the chamber to monitor pressure inside the chamber Penning gauge and the Pirani gauge. A transformer is used to pass the high currents through the Mo or W boats to evaporate the desired solid material placed in the boat. The evaporated material could travel through the chamber and form a thin film on the substrate placed in a facing-down position to the boat. The rate of deposition and thickness of the film deposited are monitored using a quartz crystal monitor. Figure 2.3 shows the basic representation of the thermal evaporation technique.

2.2.2 Drop Casting Approach

In this work, thin films for the gas-sensing devices were developed using the drop-casting approach. It is a straightforward process that involves solutes being dissolved at a consistent concentration in certain solvents. The drop-casting technique provides a simple and economical way to make thin films with precise composition and thickness. This technique, which works best for small-area deposition, involves dropping a predetermined volume of solution onto a stationary substrate and allowing it to evaporate for the appropriate length of time. Alternatively, the substrate can be baked to speed up the evaporation process [6]. A preset volume of the solution is taken into a micropipette and deposited onto a SiO_2/Si substrate that has already been pre-deposited with interdigitated electrodes, as shown in the drop-casting method schematic shown in Figure 2.4 (c).

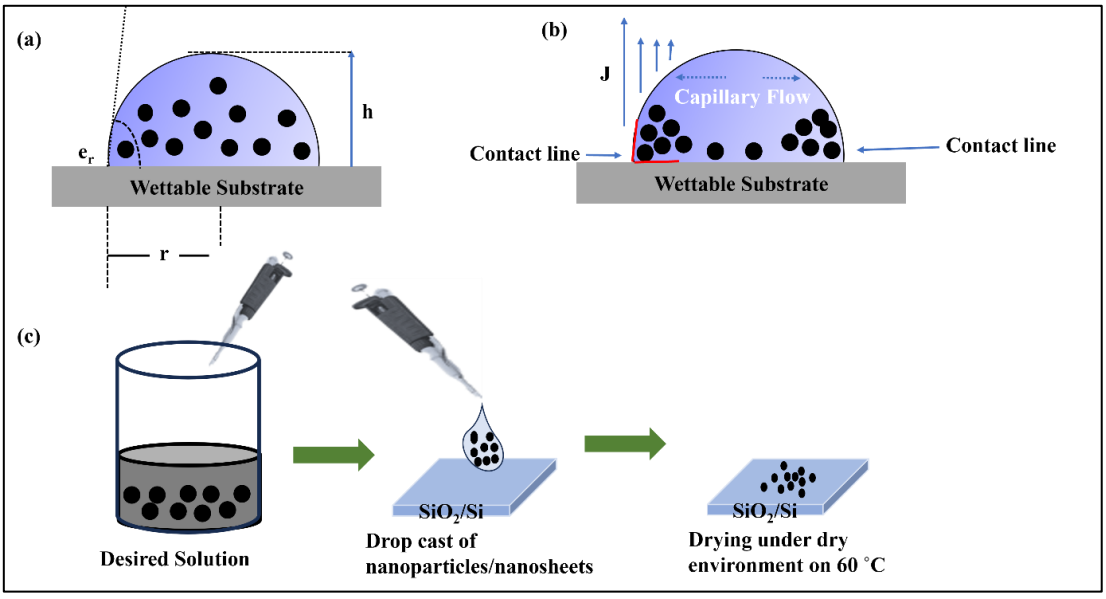

Fig. 2.4: Schematic representation of (a) droplet containing particles on depositing substrate, (b) capillary flow of particles towards edge during evaporation keeping contact line fixed, and (c) synthesis of thin films using drop casting technique. e_r= contact angle, h= droplet height, r= droplet radius, and J= evaporation flux

The straightforward approach of the drop-casting method is one of its key features. It makes it possible to quickly investigate how various solute concentrations, solvent choices, and deposition parameters affect the properties of the resulting thin films. However, this procedure can make it difficult to achieve uniform thickness and continuous coating on the deposition layer, which could affect the deposited layer's thickness variation and the properties of the resulting film.

2.3 Characterization Techniques

To verify that TMDCs nanostructures and TMDCs-based nanocomposites are successfully developed, a variety of characterization approaches are employed. To begin with, X-ray diffraction (XRD) is employed to study the structural properties which is further then confirmed by the Raman Spectroscopy by identifying the corresponding vibrational modes related to the nanostructures. To study the morphology, scanning electron microscopy (SEM) and Transmission electron microscopy (TEM) are performed. Additionally, to determine the available chemical states corresponding to the nanocomposites, X-ray photoemission spectroscopy is studied and discussed here. This section mainly focuses on the discussion of the operating principles of each of these characterizations and further, in this section, a brief review of the electrical measurements and the gas sensing measurements are also discussed that we have used in this work.

2.3.1 X-ray Diffraction (XRD)

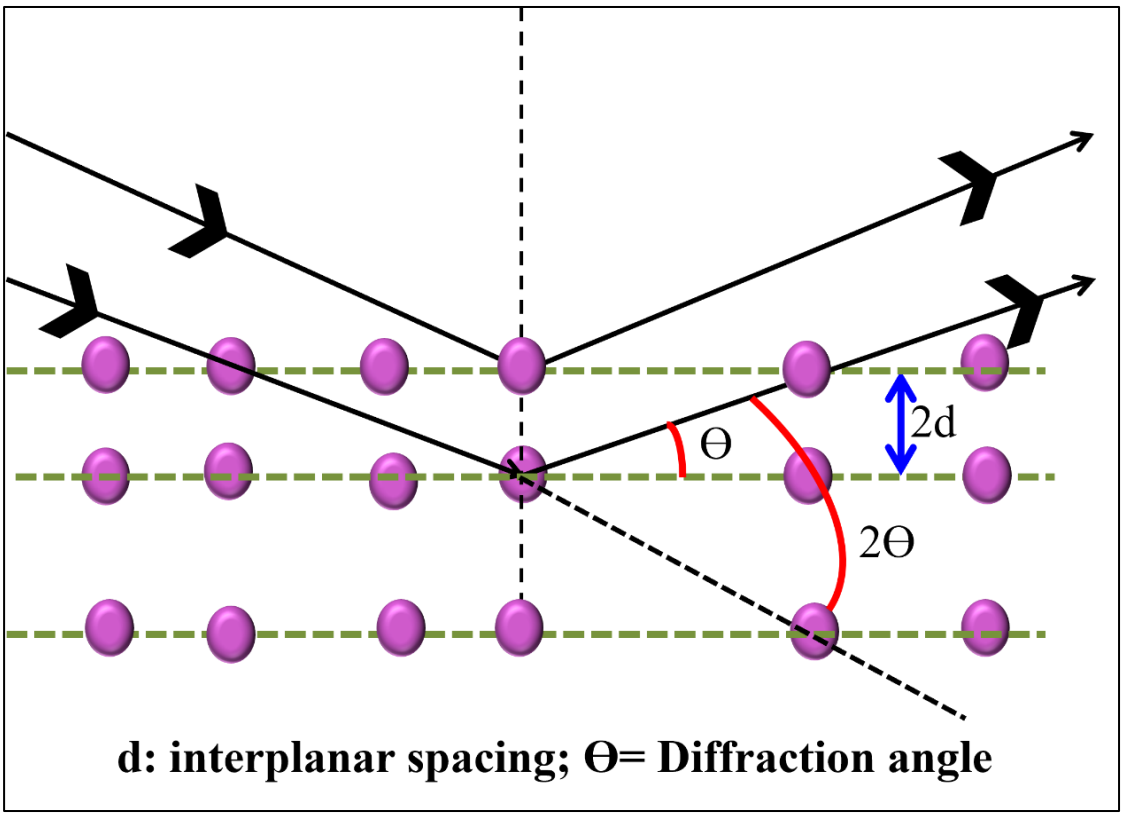

Fig. 2.5 Depiction of Bragg's law using diffraction of X-rays from the parallel planes

X-Ray Diffraction (XRD) is a non-destructive and highly versatile technique that is used to characterize crystalline materials. This technique provides information about crystal structures, atomic spacing, phase, and crystal orientation. In addition to chemical characterizations, XRD is very helpful for texture analysis and stress measurements [7]. In 1912, Max von Laue and coworkers determined that at X-ray wavelengths, crystalline materials exhibit three-dimensional grating behavior similar to the spacing between the planes in the lattice of a crystal [8]. The basis of X-ray diffraction is the constructive interference of a crystalline sample with monochromatic X-rays. Within the electromagnetic spectrum, X-rays are high-frequency waves with wavelengths ranging from approximately 0.5 to 2.5 Å. A cathode ray tube produces these X-rays, which are then collimated to concentrate them, filtered to produce monochromatic radiation, and directed toward the sample. For X-Ray diffraction (XRD), a crystal is assumed to contain atoms arranged in a set of parallel planes placed equidistant from each other, and each atom behaves as a scattering center. The rays scattered from each

atom have a phase relation with each other. When the scattered rays are in phase with each other, they undergo constructive interference to form a diffraction beam and on the other hand, out-of-phase directional rays annul each other. The constructive interference between the incident ray and the sample is produced when the arrangement satisfies Bragg's law as seen in Figure 2.5:

$$n\lambda=2d\sin\theta \tag{2.1}$$

where λ is the wavelength of the incident X-rays, d is the interplanar spacing, and θ is the angle between the incident beam and the specific diffraction plane. An integer value, n, indicates the order of diffraction (n=1,2,3…).

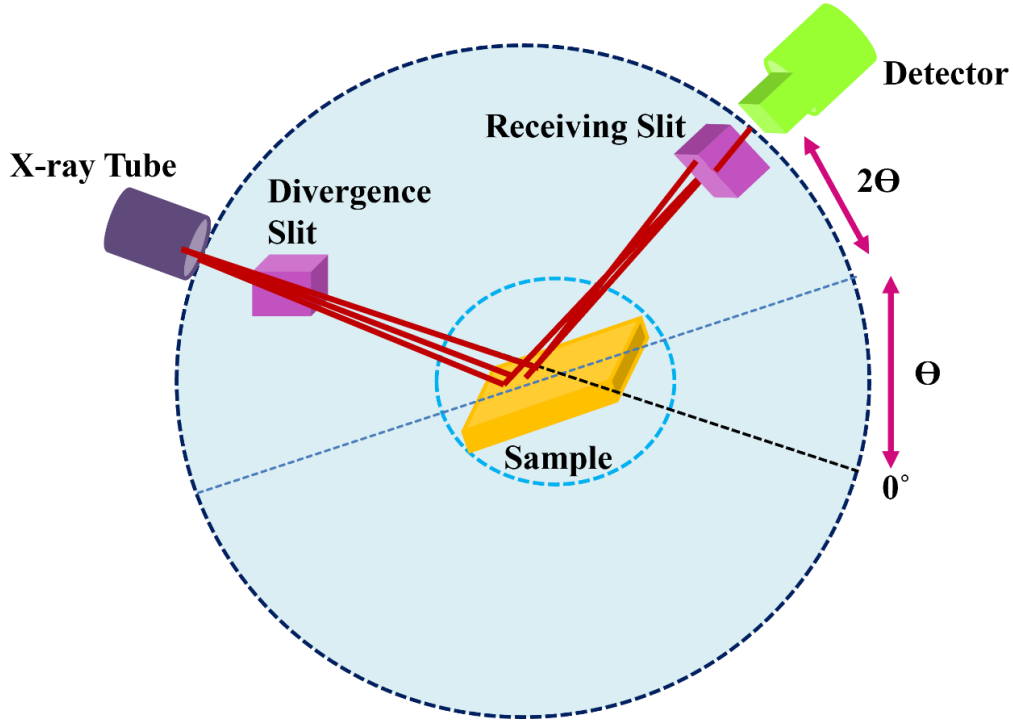

Fig. 2.6: Schematic illustration of X-ray Diffractometer

For wavelengths λ ≤ 2d, Bragg's reflection takes place in the X-ray range, which is the region where crystalline diffraction takes place. The size, space group symmetry, and crystal symmetry of the unit cell all influence peak positions. The intensity of the peak is determined by this collective interaction, as expressed by the equation:

$$F_{hkl} = \Sigma f_n e^{2\pi i(hu_n kv_n tw_n)} \tag{2.2}$$

Here, uvw represents the element coordinates, hkl represents the Miller indices, and f_n denotes the electron scattering density. The technique is frequently used on powdered samples; according to Bragg's law, the powder material interacts with the incident radiation by engaging with all possible planes within the substance. Peaks show up at different angles and for parallel surfaces, showing constructive interference. To obtain the information on crystallite diameters, X-ray diffraction is used by using the correlation shown in the equation:

$$D=k\lambda/\beta\cos\theta \quad (2.3)$$

X-ray diffractometer has three main components: X-ray tube, sample holder, and detector, the respective schematic diagram is given in Figure 2.6. The X-ray tube consists of a tungsten filament that acts as a cathode and generates a stream of electrons due to thermionic emission after the passage of high electrical current through it. The electrons are then accelerated towards anode material under a high electric field. When the bombarding electrons have sufficient energy to knock out the inner shell electrons of the anode materials, the characteristic X-ray beam is produced. The beam is then collimated onto the sample after passing through a divergence slit of variable aperture to control the length of the sample to be irradiated. X-ray tube and /or detector were then rotated over the goniometer circle to allow complete exposure of the sample. When the beam scattering satisfies Bragg's law, constructive interference occurs and an increase in intensity is recorded by detector which is then converted to a count rate and thereafter displayed over a computer screen as a function of 2θ. This graph is used to identify the phase and crystallographic orientation with the use of JCPDS cards.

The present study generated an XRD pattern with CuK_α radiation (λ= 1.54 Å) as an X-ray source. the X-ray tube was then rotated over the goniometer circle and the data was recorded for 2θ values from 10˚ to 80˚. The instrument recorded 2θ in step size of 0.05˚ and counts were accumulated at a scan speed of 2˚ per minute. The patterns were obtained at room temperature and subsequently compared with the JCPDS database and previously reported literature.

2.3.2 Raman Spectroscopy

The rotational, vibrational, and other frequency modes that materials display is identified via Raman spectroscopy. This non-destructive method provides details about the structure and bonding of the molecules. The method's operation can be explained from both a classical and quantum perspective.

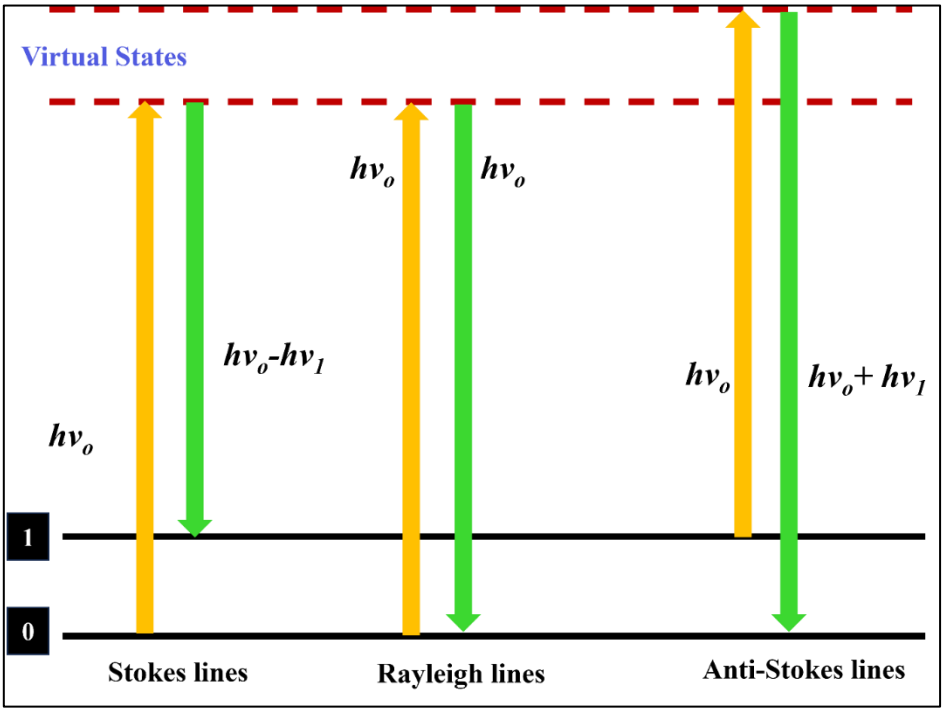

Fig. 2.7: Schematic illustration of Different types of Raman Scattering: Rayleigh Scattering, Stokes, and Anti-Stokes lines

Classical theory is based upon the ease of polarizability of the molecule, α, under the influence of light, considered as an oscillating electric field, $\varepsilon = \varepsilon^o \cos 2\Pi\nu_o t$, where ε^o is the equilibrium electric field strength and ν_o is the frequency of vibration. Upon interaction with material, it might induce a dipole moment of the same oscillating frequency. This induced dipole will then scatter radiation of frequency $\nu = \nu_o$.

$$\boldsymbol{\mu_i = \alpha\varepsilon^0 \cos 2\pi\nu_0 t}\ , \qquad (2.4)$$

$\boldsymbol{\mu_i}$ is the induced dipole moment.

As here, there is no gain or loss of energy involved, this elastic scattering is referred to as Rayleigh scattering. However, in the case of a molecule vibrating with its frequency $\nu_{vib,}$ the induced dipole moment gets modified to:

$$\mu i = \alpha^0 \varepsilon^0 cos2\pi\vartheta_0 t + \left(\frac{\delta\alpha}{\delta qv}\right)_0 \frac{\varepsilon 0 q 0 \times [cos2\pi(v0+vv)t + cos2\pi(v0-vv)t]}{2} \quad (2.5)$$

q_v is the coordinate along the axis of vibration at time t.

here, the induced dipole moment will scatter light with a frequency higher or lower than that of incident radiation, differentiated as anti-stokes and stokes lines, respectively. The scattering where no changes in frequencies of incident and scattered radiations are referred to as Rayleigh Scattering.

$$\nu = \nu_o \quad \text{Rayleigh Scattering} \quad (2.6)$$

$$\nu = \nu_o \mp \nu_v \quad \text{Raman Scattering} \quad (2.7)$$

Quantum theory is based on the quantization of the vibrational energy of the molecules, $E = h\nu (n+1/2)$, where E is the vibrational state energy, n is the vibrational energy state number (n =0,1,2,…) and ν is the frequency of vibration. The incident photons excited the molecule to a virtual energy level at a higher state. However, the molecule cannot stay in a virtual energy state for long, it falls back to a lower energy state. If the initial energy state and final energy state are the same, Rayleigh scattering takes place i.e. photons with the same energy (frequency), $\nu = \nu_o$ is emitted. Whereas, in stokes scattering, the final energy state is lower than the initial energy state, i.e. $\mathbf{\nu = \nu_o - \nu_v}$. For anti-stokes scattering, the final energy state is higher than the initial energy state, here frequency of scattered photons is higher than incident emitted photons, $\mathbf{\nu = \nu_o + \nu_v}$. The simplified mechanism design of the Raman spectrometer is explained in Figure 2.7.

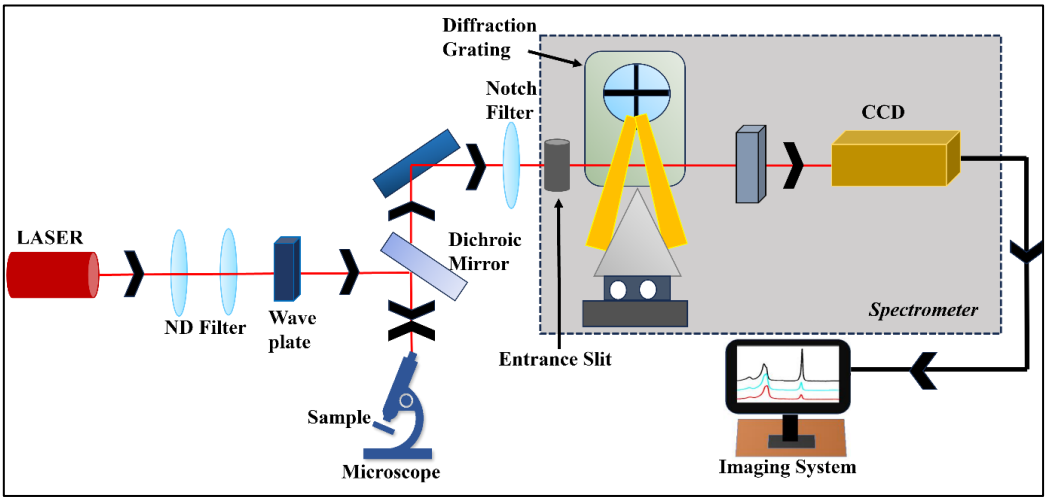

Fig. 2.8: Instrumental representation of Raman Spectrometer

In the present work, a Micro-Raman Spectrometer from Horiba Scientific, Model-LabRAM HR Evolution is used and a schematic is depicted in Figure 2.8. Raman Spectra were collected using a 514 nm diode laser with intensity < 10 mW to prevent the sample from damage.

The diffraction system consists of a confocal holographic diffraction grating (1800 lines/mm) and the detector system contains an ultra-sensitive low-noise charge-coupled detector (CCD). A laser beam is irradiated onto the sample through a combination of a dichroic mirror, wave plate, and neutral density filter (ND). Incident light scattered from the sample will consist of both the Rayleigh and scattered light. A notch filter is used to filter out the scattered Stokes light from Rayleigh and anti-Stokes, and hereafter the Stokes light is passed through a holographic diffraction grating via an entrance slit which distributes it according to its wavelength (like a prism). Thereafter, the light is captured by the CCD array detector which outputs the light according to the intensity of different wavelengths and hence records a vibrational spectral graph on the computer screen attached to it. The spectral graph represents the intensity of diffracted light as a function of wavenumber.

2.3.3 UV- Vis Spectroscopy

UV-Vis Spectroscopy is a technique used to examine how a material absorbs and reflects light in the UV spectral region. In this method, electrons are excited to a higher energy level through the absorption of UV radiation. The energy difference between the lower and higher energy levels is equivalent to the energy of the UV light that is absorbed. Using this technique, the absorber concentration in the solution of conjugated organic molecules and transition metal ions is quantitatively evaluated. High anti-bonding molecular orbitals can be stimulated in molecules with π-electrons or non-bonding electrons by absorbing ultraviolet or visible light energy.

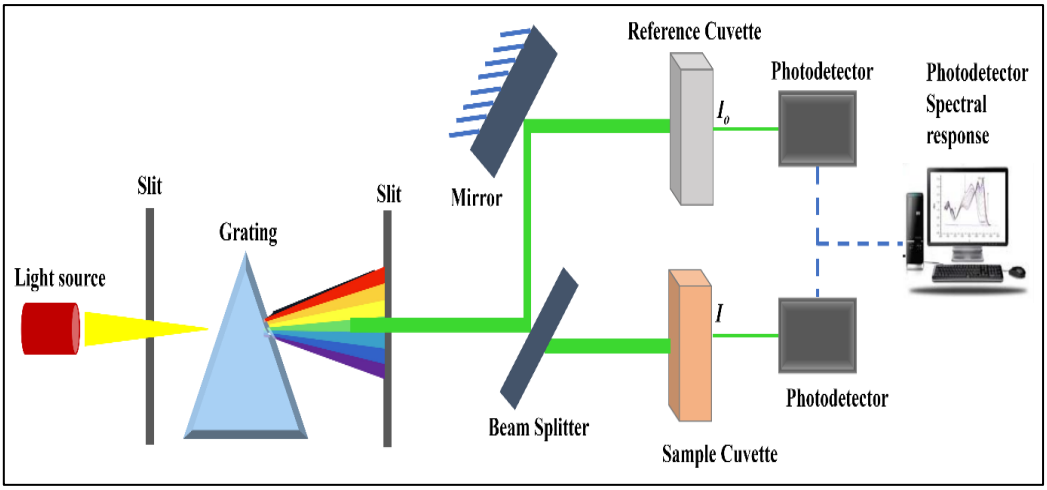

Fig. 2.:9 Schematic representation of UV-Vis Spectrometer

Beer-Lambert's Law provides the framework of a UV spectrometer's basic functionality. The rate at which light intensity decreases when an absorbent material solution is exposed to a monochromatic laser beam is dependent on the solution's thickness. It is proportional to the laser light's incidence intensity.

$$A = \log_{10} (I_o/I) = \varepsilon cL \qquad (2.8)$$

where L is the path length through the sample, c is the concentration of the absorbing species, I_o is the incident light intensity at a given wavelength, I is the transmitted intensity, and ε is a constant known as the molar absorptivity or excitation coefficient for each species and wavelength [9].

The main components of UV-visible spectroscopy consist of a light source, monochromator, chopper, sample container, detectors, amplifier, and recorder. H_2-D_2 lamps (300-375 nm) and tungsten filament (375-800 nm) are the typical light sources and cover a wider range of wavelengths up to the ultraviolet region and are very efficient. Through the entrance slit, a monochromator transforms polychromatic light into monochromatic light. A collimating lens collimates the beam, while a prism or grating disperses it. The beam with a specific wavelength is reflected towards the existing slit by the reflecting lens. A certain wavelength can be adjusted such that radiation exiting the monochromator through the built-in lens is at that wavelength. The monochromator's output beam splits into two beams using a chopper; one beam travels through the sample and the other through the reference. Radiation transparency is required for both the sample

and reference solution cuvettes. Quartz or fused silica cuvettes are used as sample containers for UV-visible spectroscopy. Charge-coupled detectors (CCDs) are silicon-based multichannel array photodetectors that are useful for capturing UV-visible spectra. An amplifier records all the data, multiplexes the signals from the detector to create a readable signal, and generates the spectrum of the desired molecule. Figure 2.9 shows the basic diagram of the UV visible spectrometer. With the use of a UV spectrometer, the materials' bandgap can be determined. The bandgap is measured using the Tauc plot. The approach known as the Tauc plot, initially presented by Tauch in 1966, is predicated on the belief that energy is a function of absorbance coefficient α. Additionally, Davis and Mott developed a similar technique for semiconductors and discussed how the difference between photon energy and bandgap energy affects optical absorbance. The Tauc equation for semiconducting material is given by:

$$(\alpha h\nu)^{1/n} = B(h\nu - E_g) \tag{2.9}$$

where α is the absorbance coefficient, n is a quantity that depends on the transition property, B is constant, v is the photon frequency, E_g is the band gap energy, and h is Planck's constant. For a direct bandgap transition, the value of n is 2, and for an indirect bandgap transition, it is ½. α= ln(10)A/l yields the absorbance coefficient, where A denotes absorbance and l represents the material's thickness in centimeters [10] [11].

Plotting $(\alpha h\nu)^{1/n}$ with hν and then extrapolating in the linear area across the energy axis in the related graph yields the bandgap energy. The estimated matching energy gap is located at the junction with the energy axis.

2.3.4 Electron Microscopy

Incident electron beams can interact with matter and produce different radiations depending upon the energy of the incident electrons, atomic number, and matter density. As the interaction between the electron and coulombic field generated by a primary electron with sample nuclei results in a deviation of the path of the primary electron without significant loss of energy (i.e. elastic scattering), backscattered electrons (BSE) are emitted. Their scattering depends upon the atomic number and density of the sample, which is further used as compositional contrast. In the inelastic scattering of primary electrons, the energy loss is enough to remove an inner shell electron from the sample, and the emitted electrons are called

secondary electrons (SE). SE possesses low energy (< 50 eV) and is emitted from near the surface (5 to 50 nm), used to study surface morphology and topography. If a higher-level orbital electron fills up the vacancy created by the SE, the energy released upon their recombination gives characteristic X-ray photons.

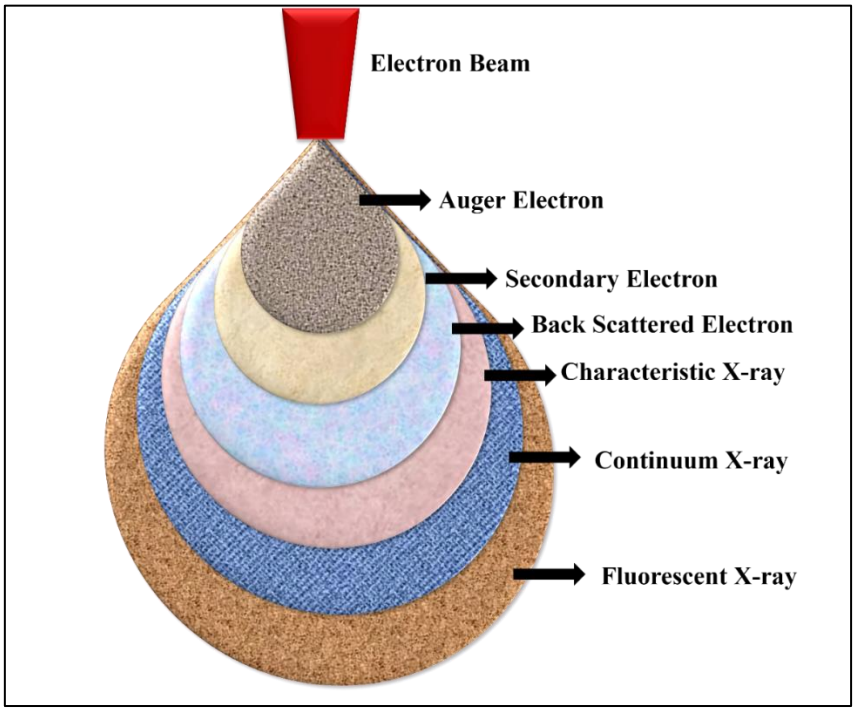

Fig. 2.10: Schematic representation of electron-matter interaction

2.3.4.1 Scanning Electron Microscopy (SEM)

SEM is a sophisticated type of microscopy that uses electrons rather than light to determine the three-dimensional structure of solid materials. This method offers a thorough understanding of a sample's morphology, topography, and content. With dimensions ranging from nanometers to micrometers and magnifications reaching 30,000x and even 100,000x, scanning electron microscopy (SEM) is the best tool for obtaining extremely accurate pictures for analyzing both organic and inorganic materials. Electromagnetic lenses are used in SEMs to concentrate electron beams onto samples. Materials like metals, metal oxides, ceramics, or biological specimens could be included in the sample. The interactions between the electron beam and the specimen's surface are then captured to create a picture. Deflection of various types of electrons occurs as a result of the interaction between an electron beam and the sample.

Samples for SEM investigation are prepared by covering them with conducting metals such as platinum (Pt) or gold (Au) after they have been dispersed, thin-film applied, or pellets arranged over conductive carbon tape [12]. The sample will be fixed in the sample holder following the sample wrapping. The operating principle of the SEM equipment is based on the idea that the specimen's atomic electrons, which are emitted as SEs, are energized by the primary electrons released from the source. An image is created by gathering these secondary electrons from every location throughout the sample. SEMs must function in a vacuum to prevent interactions between the electrons that are created and released from the electron cannon, which are accelerated by high energy applied in the 1–40 keV range. These released electrons are concentrated and limited by metal slits and magnetic field lenses inside a vacuumed column to a monochromatic beam with a width of 100 nm or less. Scanning coils in a bitmap pattern move the restricted primary electrons over the sample surface. After the primary electron touches the surface of the sample, it will engage in a variety of interactions with the sample's near-surface region down to a certain depth. The specimen's atomic concentration, accelerating voltage, and atomic number all affect how electrons scatter and interact. Higher atomic number materials absorb or block more electrons, resulting in less volume interaction. In a similar vein, using a high accelerating voltage will produce highly energetic electrons that further penetrate the material.

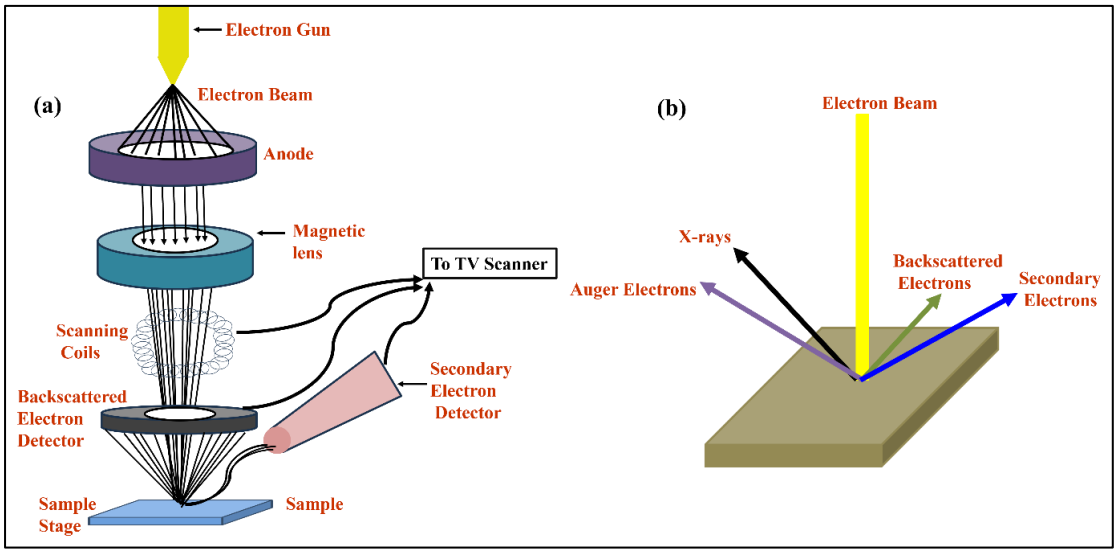

Fig. 2.11: Schematic representation of (a) instrumentation of scanning electron microscopy, and (b) Scattering of electrons

The electron gun, vacuum, and column make up the majority of the SEM's apparatus. Additional components of the column unit include a sample holder, detector, condenser lens, scanning coil, and objective lens. The gun emits an electron beam that is contained in a vacuum and travels vertically through lenses and electromagnetic fields. After the electron beam has been focused by an objective lens on the specimen surface, detector coils that are managed by the scan generator are used to raster the focused beam across the material's surface. The rastering pattern's size is altered by magnification. Electrons and X-rays are released from the specimen when the electron beam strikes the material, and an array of signals is generated. The detector catches up with these signals and transforms them into the signals that are used to create images. The primary advantage of SEM is that, when lenses are substituted with electromagnets, it offers the researcher a great deal of control over the magnification level [13]. A visual depiction of fundamental SEM components is described in Figure 2.11.

2.3.4.2 Transmission Electron Microscope

The crystallinity of the as-grown samples was examined in the current investigation using TEM. A transmission electron beam (TEM) is a microscopic technique that passes through an extremely thin specimen and interacts with it to provide information about it. According to quantum mechanics, the idea of wave-particle duality can be applied to define electrons, just like it does light. The difference is that an electron's wavelength depends on its speed, even though both can have varied speeds and wavelengths. As the accelerating voltage and resolving power increase, the wavelength decreases. Higher magnification in TEM usually results in a smaller region being illuminated by the beam of light. However, the interactions between the beam and the sample also decrease at higher working voltages, which results in pictures with less contrast. The sample may sustain significant damage from beam radiation exposure with an operating voltage typically between 80 and 300 keV. This damage could manifest as de-crystallization and re-confirmation of atomic bond breaking, or simply as a loss of mass. Conversely, a noisy image will result from an exposure to a low-voltage electron beam. The signal-to-noise ratio (S/N), contrast, and resolution of an image determine its quality. Electron microscope resolution has increased with time, going from 100 nm to 0.1 nm. The electron travels from top to bottom via the column's high vacuum for around one to two meters [14]. Figure 2.12 shows the basic setup of the TEM instrument.

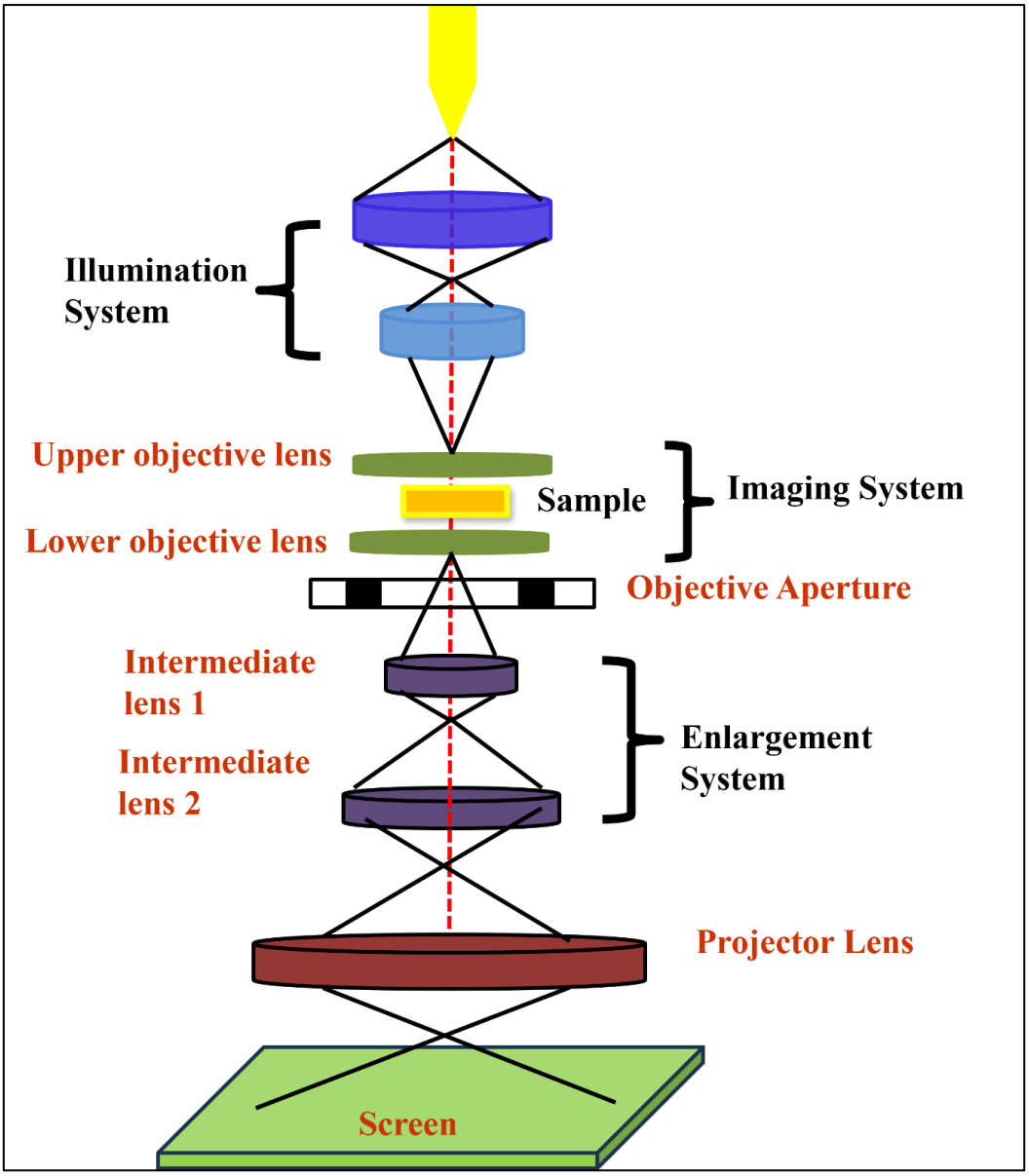

Fig. 2.12: Schematic illustration of the instrumentation of Transmission electron microscopy

An electron gun, condenser lenses, specimen holders, objective lenses, projector lenses, screen/camera, and specimen holders are the basic parts of a TEM. Each of these components might have a different design and contain several elements that add to the overall quality of the image. A condenser lens gathers the electron beam that is emitted from an electron cannon and uses it to send electrons toward the specimen in two ways: either as a focussed beam or as parallel beam images. To generate high-resolution images with diffraction patterns, an imaging system comprising objective and projector lenses is needed. After passing through the item, the electron intensity distribution is projected onto

a fluorescent screen using a three-stage lens system [15]. Finally, the electric charge is converted into picture pixels using a charge-coupled device (CCD) camera.

The incident beam will suffer scattering while passing through the specimen and the beam exited from the specimen will comprise a direct beam and scattered beam, which will result in a non-uniform spatial or angular distribution of electrons. The direct beam is for the contrast in TEM images and the scattered beam is used for the diffraction pattern (DP). The imaging system uses a combination of intermediate, diffraction, and a projector lens to magnify the diffraction pattern formed by the objective lens and display it over a computer screen via a CCD detector.

The entire TEM setup is stored in a high vacuum chamber and is connected to a data-collecting device with a graphical user interface (GUI). The differentiation between images is based on both dark-field and bright-field imaging. The specimen is evenly illuminated in a bright-field image, producing a black image against a brilliant background. On the other hand, a diffracted wave passes through the objective aperture to create a Dark-field image on the back focal plane of the objective lens. The sample used in TEM must be electron-transparent. The dimensions of the nanostructures act as a diffraction grating for incoming electrons and electrons scattered at different angles depending upon the crystal structure, satisfying Bragg's law.

2.3.5 X-Ray Photoelectron Spectroscopy (XPS)

The elemental, electrical, and chemical states at the surface of a variety of materials can be investigated using XPS, a powerful quantitative approach that is sensitive to surface conditions. The term Electron Spectroscopy for Chemical Analysis (ESCA) is another name for the technique. The basic principle of XPS is the photoelectric effect, or photoemission, which Hertz initially discovered in 1887. This phenomenon occurs when a photon strikes a sample; the electron is subsequently expelled and escapes into the vacuum as a result of the photoelectric effect. The incident photon's energy can fall into one of three categories: hard X-ray (> 1000 eV, XPS), soft X-ray (100 to 1000 eV, SXPS), or ultraviolet (5 to 1000 eV, UPS). In an electron energy analyzer, incident light on the sample and electrons excited by the photoelectric effect are analyzed with respect to the momentum p (wave vector p/ħ) and the kinetic energy (K.E.) of the emitted photoelectrons.

$$E_{kin.} = \hbar\omega - E_B - \phi \quad (2.10)$$

Here, ϕ is the work function of the analyzer, E_B is the binding energy, and $\hbar\omega$ is the photon's energy. The schematic diagram of the XPS setup is shown in Figure 2.13.

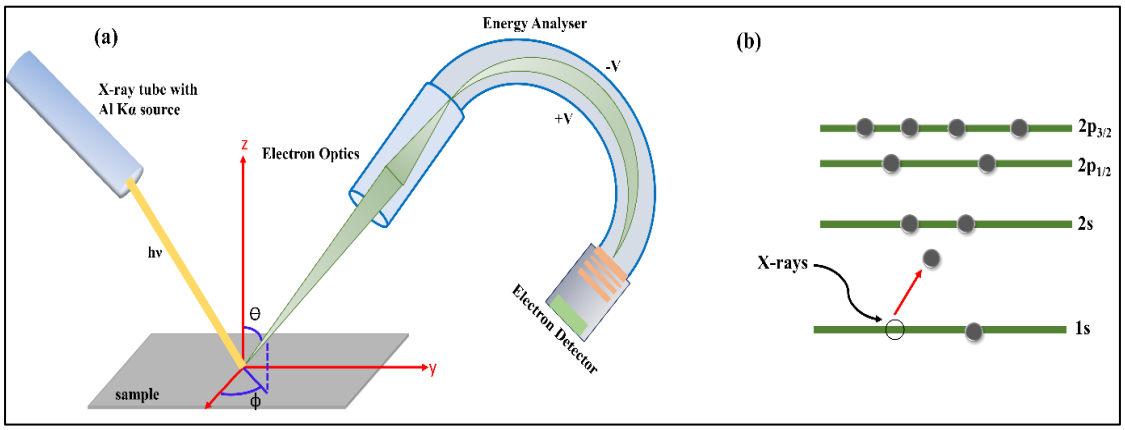

Fig.2.13: Schematic representation of (a) X-ray photoemission spectroscopy setup, and (b) process of ejection of core-level electron on the absorption of X-ray photon

An ultra-high vacuum system (UHVS), an X-ray source, an electron analyzer, and an ion gun comprise the components of the XPS apparatus. Longer photoelectron pathways are provided by UHVS to preserve surface cleanliness and protect against contamination. The energy of the X-ray sources that are employed is either 1253.6 eV for Mg K_α radiation or 1486.6 eV for Al K_α radiation. The analyzer filters electron energies and counts electrons using a detector. It also has a lens system to gather photoelectrons. Next, an ion gun for depth profiling and sample cleaning (Ar^+ is the most often employed ion). The detected electron provides useful details on several atomic species that are present close to the sample surface, typically at a depth of approximately 10 nm. Furthermore, a small change in binding energy, sometimes referred to as a chemical shift, is also advantageous. Different peaks in XPS spectra may appear at various binding energies, owing to varying core states on the surface of the sample. XPS spectra can be used to detect this oxidation state as well as the chemical shift of the chemical species at a specific binding energy.

From a depth of d, a photoelectron is emitted with an initial intensity of Io and an intensity at which the electrons knock-off of the surface, respectively. This phenomenon can be explained using Beer-lambert as shown in Equation (2.10):

$$I_s = I_o\, e^{-d/\lambda} \tag{2.11}$$

The electron's inelastic mean free path is shown by λ in the equation above. In this case, "d" represents the thickness, which is typically reached at a depth of around 3λ, often referred to as the sampling depth, and at which 95% of photoelectrons are dispersed when emerging to the surface. The value of λ for Al K_α radiation is around 1-3 nm, resulting in a sample depth of 3-10 nm. The element's electron binding energy varies for various oxidation states. In general, the neutral atom has a lower core electron binding energy than the ion. The spin-orbit interaction that results in the doublet states is what produces the core-level spectra of the XPS pattern. The core electrons of each surface atom have a unique binding energy, and the material's possible valence states and chemical bonding can be deduced from the core-level shift of these electrons.

The data is represented in terms of the intensity versus B.E. of the electrons calculated from the Kinetic energy of the core-level electrons. The XPS data included in this thesis utilized a monochromatic X-ray source Al K_α of energy 1486.6 eV. the XPS spectra were fitted in CasaXPS by using a Shirley Background. The current study determined elemental and chemical states using X-ray photoelectron spectroscopy.

2.4 Electrical and Gas Sensing Measurements

2.4.1 Electrical Measurements

The resistivity, mobility, depletion width, barrier height, carrier concentration, and contact resistance of the material are all determined via electrical characterization. To determine whether the fabricated materials are ohmic or Schottky junctions, the current work has employed electrical characterizations to measure the current-voltage (I-V) relationship of the materials. In this study, the electrical characteristics of both Ohmic and Schottky junctions have been examined using the two-probe technique. First, the output probes were linked to the source meter (Keithley-4200 SCS) and two probes were attached to the metal contact on the I-V characterization system. The heterojunction characteristics of this source meter are measured when a constant voltage is applied and the corresponding current is altered. To examine the electrical characteristics of the device, a voltage of -3 V to +3 V was supplied in both forward and reverse bias during the test.

2.4.2 Gas Sensing Measurement

A gas-sensing chamber setup, optimized for various gases, has been employed to examine the properties of the gas sensor. The detecting chamber is built out of stainless steel and has a gas inlet/outlet port. This closed sensing chamber's primary function is to provide isolation from the outside world when exposed to poisonous and dangerous gases. The schematic depiction of the experimental gas sensing apparatus is shown in Figure 2.14. To prevent external impacts during gas sensing, the gas-sensing chamber was first emptied up to around 1×10^{-2} mbar with the use of a rotary pump. Throughout the measurements, the overall chamber temperature is kept close to room temperature (RT) because of the heater's tiny size and steady airflow. A heater that is linked to the gas sensing platform's external DC supply and has a variac for temperature control can be used to apply the high operating temperature to the sensor. The primary objective is to subject the sensor to a moderate temperature to confirm its low-power operation. A standard hygrometer was used to measure the percentage relative humidity (% RH) after the analyte gas was mixed with humidifier air that had been generated using a bubbler. Different kinds of gas cylinders (1% and 5%) are attached to the sensing chamber's inlet port for the gas sensing test.

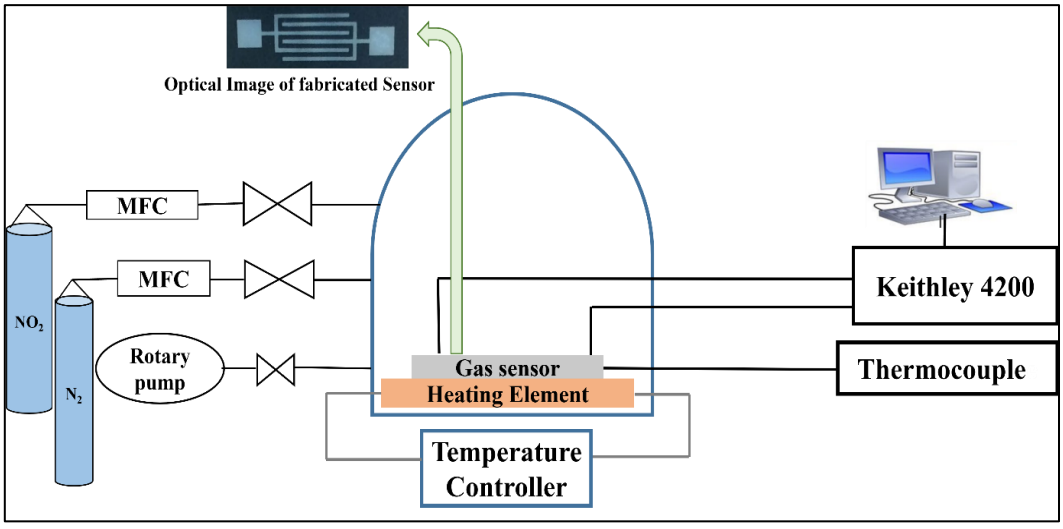

Fig. 2.14: Schematic Representation of the typical gas sensing setup

A specific volume of gas is then introduced into the sensing chamber, which modifies the baseline after a sensor's baseline on the computer screen stabilizes. The output port

of the sensing chamber is opened and the gas sensing response curve is recorded as soon as the gas sensing response is saturated. The sensor's electrical resistance was measured in a gas environment that changed frequently, alternating between dry air and target gases such as CO, NO_2, and NH_3, at varying concentrations and temperatures. The relative humidity was kept constant at 40% RH throughout all measurements to ascertain the device's gas-sensing capabilities. By monitoring the sensor response towards the target analyte gas, the working temperature of each device is first optimized. The sensing response was then assessed against various NO_2 and NH_3 gas concentrations at a constant operating temperature. to reach a state of equilibrium. Before measurements, each sample was dried and allowed to stabilize at a specific temperature. $(|R_g-R_a|)/R_a\times$ 100% is the definition of the relative response (R) of the sensor, where R_g and R_a are the sensor's resistances in the presence of target gas mixed with dry air and dry air, respectively. After the analyte gas is present, the response time is the amount of time needed to reach 90% of the maximum resistance; after the analyte gas is removed, the recovery time is the amount of time needed to reach 10% of the minimum resistance value.

References

[1] V. Shanmugam *et al.*, "A Review of the Synthesis, Properties, and Applications of 2D Materials," *Part. Part. Syst. Charact.*, vol. 39, no. 6, 2022, doi: 10.1002/ppsc.202200031.

[2] Y. X. Gan, A. H. Jayatissa, Z. Yu, X. Chen, and M. Li, "Hydrothermal Synthesis of Nanomaterials," *J. Nanomater.*, vol. 2020, 2020, doi: 10.1155/2020/8917013.

[3] J. W. Jianlin Li, Qingliu Wu, "Synthesis of Nanoparticles via Solvothermal and Hydrothermal Methods," *Handb. Nanoparticles*, no. February, pp. 1–1426, 2015, doi: 10.1007/978-3-319-15338-4.

[4] P. C. Shen *et al.*, "CVD Technology for 2-D Materials," *IEEE Trans. Electron Devices*, vol. 65, no. 10, pp. 4040–4052, 2018, doi: 10.1109/TED.2018.2866390.

[5] S. Bhowmik and A. Govind Rajan, "Chemical vapor deposition of 2D materials: A review of modeling, simulation, and machine learning studies," *iScience*, vol. 25, no. 3, pp. 1–32, 2022, doi: 10.1016/j.isci.2022.103832.

[6] Y. Yunus *et al.*, "Review of the Common Deposition Methods of Thin-Film Pentacene, Its Derivatives, and Their Performance," *Polymers (Basel).*, vol. 14, no. 6, 2022, doi: 10.3390/polym14061112.

[7] S. Nasrazadani and S. Hassani, "Modern analytical techniques in failure analysis of aerospace, chemical, and oil and gas industries," in *Handbook of Materials Failure Analysis with Case Studies from the Oil and Gas Industry*, Elsevier, 2016, pp. 39–54.

[8] J. J. Thomson and P. Knipping, "The birth of X-ray crystallography," *Nature*, vol. 491, pp. 186–187, 2012.

[9] H. Wang and P. K. Chu, "Surface Characterization of Biomaterials," in *Characterization of Biomaterials*, Elsevier, 2013, pp. 105–174.

[10] V. Mursyalaat, V. I. Variani, W. O. S. Arsyad, and M. Z. Firihu, "The development of program for calculating the band gap energy of semiconductor

material based on UV-Vis spectrum using delphi 7.0," in *Journal of Physics: Conference Series*, 2023, vol. 2498, no. 1, pp. 0–5, doi: 10.1088/1742-6596/2498/1/012042.

[11] P. Makuła, M. Pacia, and W. Macyk, "How To Correctly Determine the Band Gap Energy of Modified Semiconductor Photocatalysts Based on UV-Vis Spectra," *J. Phys. Chem. Lett.*, vol. 9, no. 23, pp. 6814–6817, 2018, doi: 10.1021/acs.jpclett.8b02892.

[12] A. Mohammed and A. Abdullah, "Scanning Electron Microscopy (SEM): a Review," *Proc. 2018 Int. Conf. Hydraul. Pneum. - HERVEX*, no. January, pp. 77–85, 2018.

[13] K. Akhtar, S. A. Khan, S. B. Khan, and A. M. Asiri, *Scanning electron microscopy: Principle and applications in nanomaterials characterization*. 2018.

[14] L. E. Franken, K. Grünewald, E. J. Boekema, and M. C. A. Stuart, "A Technical Introduction to Transmission Electron Microscopy for Soft-Matter: Imaging, Possibilities, Choices, and Technical Developments," *Small*, vol. 16, no. 14. 2020, doi: 10.1002/smll.201906198.

[15] L. A. Bendersky and F. W. Gayle, "Electron Diffraction Using Transmission Electron Microscopy," *J. Res. Natl. Inst. Stand. Technol.*, vol. 106, no. 6, pp. 997–1012, 2001, doi: 10.6028/jres.106.051.

Chapter – 3

Effect of Varying the Precursors' Concentration on Structural and Electronic Properties of 1T/2H Phase MoS_2 for Gas Sensing Application

CHAPTER – 3

EFFECT OF VARYING THE PRECURSORS' CONCENTRATION ON STRUCTURAL AND ELECTRONIC PROPERTIES OF 1T/2H PHASE MoS_2 FOR GAS SENSING APPLICATION

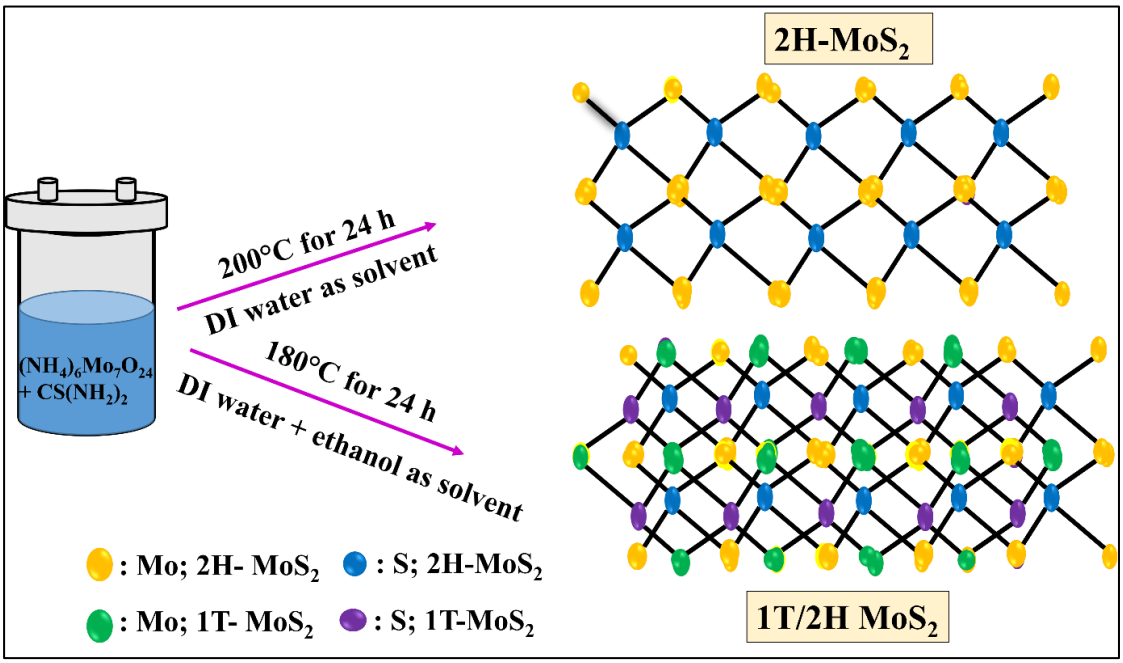

In this chapter, we have synthesized a mixed phase of MoS_2 using the hydrothermal method by varying the weight percentage of the precursors' concentration. The systematic effect of the increase in weight percentage of the ammonium ions (NH^{4+}) concentration on the structural and electronic properties of the synthesized 1T/2H MoS_2 nanostructures has been investigated. Raman, XRD confirmed the availability of the mixed phase of MoS_2, and the effect of variation in concentration is visible in the SEM images. The increase in weight percentage has increased in the 1T phase which causes a decrease in the optical band gap and has been confirmed using the UV-Visible Spectroscopy. Out of all the prepared 1T/2H MoS_2 nanostructures, the 1T/2H MoS_2 with 1.8 M concentration has exhibited the highest amount of 1T phase indicating the metallic behavior and the obtained bandgap is approximately 1.5 eV. The XPS spectra conclude that with the increase in NH^{4+} ion concentration, around 45.8 % metallic (1T) character has appeared in the 1T/2H-MoS_2 and a mixed morphology has been obtained

with the agglomeration of the tiny pin-like structures. Thus, the mixed phase of 1T/2H-MoS_2 is found to be a better candidate for gas sensing in terms of its improved bandgap, and available edge on the surface as active adsorption sites.

3.1 Introduction

Transition metal dichalcogenides (TMDs) comprising a general formula MX_2, where M stands for a transition metal, such as Mo, W, Ti, and X belongs to a chalcogen atom, such as S, Se, and Te, are prepared using various methods with extensive diversity in electrical properties varying from semiconductors, metals to superconductors [1,2,3]. MoS_2, from the family of TMDs, is an extensively researched material because of the availability of direct bandgap in monolayers and good electron mobility of 60 $cm^2V^{-1}s^{-1}$ at 250 K and high current on/off ratio [4]. Based on the atomic arrangement of Mo/S atoms, MoS_2 can be found in two phases. The most prevalent and stable form of MoS_2 in the environment is the 2H phase. Both 1T and 2H phases show the arrangement such as each Mo atom is surrounded by six S atoms. A distinct difference between 2H-MoS_2 and 1T-MoS_2 is that 2H-MoS_2 is semiconducting, whereas the latter is metallic [5]. Due to the metallic phase of 1T-MoS_2, metal dichalcogenides (TMDs) gained huge attention in MoS_2-derived applications. Commonly, 1T-MoS_2 is produced by chemically exfoliating 2H-MoS_2 and intercalating it with alkali ions like Li^+, Na^+, and K^+. The resulting 1T-MoS_2 materials tend to be hydrophilic [6]. The most common method of Li^+ intercalation involves the transfer of an electron from the reducing agent to MoS_2, which raises the electron density of Mo d-orbital. It leads to the 1T (metallic) phase transition by introducing instability in the 2H (semiconducting) phase. By improving the exposed active sites and the charge transfer characteristics of MoS_2 nanosheets, the catalytic activities of the 1T phase are enhanced [7]. As per reports, Li^+ intercalation of 2H-MoS_2 is one of the complicated methods to prepare 1T-MoS_2. Using the Na^+ ion intercalation, the best quality of nanosheets is obtained. By maintaining the growth kinetics, the hydrothermal process is the most used method to prepare 1T-MoS_2 nanosheets and their composites, specifically for electrocatalytic applications. For further improved electrocatalytic performance, reactions are optimized for 1T-MoS_2 nanosheets with morphologies in the form of tears, pinholes, and defects. 1T-MoS_2 finds promising uses in environmental monitoring, industrial and medical fields, etc. as

an efficient sensor. For excellent sensitivity, a large surface area and chemical and thermal stability of the material are required. The effective surface-to-volume ratio, excellent electrical properties, and highly reactive active sites make MoS_2 a promising gas-sensing material [8]. For gas sensing, 1T or the mixed phase of 1T/2H-MoS_2 is preferable to pure 2H-MoS_2 due to its metallic properties. In 2H MoS_2, the edge sites are excellent for adsorption and catalytic reactions whereas basal planes are catalytically inert. However, the basal planes of 1T MoS_2 are rich in active sites compared to 2H-MoS_2, which is more desirable for improving the gas sensing performance and the sensitivity largely relies on the adsorption strength of gas molecules over the sensor's surface i.e. more active sites, more adsorption. For that reason, the phase exploitation between the 2H and 1T structure of MoS_2 is more necessary for the enhancement of gas sensing properties [9].

In the present work, encouraged by the alkali ion intercalation, we propose a novel and easy strategy for the synthesis of 1T/2H mixed phase of MoS_2 using the hydrothermal method with the addition of ammonium molybdate heptahydrate and thiourea for activating the ammonium ion (NH^{4+}) intercalation. Presence of more active sites, controlled electrical conductivity, and good optical properties, the prepared 1T/2H MoS_2 is expected to exhibit better gas sensing performances.

3.2 Materials and Methods

3.2.1 Chemicals

Ammonium Molybdate Tetrahydrate (AMT) $(NH_4)_6Mo_7O_{24}.4H_2O$, Thiourea $CS(NH_2)_2$, De-ionized (DI) water, and Ethanol. All the chemicals are used as purchased without any further purification.

3.2.2 Synthesis Procedure

A simple hydrothermal method was employed to synthesize a mixed 1T/2H-MoS_2 using 60 ml of ethanol/ DI water mixture with a 1:2 ratio as solvent by adding AMT as Mo precursor and thiourea as S precursor with a 1:1 ratio by varying the molar concentration as 1, 1.4, and 1.8 M. To obtain a mixed solution, the used precursors were dissolved in 60 ml of DI/ethanol solvent and swirled at 600 rpm for 30 min. The entire solution was then

put into a Teflon-lined autoclave and heated for 24 hours at 180 °C. The resulting slurry was rinsed four times with DI water and ethanol, and the precipitates were then put in the oven to dry at 100°C for 12 h and marked as MoS_2-1, MoS_2-1.4 & MoS_2-1.8 corresponding to their concentrations. Figure 3.1 illustrates the simplified representation of the synthesis of 1T/2H-MoS_2 using the hydrothermal method.

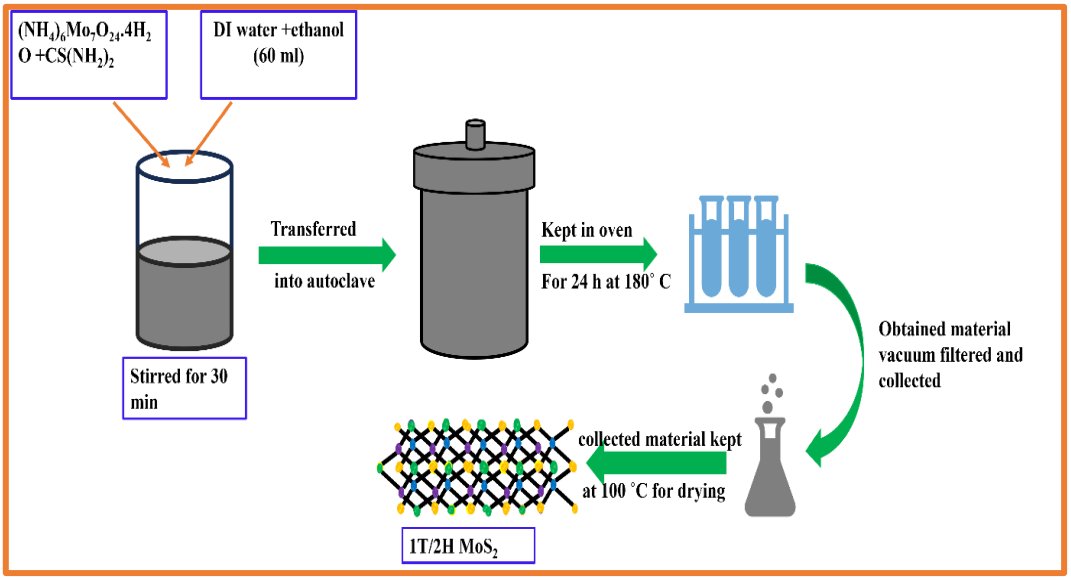

Fig. 3.1: Schematic representation of the hydrothermal synthesis of 1T/2H-MoS_2

3.3 Results and Discussion

3.3.1 Structural and Morphological Properties of Prepared 1T/2H-MoS_2 with Varying NH^{4+} Concentration

The morphologies of MoS_2-1, 1.4 & 1.8 nanostructures were analyzed. Figure 3.2 (a, b, & c) are SEM image representations clearly showing the nanoflowers morphology of MoS_2. From the SEM images, it has been observed that MoS_2-1 shows a structure of irregularly shaped bubbles with solid and thick surfaces (Fig. 3.2 (a)), which has been further converted into sharp and smaller micro flower bubbles with sharp pin-shaped structures (Fig. 3.2(b)) and with an increase in concentration from 1 M to 1.4 M and later the crumbled micro flowers seemed to be segregated into smaller sticks and agglomeration of the sticks was observed when concentration was raised from 1.4 M to 1.8 M (Fig. 3.2 (c)).

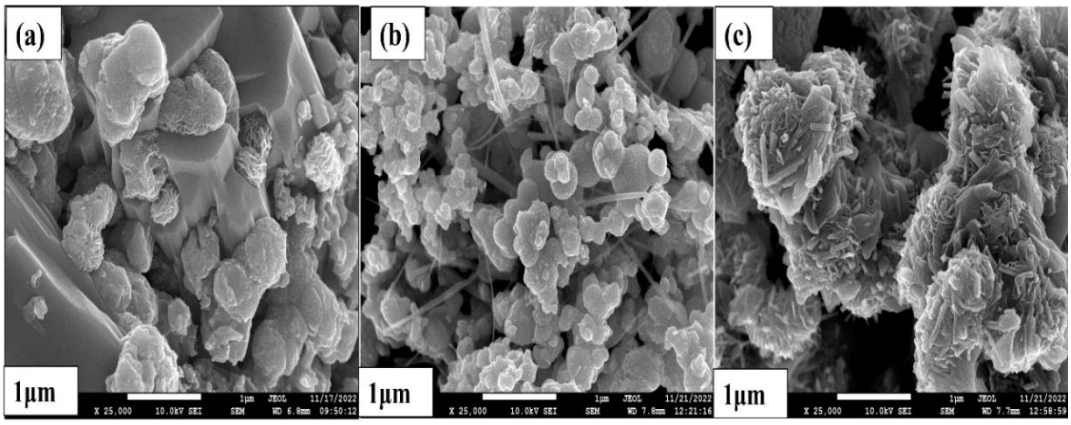

Fig. 3.2: SEM images of (a) MoS_2-1, (b) MoS_2-1.4, & (c) MoS_2-1.8

The XRD patterns of synthesized MoS_2 nanoflowers are shown in Fig. 3.3(a). MoS_2-1.8 exhibited three diffraction peaks at 13.8° (002), 32.6° (100), and 58.1° (110), whereas MoS_2-1.4 showed the diffraction peaks at 13.59° (002), 32.46° (100), and 57.64° (110), and MoS_2-1 registered the diffraction peaks at 14.03° (002), 33.12° (100), and 60.26° (110) as shown in Table 1. Some additional peaks around 11°, and 21° corresponding to (002) and (004) crystal planes appeared because of the partial intercalation of ammonium ions (NH^{4+}) increasing the interplanar spacing of MoS_2 and confirming the hybrid phase of 1T and 2H. Fig. 3.3(b) represents the Raman Spectra of the prepared MoS_2 nanoflowers with corresponding concentrations. As of the 2H-MoS_2, three peaks at 282.74 cm^{-1}, 376.29 cm^{-1}, and 404.03 cm^{-1} have been observed in MoS_2-1.8 corresponding to the E_{1g}, E^1_{2g}, and A_{1g} respectively, whereas for 1T, E_{1g} signifies the octahedral coordination of Mo, E^1_{2g} represents the in-plane vibrations of two S atoms w.r.t. the Mo atoms in opposite direction, and A_{1g} is the out-of-plane vibration of S atoms in opposite directions [10]. The emergence of the peaks at 126.5 cm^{-1}, 196.7 cm^{-1}, and 351.9 cm^{-1} corresponding to J_1, J_2, and J_3 respectively demonstrated the formation of 1T-MoS_2. J_1 modes correspond to the zigzag chain's in-plane shearing mode relative to the other, J_2 to the shifts of S atom layers with respect to the Mo atoms, and J_3 to the stretching towards the out-of-plane component of one side of the zigzag chain relative to the other [8]. Herein, MoS_2-1 does not exhibit the A_{1g} peak, whereas the intensity in MoS_2-1.4 is very low for the same, suggesting the dominance of basal planes in comparison to the edges in MoS_2-1.4 [11]. Interestingly, MoS_2-1, 1.4 & 1.8 seem to exhibit 1T and 2H characteristic peaks resulting the higher

J_1 and J_3 intensities in the case of MoS_2-1.8 as compared to the others, suggesting that MoS_2-1.8 contains a good fraction of 1T.

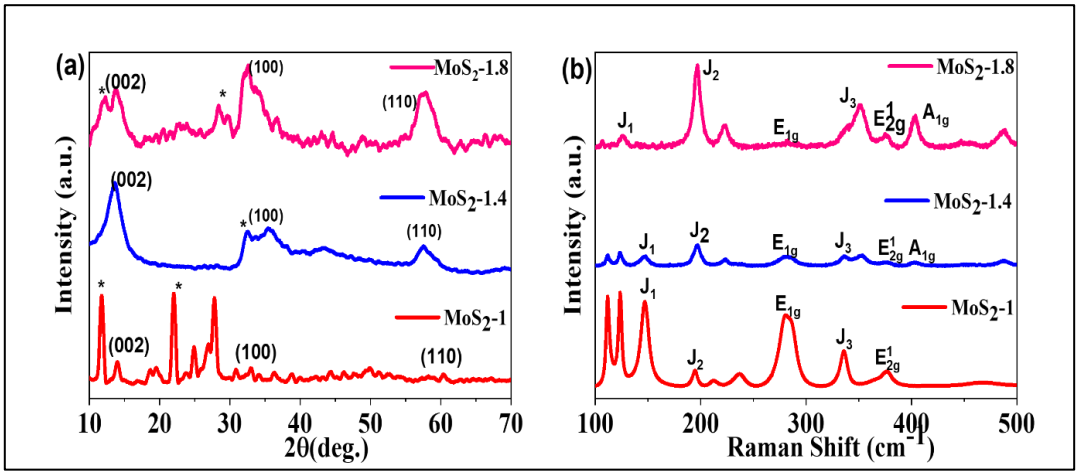

Fig. 3.3: (a) X-ray Diffractograms, & (b) Raman Spectra of MoS_2-1, MoS_2-1.4, & MoS_2-1.8

Table 3.1: Interplanar Spacing and crystallite size of the prepared MoS_2 samples with respect to the diffraction angle

Sample	(002) 2θ (°)	Interplanar Spacing (nm)	Crystallite size (nm)
MoS_2-1.8	13.8°	0.65	0.13
MoS_2-1.4	13.59°	0.64	0.14
MoS_2-1	14.03°	0.63	0.19

3.3.2 Optical and Core Level Studies of Prepared 1T/2H-MoS_2 with Varying NH^{4+} Concentration

To determine the effect of mixed-phase 1T and 2H-MoS_2 on the optical properties, UV-Vis measurements were performed and plotted in Fig. 3.4(a), the two peaks around 200-400 nm correspond to the strong optical absorption indicating a direct excitonic transition from the valence band to the conduction band. From Fig. 3.4(a), in the range 200-700 nm, weak light absorption has been noticed in MoS_2-1, which further decreased significantly after 350 nm. On the other hand, for MoS_2-1.4 & MoS_2-1.8, a significant increase in the light absorption was noticed as compared to the MoS_2-1 and their light absorption remained high above 400 nm. Enhanced absorption was noticed in 1T/2H-MoS_2 nanostructures for 1.8M and 1.4M. The light absorption of 1T/2H-MoS_2 in the visible region has appeared

almost twice that of the 2H phase dominant MoS_2 [12]. This has improved due to the increase in metallic (1T) character in 1T/2H MoS_2. Further, the bandgap of 1T/2H-MoS_2 has been calculated with all the performed concentrations using the tauc-plots, and representations has been shown in Fig. 3.4(b-d) [8].

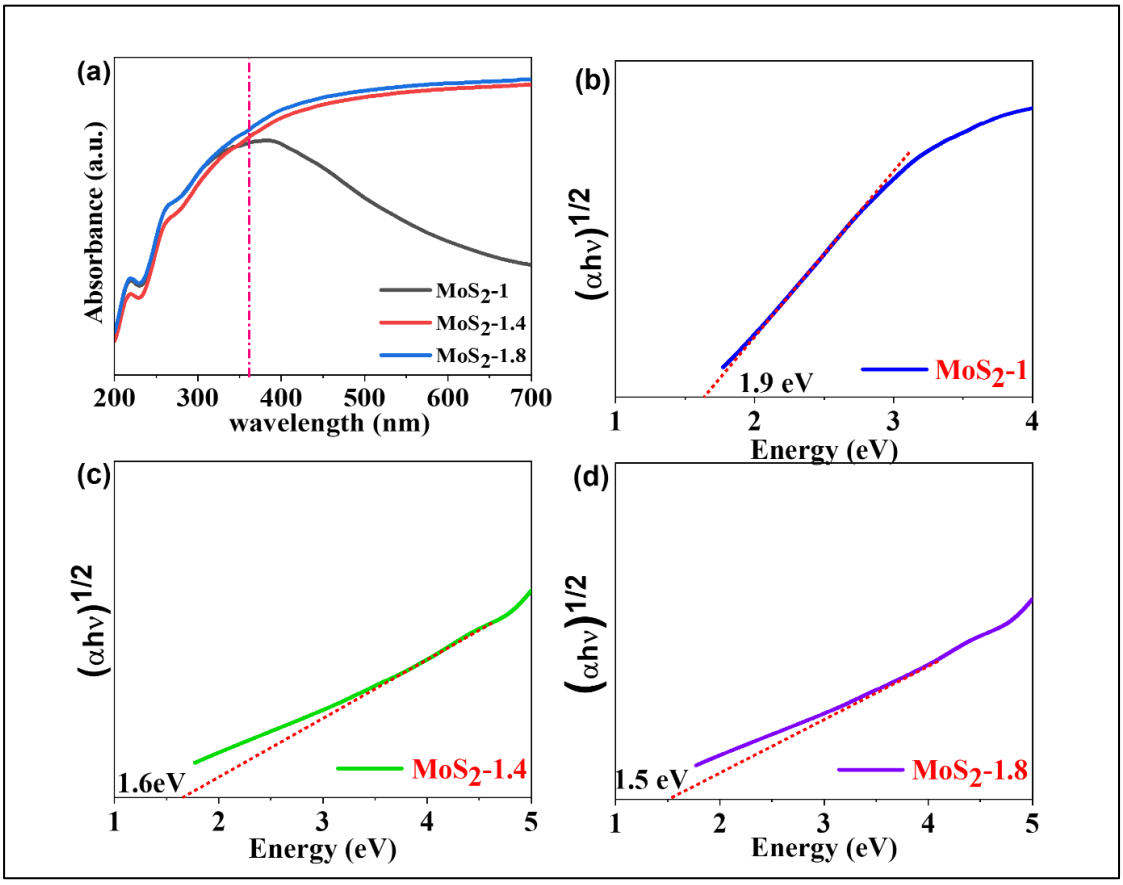

Fig. 3.4: (a) UV-Vis Spectra and Tauc plots of (b) MoS_2-1, (b) MoS_2-1.4, & (c) MoS_2-1.8

To determine the percentage of the 1T and 2H phases existing in the mixed 1T/2H-MoS_2, XPS analysis is important. The Mo 3d peaks were located at 228.8 eV and 231.4 eV which relate to the $Mo3d_{5/2}$ and $Mo3d_{3/2}$ respectively. The S 2p peaks were located between 161-163 eV which determines the S 2p state. The individual contributions of 1T & 2H in terms of percentage in the mixed form of MoS_2 with varied concentrations have been determined (Fig. 3.5(a-f)). The peaks in MoS_2-1 (Fig. 3.5(a)) are associated with the 1T phase of MoS_2, whereas the peaks in MoS_2-1 at 228.8 eV and 232.1 eV are related to the 2H phase of MoS_2 [13]. The amount of the 1T and 2H nature present in mixed-phase MoS_2 is calculated from the deconvoluted peaks, determined by the area

percentage occupied by the Mo peaks. According to the experimental results, the 1T character in MoS_2 developed to 27.9% (1 M), 36.3% (1.4 M), and 45.8% (1.8 M) when the precursor concentration ratio increased from 1 to 1.8 M, and subsequently the 2H ratio decreased. In addition, with the increase in concentrations, the intensity as well as the area percentage of the peak related to Mo^{6+} available around 236.2 eV also increased indicating the incomplete sulfurization of Mo precursor (Fig. 3.5 (e)).

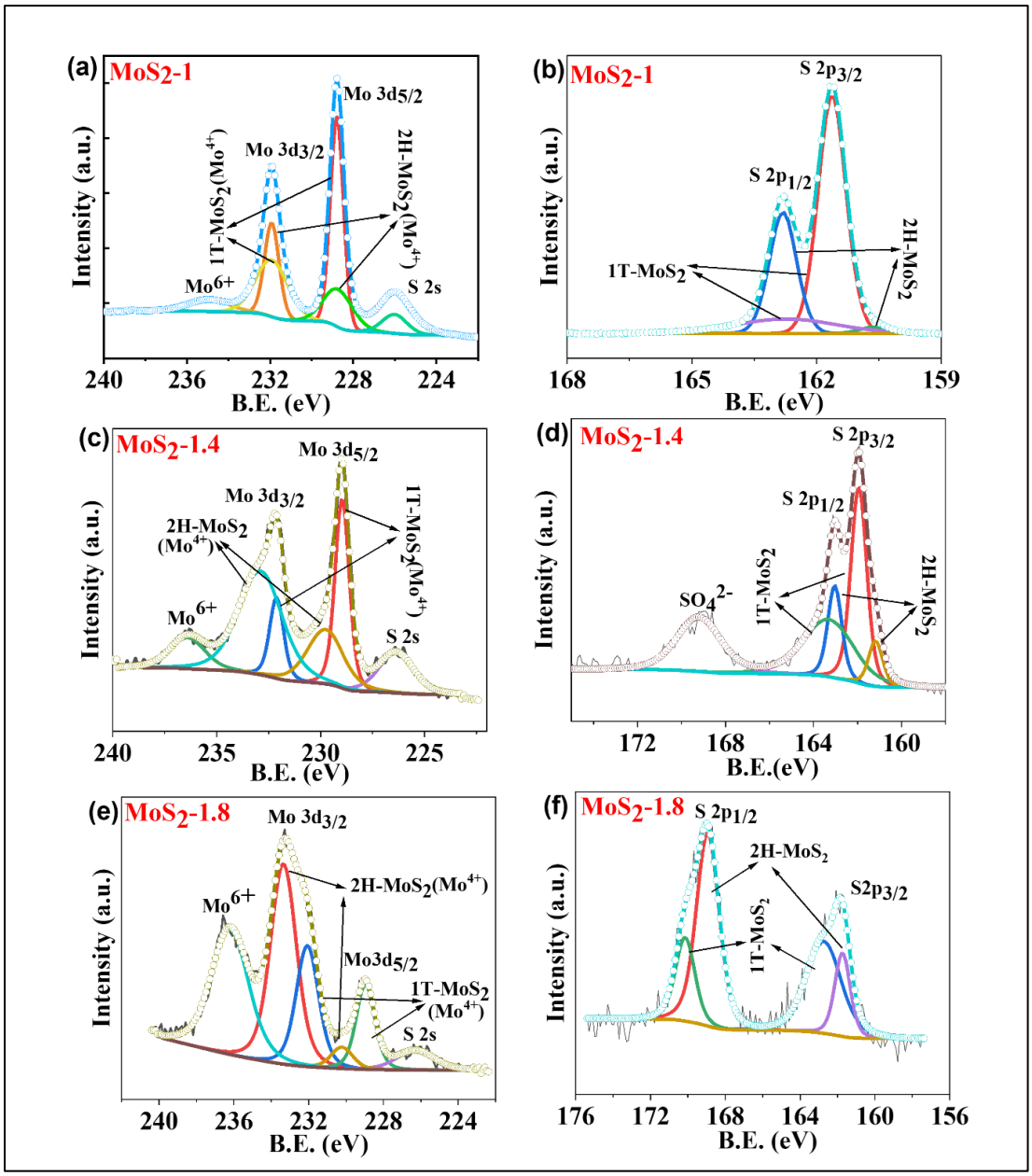

Fig. 3.5: (a, c, e) XPS spectra of deconvoluted Mo 3d and (b, d, f) S 2p core levels differentiating 1T and 2H characters of MoS_2 for MoS_2-1, MoS_2-1.4, & MoS_2-1.8

3.4 Conclusion

1T/2H-MoS_2 nanoflowers have been successfully prepared through the hydrothermal method at 200 °C with the Mo/S molar ratios 1, 1.4, and 1.8. MoS_2. The obtained MoS_2 indicates that the intercalation transpired with the increased concentration of NH^{4+} ions. The interplanar spacing between MoS_2 layers increases with an increase in concentration with the decrease in crystallite size and the crystallite size lies in the range of 0.13-0.19 nm. Intercalation induces the formation of 1T character of MoS_2 which has been validated by Raman, XPS, and UV-Vis spectroscopy. The presence of corresponding Raman modes (J_1, J_2, and J_3) has confirmed the existence of a mixed 1T/2H phase of MoS_2. Further, the content percentage (1T/2H) has been obtained using Mo 3d deconvoluted XPS spectra. Therefore, it is deduced that the mixed 1T/2H MoS_2 samples have been successfully prepared using the hydrothermal method, and the mixture of DI water with ethanol encouraged the synthesis of mixed 1T/2H-MoS_2 in hydrothermal conditions which are stable. The microflower morphology has appeared to be turned into a pin-like structure by increasing the surface-to-volume ratio of individual grains along with more available active sites suggesting that NH^{4+} intercalated 1T/2H-MoS_2 could be suitable for gas sensing.

References

1. Manzeli, S., Ovchinnikov, D., Pasquier, D. *et al.*, "2D transition metal dichalcogenides" *Nature Reviews Materials* 2, 17033 (2017), https://doi.org/10.1038/natrevmats.2017.33

2. Samy, O.; Zeng, S.; Birowosuto, M.D.; El Moutaouakil, A., "A Review on MoS_2 Properties, Synthesis, Sensing Applications and Challenges" *Crystals* 2021, *11*, 355. https://doi.org/10.3390/cryst11040355

3. Zhong Lin *et al.,* "2D materials advances: from large scale synthesis and controlled heterostructures to improved characterization techniques, defects and applications*". 2D Materials*, 2016, 3 (042001), **DOI**: 10.1088/2053-1583/3/4/042001

4. Zong, Boyang and Li, Qiuju and Chen, Xiaoyan and Liu, Chengbin and Li, Liangchun and Ruan, Jian and Mao, Shun, "Highly Enhanced Gas Sensing Performance Using a 1T/2H Heterophase MoS_2 Field-Effect Transistor at Room Temperature", ACS Appl. Mater. Interfaces 2020, 12, 45, 50610–50618, https://doi.org/10.1021/acsami.0c15162

5. Wonbong Choi, Nitin Choudhary, Gang Hee Han, Juhong Park, Deji Akinwande, Young Hee Lee, "Recent development of two-dimensional transition metal dichalcogenides and their applications", *Materials Today*, Volume 20, Issue 3,2017, Pages 116-130, https://doi.org/10.1016/j.mattod.2016.10.002

6. Zuoli He, W. or W.X. Que, "Molybdenum disulfide nanomaterials: Structures, properties, synthesis and recent progress on hydrogen evolution reaction", June 2016, *Applied Materials Today* 3:23-56, 10.1016/j.apmt.2016.02.001

7. Xin Zhang et al., "Phonon and Raman scattering of two-dimensional transition metal dichalcogenides from monolayer, multilayer to bulk material**",** ***Chem. Soc. Rev.*****,** 2015,**44,** 2757-2785, https://doi.org/10.1039/C4CS00282B

8. Levna Chacko *et al*, "Phase Engineering from 2H to 1T-MoS_2 for Efficient Ammonia PL Sensor and Electrocatalyst for Hydrogen Evolution Reaction", *J. Electrochem. Soc.*, 2019, 166 H263, **doi:** 10.1149/2.0071908jes

9. Hongmei Wang et al, "Synthesis, properties, and optoelectronic applications of two-dimensional MoS_2 and MoS_2-based heterostructures", ***Chem. Soc. Rev.***, 2018,**47**, 6101-6127, doi: https://doi.org/10.1039/C8CS00314A

10. Lei Huang et al., "Methyl-functionalized MoS_2 nanosheets with reduced lattice breathing for enhanced pseudocapacitive sodium storage", ***Phys. Chem. Chem. Phys.***, 2017,**19**, 13696-13702

11. Fareza, A.R., Nugroho, F.A.A., Fauzia, V., "Facile Synthesis of 1T-MoS_2 Nanoflowers Using Hydrothermal Method", 2021. Material Science Forum, Vol 1028, 173-178. https://doi.org/10.4028/www.scientific.net/msf.1028.173

12. Lie Tian, Rong Wu, Hai Yang Liu, "Synthesis of Au-nanoparticle-loaded 1T@2H-MoS_2 nanosheets with high photocatalytic performance", July 2019, *Journal of Materials Science* 54(13), DOI: 10.1007/s10853-019-03545-1

13. Taufik A, Asakura Y, Kato H, Kakihana M, Saleh R, Sekino T & Yin S, 1T/2H-MoS_2 engineered by in-situ ethylene glycol intercalation for improved toluene sensing response at room temperature, *Advanced Powder Technology,* 31(5) (2020)1868. https://doi.org/10.1016/j.apt.2020.02.022

Chapter – 4

Investigation of NO_2 Gas Sensing Response of MoS_2 Based Gas Sensors with SnO_2/MoS_2 and $CB/SnO_2/MoS_2$ Heterostructures in Ambient Conditions

CHAPTER – 4

INVESTIGATION OF NO_2 GAS SENSING RESPONSE OF MoS_2 BASED GAS SENSORS WITH SnO_2/MoS_2 AND $CB/SnO_2/MoS_2$ HETEROSTRUCTURES IN AMBIENT CONDITIONS

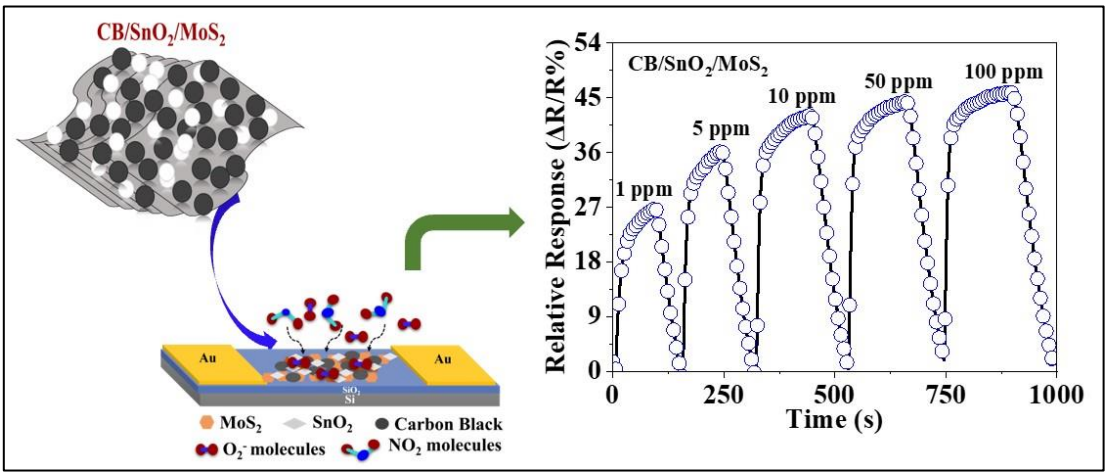

In this chapter, an active carbon black incorporated ternary nanocomposite $CB/SnO_2/MoS_2$ has been synthesized using the hydrothermal method to determine the nitrogen oxide (NO_2) gas sensing performance. The ternary heterostructure interface of $CB/SnO_2/MoS_2$ increases the effective adsorption sites over the surface for the adsorption of NO_2 gas molecules, enhancing surface reactivity toward gas molecules. The developed sensor exhibits a higher sensitivity and selectivity toward NO_2. Herein, the ternary heterostructure interface sensor showed a maximum sensing response ($\Delta R/R\% \sim 46\%$) for 100 parts per million (ppm) exposure, which is higher than bare MoS_2 and binary heterojunction of SnO_2/MoS_2. The gas-sensing mechanism is dedicated to the p-n heterojunctions and the Schottky barriers between interfaces, which have been justified by the electrical measurements. This work revealed active CB as an effective material for enhanced gas adsorption active sites and generated heterojunction interfaces between SnO_2/MoS_2, resulting in enhanced gas-sensing performance of the sensors.

4.1 Introduction

Rapid industrial development and economic and population expansion have dramatically upsurged the supply and need of commodities in society [1]. This

expansion has caused many toxic emissions such as combustible and toxic gases such as Nitride Oxide (NO), Nitrogen Oxide (NO_2), Ammonia (NH_3), volatile organic compounds (VOCs), Formaldehyde and so on which are harmful to the environment, the human health and the world ecosystem [2]. NO_2 is the most common exhaust gas from the waste emissions produced by industrial applications and automobiles. NO_2 is acidic and oxidizing in nature, highly reactive with a stinky smell, and causes serious harm to human health, particularly to the respiratory system causing permanent damage, even at low concentrations as 1 ppm (parts per million) [3]. Therefore, for the efficient detection of NO_2, the synthesis of nanomaterials and utilization to develop gas sensors are highly required to rapidly push gas sensing technology forward [4]. Metal oxide-based sensors are evolving among various available gas sensors due to their economic and simple operation, and ultrasensitive nature [5]. The main disadvantage of these sensors is their high working temperature [6]. Simultaneously, continuous efforts have been directed toward improving the recovery/response speed, stability, and selectivity, but efforts are particularly made in the direction of lowering the working temperature of these sensors [7]. Among metal oxide-based sensors, such as SnO_2 exhibited higher stability and became the most popular but their high operating temperature (100-400 °C), reduced sensor lifetime, and inferior selectivity behavior have inhibited their employment for large-scale applications due to the risk of ignition [8,9]. Generally, a lower operating temperature assures a reduction in power consumption and expands the application range of gas-sensing devices [10]. Recently, two-dimensional (2D) layered transition metal dichalcogenides (TMDCs) especially MoS_2 have gained huge recognition because of their layer-dependent properties comprising van der Waals and covalent bonding at the inter- and intralayer respectively with substantial mobility (700 cm^2/V-s) and semiconducting nature, proved it to be promising gas sensing material [11,12]. 2D TMDCs may also face the same selectivity issues as metal oxides by responding to more than one type of gas. In addition, response time is sluggish, and recovery is often incomplete [13]. With the increase in demand for highly sensitive, fast, and stable sensors, MoS_2-based composites have grown much interest in sensing applications [14, 15]. Recently, many studies concentrating on TMDCs (such as MoS_2) and metal oxide (SnO_2) hybrids have been reported with

increased sensing performance [16]. *Han et al.* have reported that the SnO_2/MoS_2 composite offers a relative response in 18.7 s at 5ppm NO_2 near room temperature [17].

Alternatively, carbon-based nanomaterials (CNMs) such as graphene, graphene oxide (GO), reduced graphene oxide (rGO) carbon nanotubes (CNTs), and carbon black (CB) have unique chemical and electronic transport properties, make most popular gas-sensing at low operating temperatures, unlike pristine metal oxide semiconductors and TMDCs. GO, rGO, and CNTs have emerged as potential functionalization candidates with MoS_2 and SnO_2 [18,19,20]. Out of these carbon materials, CB is not much reported for gas-sensing applications [21]. The CB is typically curved graphitic layers parallel to their spherical surface, which are prone to oxidization and form oxygen-containing functional groups for gas-sensing applications [22]. It has been reported that CB could be blended with materials such as conducting polymers and polyaniline (PANI) to access large active sites and enhance the electrical conductance to detect the NO2 molecules [23], [24]. Liou and Lin [25] studied the TiO_2-CB composite and revealed that the sensitivity of the TiO_2-CB composite can be enhanced by increasing the amount of TiO_2 to CB ratio (16:1) and the efficient recovery is attained at a high working temperature (150 ˚C) for the NO_2 gas (1–100 ppm). In another work, the composite of CB with α-type nickel hydroxide [α-$Ni(OH)_2$] nanosheets show the most rapid NO_2 gas detection, i.e., 2 s for the 100 ppm of NO_2 detection and the selectivity of Ni-CB is exceptional [26]. CB endows higher conductivity to the sensing films and besides that, CB can operate near room temperature making it suitable for this study [27], [28]. CB is considered a promising material for gas sensing due to its high specific surface area, excellent electrical properties, and chemical stability [29], [30]. In this work, different sensors based on bare MoS_2 nanosheets, binary SnO_2/MoS_2, and further an addition of active CB have been used to make a ternary composite with SnO_2 and MoS_2. The ternary heterostructure of $CB/SnO_2/MoS_2$-based sensors enhances the NO_2 sensing performance because of the higher abundant active sites on the surface and charge transportation properties. SnO_2 is expected to play a vital role with CB by preventing the oxidation of CB to improve the sensitivity of the fabricated sensor. This sensing strategy to enhance the gas-sensing performance near room temperature received attention to develop a low-cost and easy fabrication approach for a new class of gas sensors.

4.2 Experimental Details

4.2.1 Synthesis of MoS_2 Nanosheets and SnO_2/MoS_2 Heterostructures

To prepare MoS_2 nanosheets, a simple hydrothermal route was employed in which 1.0 g of sodium molybdate tetrahydrate ($Na_2MoO_4 \cdot 4H_2O$) and 1.2 g of thioacetamide were dissolved in 50 mL of deionized (DI) water. The dissolved precursors were stirred with a continuous stirring at 600 rpm/min using a magnetic stirrer at room temperature to obtain a homogeneous mixture. After that, this homogeneous solution was transferred to a 100-mL stainless steel autoclave and placed inside the oven at 220 ˚C for 24 h. Then, the autoclave was set to cool down naturally. The sample was washed multiple times with DI water and ethanol by centrifugation to extract the impurities and collect the black precipitates from the obtained solution. After that, the MoS_2 black powder was collected by drying the precipitates at 80 ˚C for 12 h in the oven. Subsequently, to synthesize the SnO_2/MoS_2 composite, 3.5 g of $SnCl_4 \cdot 5H_2O$ was dissolved in 60 mL of DI water and kept for magnetic stirring for 30 min to form a homogeneous mixture. After that, sodium hydroxide (NaOH) pellets were mixed in the mixture to form a white-colored mixture having a pH of around 10. Then, 0.5 g of pre-synthesized MoS_2 was mixed in the solution and stirred for the next 30 min, and the same procedure as above was repeated to obtain SnO_2/MoS_2 heterostructures.

4.2.2 Synthesis Procedure of $CB/SnO_2/MoS_2$

The 0.86 g of SnO_2/MoS_2 was dissolved in 50 mL of DI water with 30 mg of active CB and kept for ultrasonication for 1 h to obtain a homogeneous mixture. Then, the prepared solution was transferred to a 100-mL Teflon-lined stainless-steel autoclave and kept in the oven at 200 ˚C for 6 h. The collected sample was washed several times with DI water and ethanol to remove the impurities, and black precipitates were obtained from the resultant solution. The collected black powder was dried at 80 ˚C in the oven for 12 h. Figure 4.1 shows the step-wise synthesis of the MoS_2, binary composite SnO_2/MoS_2, and ternary composite $CB/SnO_2/MoS_2$ using the hydrothermal method.

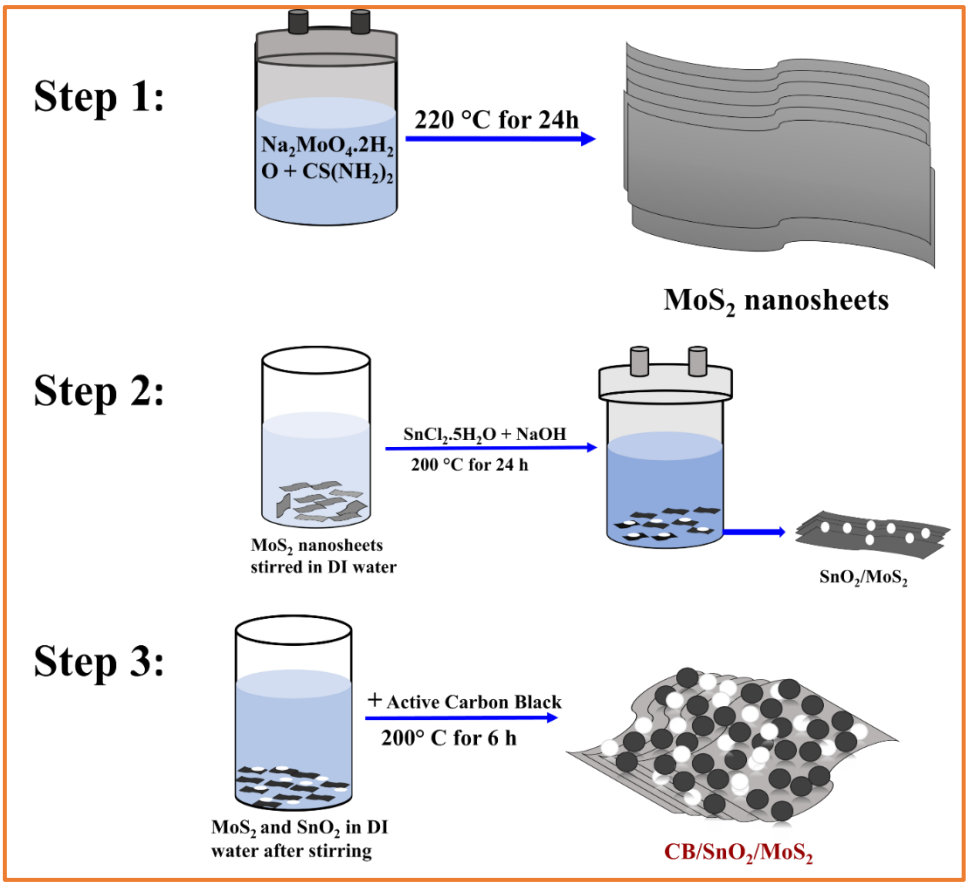

Fig. 4.1: Step-wise schematic representation of the hydrothermal synthesis of MoS_2 nanosheets, SnO_2/MoS_2, and Carbon black incorporated SnO_2/MoS_2 ($CB/SnO_2/MoS_2$)

4.2.3 Material Characterizations

X-ray powder diffraction (XRD) analysis was performed (Rigaku, New Delhi, India, Ultima-IV) to study the crystal structure and phase composition, and a Raman spectrometer with a laser source of wavelength 532 nm (inVia Renishaw Spectrometer) was used to study the vibrational modes of the materials. The morphological features of the microstructures were identified by using scanning electron microscopy (SEM), and the surface chemical composition of materials was characterized by X-ray photoelectron spectroscopy (XPS) with Al K_α source (λ = 1487 eV).

4.2.4 Gas Sensing Device Fabrication

To develop the resistance-based sensors, interdigitated gold (Au) electrodes (200 nm) were deposited by a thermal evaporation system on SiO_2/Si substrates with a shadow

mask. The separation between the two fingers of the electrode was 100 µm. The nanocomposites of MoS_2, SnO_2/MoS_2, and $CB/SnO_2/MoS_2$ were homogenously mixed in DI water separately using ultrasonication for 1 h, and then, the prepared solutions were drop-cast (10 µL) between the fingers deposited on the SiO_2/Si substrate with a constant concentration of 10 mg/mL using a micropipette. Further, these devices were kept for drying in a furnace at 100 ˚C for 20 min in an N_2 dry environment and used for electrical and gas-sensing measurements. Figure 4.2 shows the schematic diagram of the device fabrication using the drop cast approach.

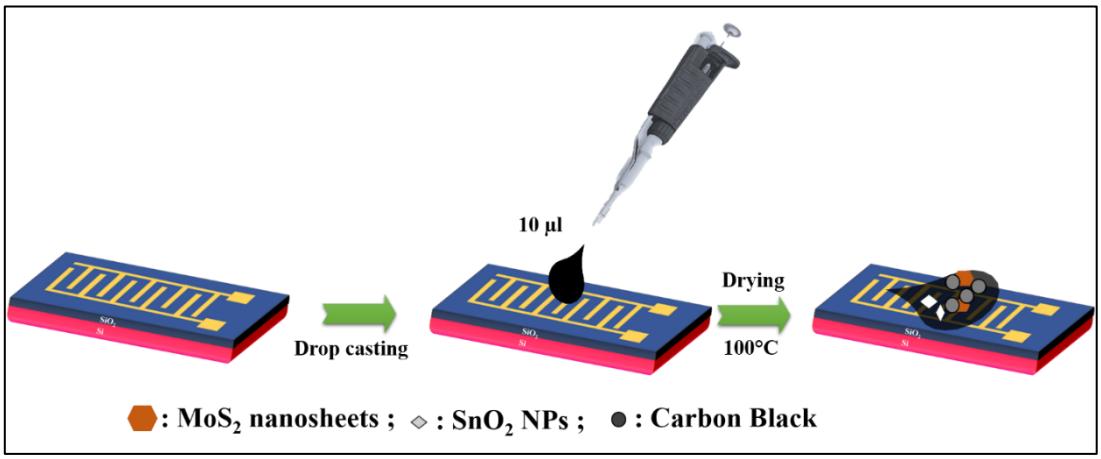

Fig. 4.2: Schematic diagram of the device fabrication for gas sensing measurements

4.3 Results and Discussion

4.3.1 Structural and Morphological Properties of MoS_2, SnO_2/MoS_2, and $CB/SnO_2/MoS_2$

To determine the crystallinity of the synthesized materials, X-ray diffraction patterns are observed [as shown in Fig. 4.3(a)]. For the bare MoS_2 sample, the diffraction peaks are observed at $2\theta = 14.2^\circ$, 33.6°, and 59.5°, corresponding to the (002), (100), and (110) planes related to the hexagonal phase of MoS_2 (JCPDS 37-1492). The diffraction peaks of SnO_2 corresponding to the pure tetragonal rutile phase show diffraction peaks at 26.7˚ (110), 34.1˚ (101), 51.8˚ (211), and 65.4˚ (301), which are in good consistency with the standard (JCPDS 41-1445) [31]. From the XRD pattern of $CB/SnO_2/MoS_2$, the characteristic peaks at 26.7˚ and 38.1˚ belong to the (002) and (100) diffraction planes of hexagonal graphite (JCPDS 41-1487), respectively. These peaks are used to identify the carbon crystal phase

[32]. The smaller peak intensities related to CB stipulate that the CB surface is covered by the rutile structure of SnO_2. In Fig. 4.3 (b), two main characteristic peaks at 375.41 and 401.3 cm^{-1} belong to E^1_{2g} and A_{1g} modes representing the in-plane and out-of-plane vibrations between Mo and S atoms, respectively. The two vibrational modes of A_{1g} at 584.3 cm^{-1} and B_{2g} at 634 cm^{-1} represent the vibrational bonds between Sn and O atoms, respectively. However, in $CB/SnO_2/MoS_2$, the appearance of D and G bands at 1359.63 and 1598.53 cm^{-1}, respectively, related to graphitic carbon confirming the bonding with MoS_2 and SnO_2 bands [14].

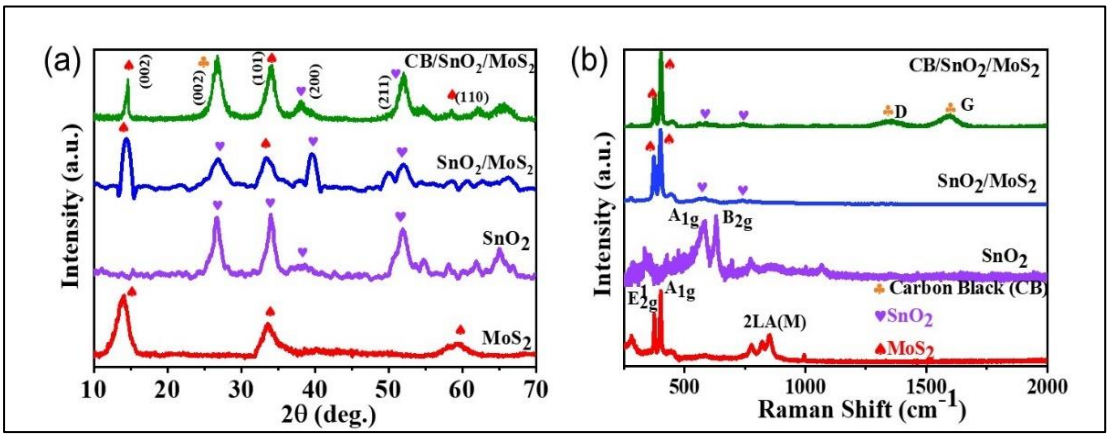

Fig. 4.3: (a) X-ray diffraction patterns and (b) Raman Spectra of hydrothermally synthesized SnO_2; MoS_2; SnO_2/MoS_2; and $CB/SnO_2/MoS_2$

From the SEM images, it is observed that the MoS_2 comprises the structure as sheets at 100 nm displayed in Fig. 4.4 (b), whereas SnO_2/MoS_2 heterostructures exhibit a distinct crumpled structure, unlike flat MoS_2 nanosheets. The SnO_2 clusters (white colored) are observed and widely distributed on the crumpled MoS_2 surface. Fig. 4.4 (c) depicts the SnO_2 microstructures decorated over self-assembled nanosheets of MoS_2 with multiple folds. Fig. 4.4(d) shows the SEM image of $CB/SnO_2/MoS_2$, where the densely distributed CB is also observed along with SnO_2 over the completely covered MoS_2 crumpled surface, which was hardly identified. It is observed that the CB particles and SnO_2 nanoparticles (NPs) are distinguishable and fully cover the surface of MoS_2 nanosheets [33].

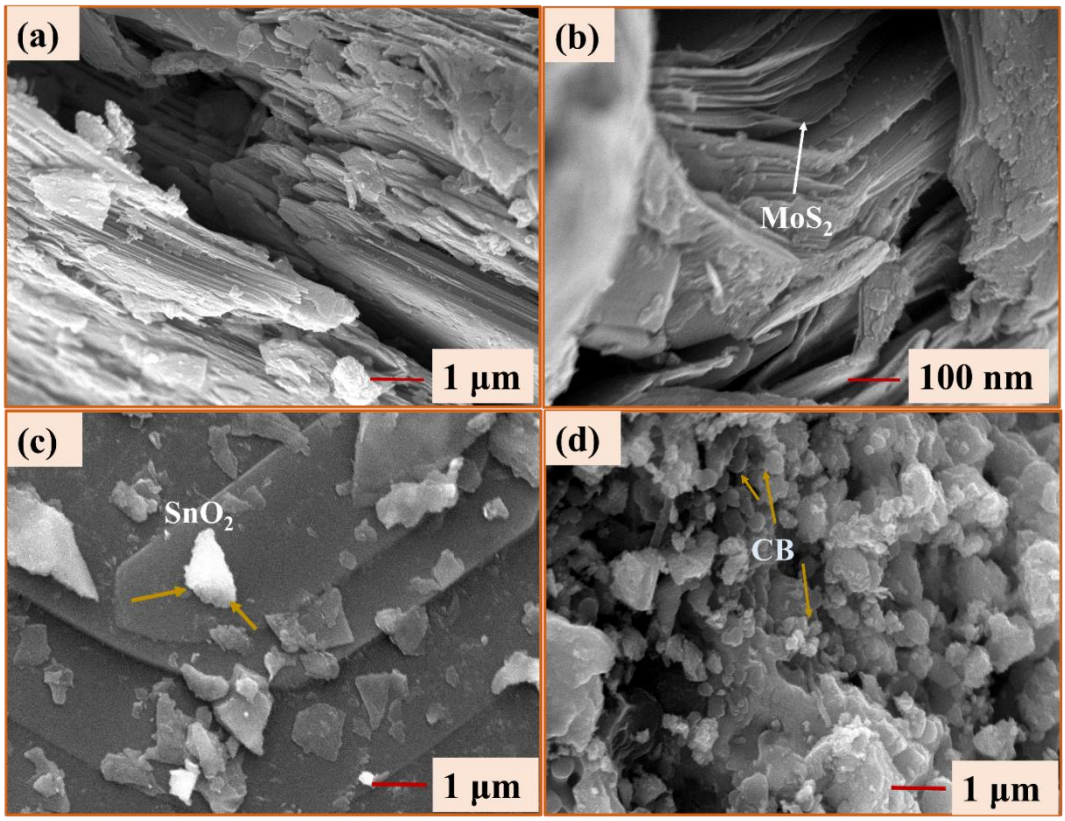

Fig. 4.4: SEM images of (a-b) hydrothermally synthesized MoS_2 nanosheets at 1 µm and 100 nm respectively; (c) SnO_2/MoS_2; SnO_2 has been marked; (d) $CB/SnO_2/MoS_2$; CB has been highlighted

4.3.2 Chemical Properties of $CB/SnO_2/MoS_2$

The XPS survey scan of the $CB/SnO_2/MoS_2$ composite is shown in Fig. 4.5(a), confirming the availability of the elements including C, Sn, O, Mo, and S from the CB, SnO_2, and MoS_2 materials, respectively. In Fig. 4.5(b), the high-resolution deconvoluted XPS spectrum of C 1s constitutes the four peaks at 284.6, 285.3, 286.7, and 289.7 eV corresponding to C = C (sp^2), C-O-C/C-OH, C-C (sp^3), and O = C-OH species, respectively. The main peak corresponding to C = C at 284.6 eV belongs to the pure graphite constituting CB mainly and the other additional peaks arise since the O-H bonds present during the preparation of heterostructures [34]. The two peaks from the Sn 3d region [Fig. 4.5(c)] located at 487.4 (Sn $3d_{5/2}$) and 495.8 eV (Sn $3d_{3/2}$) with a spacing of 8.4 eV show the presence of Sn element in the form of Sn^{4+} oxidation state in SnO_2/MoS_2 [35]. Additionally, the minor Sn 3d doublet having the peaks present at 488.5 and 496.6 eV corresponds to the Sn^{2+} oxidation state arising from the Sn-OH

surface group, originating due to the heterojunction [35]. Fig. 4.5(d) shows the deconvolution of O 1s spectra with the main peak situated at 531.3 eV verified as one of the main characteristic peaks of SnO_2 determining Sn-O bonding. Additionally, the peaks present at 532.2 and 533.8 eV can be attributed to the oxygen species originated due to O^{2-} adsorption sites and the hydroxyl ions, respectively [36].

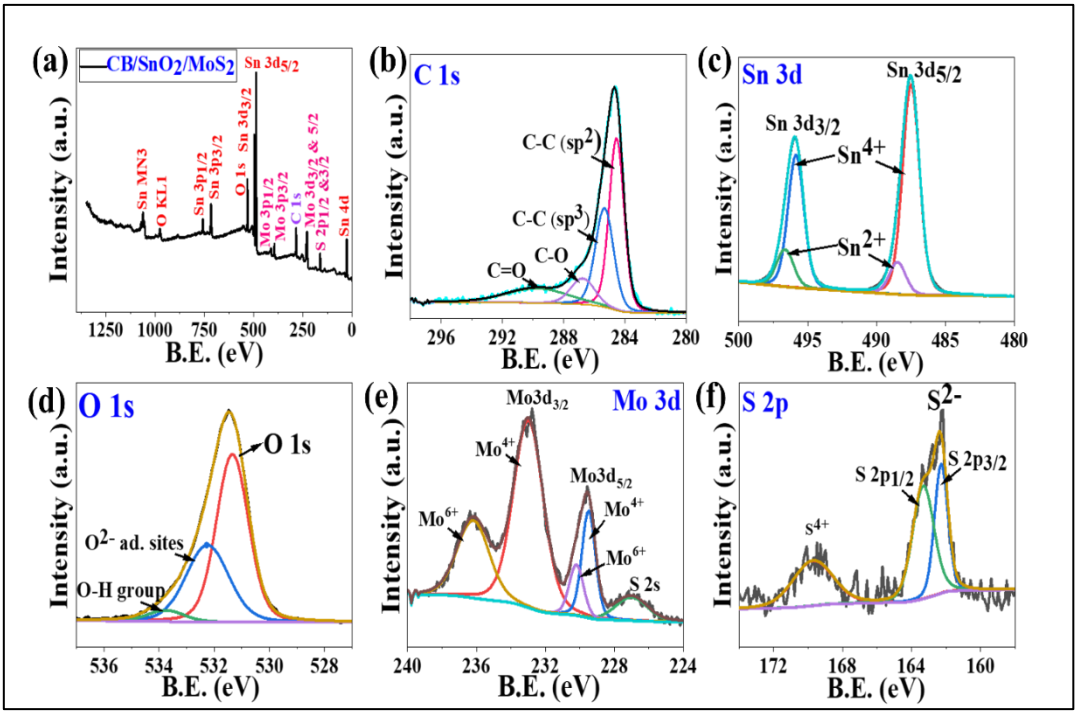

Fig. 4.5: (a) XPS survey spectra of CB/SnO_2/MoS_2; (b) deconvoluted core-level spectra of C 1s of CB; (c-d) Sn 3d & O 1s of SnO_2; and (e-f) Mo 3d & S 2p of MoS_2

In Fig. 4.5(e), the XPS spectrum of Mo 3d from the CB/SnO_2/MoS_2 shows the main peaks at 229.4 and 232.9 eV related to the Mo^{4+} $3d_{5/2}$ and $3d_{3/2}$, respectively. In addition to these two main peaks, the peaks available at 230.2 and 236.2 eV are assigned to Mo^{6+} $3d_{5/2}$ and $3d_{3/2}$, respectively, which might be the result of the partial oxidation of MoS_2 in the presence of SnO_2 to form MoS_3, which further turns into MoO_3. The deconvolution of S 2p spectra consisting of two main peaks situated at 162.3 and 163.3 eV has been assigned to S^{2-} $2p_{3/2}$ and S^{2-} $2p_{1/2}$ of MoS_2, respectively, and an extra peak at 169.6 eV related to the S^{4+} state confirming the presence of Mo^{6+} state [Fig. 4.5(f)] [37]. Interestingly, the XPS results of CB, SnO_2, and MoS_2 from the heterostructures show the strong interaction between one another and imply the intimate growth of CB over the SnO_2/MoS_2 surface.

4.3.3 Electrical and Gas Sensing Measurements of MoS_2, SnO_2, and $CB/SnO_2/MoS_2$

To determine the reliability and behavior of synthesized materials such as MoS_2, SnO_2/MoS_2, and $CB/SnO_2/MoS_2$ as sensing material, electrical measurements were recorded for the prefabricated devices made with Au electrodes, and data are displayed in Fig. 4.6 (a). The I–V characteristics of the fabricated sensors exhibit nonlinear behavior (Schottky nature). This Schottky contact behavior between the heterojunctions is believed to be created in SnO_2-incorporated MoS_2 nanosheets (SnO_2/MoS_2) and $CB/SnO_2/MoS_2$ because of the defects present on the surface created during functionalization and also due to the difference in the work functions between MoS_2 nanosheets ($\phi = 4.53$ eV), SnO_2 ($\phi = 4.85$ eV), and CB ($\phi = 4.5$ eV) [38], [39], [40]. The current-level difference between MoS_2 and SnO_2/MoS_2 is noticeable, and it is possible due to the large bandgap and lower conductivity of SnO_2 as compared to MoS_2.

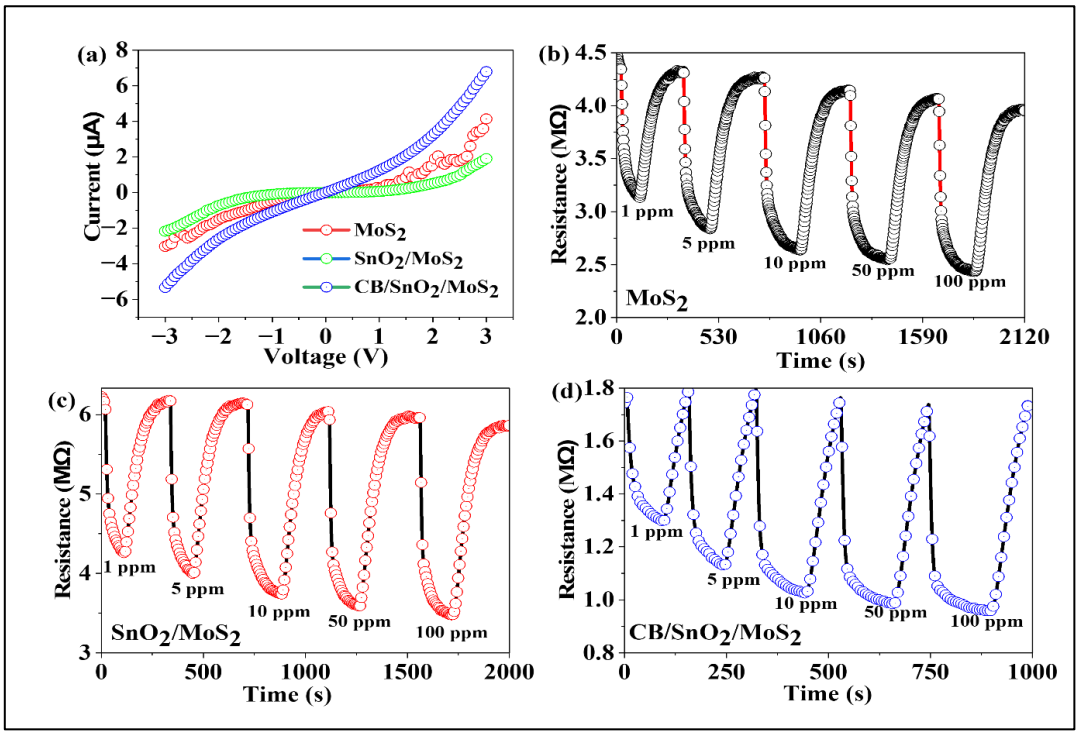

Fig. 4.6: (a) I-V curves and dynamic resistance curves of NO_2 gas sensing of (b) MoS_2 sensor (c) SnO_2/MoS_2 sensor; (d) $CB/SnO_2/MoS_2$ sensor at 30 ℃

However, the enhancement in current and conductivity in $CB/SnO_2/MoS_2$ is developed, which probably be due to additional CB conductance channels with SnO_2 NPs and MoS_2 nanosheets. Fig. 4.6 (a) shows that the incorporation of CB with the SnO_2/MoS_2 matrix modulates the electrical properties of $CB/SnO_2/MoS_2$. The slope of the I–V curve of SnO_2 is minimum and maximum for $CB/SnO_2/MoS_2$, which is the reciprocal of resistance. The same behavior was observed with the initial resistances of the fabricated sensors in air [Fig. 4.6(b)–(d)]. Further, during the NO_2 gas-sensing measurement, the resistance of the MoS_2 sensor decreased during NO_2 exposure (oxidizing gas), suggesting that the MoS_2 behaves as a p-type semiconductor.

The transient relative response curves of bare MoS_2, SnO_2/MoS_2, and $CB/SnO_2/MoS_2$ sensors for 1–100-ppm NO_2 are shown in Fig. 4.7(a)–(c). The comparative relative response curves of corresponding transient graphs MoS_2, SnO_2/MoS_2, and $CB/SnO_2/MoS_2$ sensors are shown in Fig. 4.7(d).

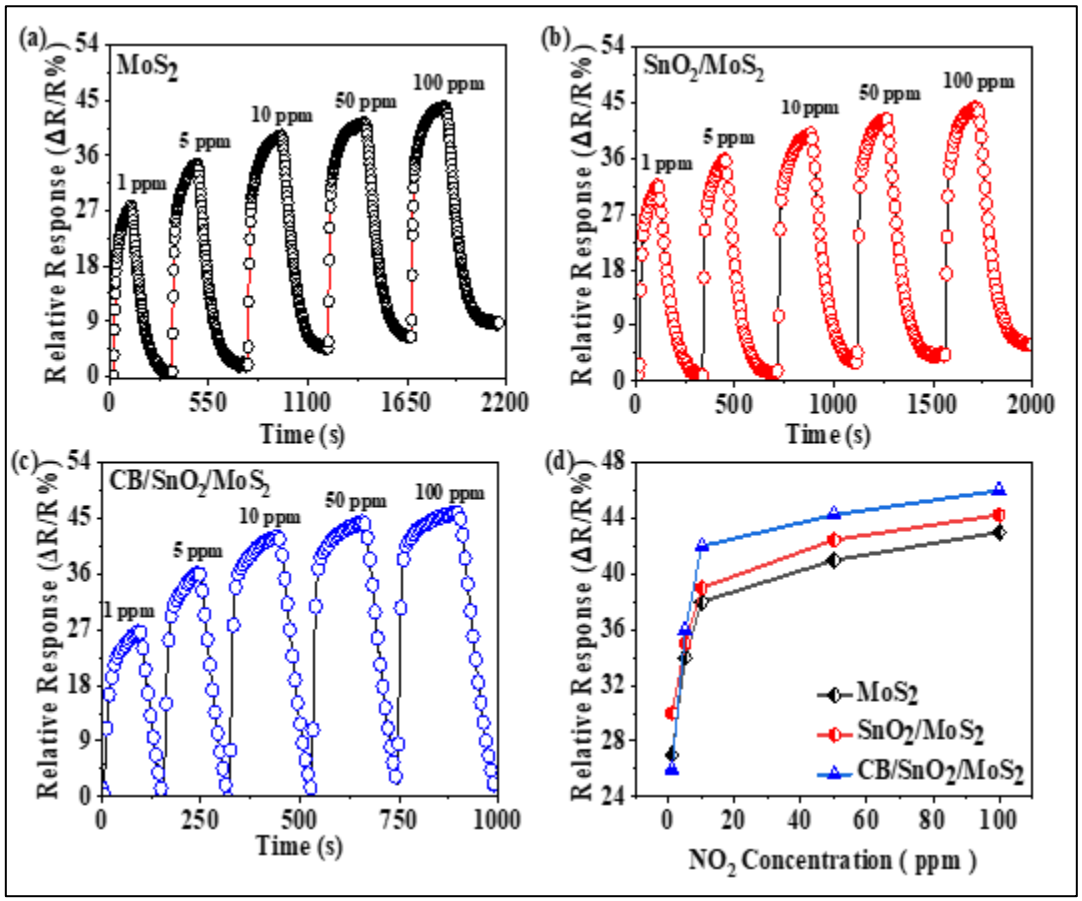

Fig. 4.7: (a-c) Transient relative response of MoS_2, SnO_2/MoS_2, and $CB/SnO_2/MoS_2$ for NO_2 gas at 30 ˚C; (d) comparative relative response for NO_2 gas

4.3.4 Gas Sensing Test Measurements

The sensing performances of the prepared nanocomposites were evaluated through electrical resistance change upon exposure to NO_2 gas at 30 ˚C. As the concentration of NO_2 gas increases, a larger change in resistance is recorded, as shown in Fig. 4.6 (b)–(d). Fig. 4.8(a) shows the selectivity of various sensors, which are tested at a 100 ppm of NO_2 gas concentration for different gases such as NO_2, NH_3, H_2, H_2S, and CO. All fabricated sensors show highly selective behavior toward NO_2 than other gases. Fig.4.8 (b)–(d) depicts the response and recovery curves of MoS_2, SnO_2/MoS_2, and $CB/SnO_2/MoS_2$ at 50 ppm NO_2, and response time (τ_{res}) of $CB/SnO_2/MoS_2$ is much shorter, i.e., 26 s than that of bare MoS_2 (61 s) and nanocomposite SnO_2/MoS_2 (52 s). Moreover, the recovery time of $CB/SnO_2/MoS_2$ (73 s) is much shorter in comparison to bare MoS_2 (183 s) and SnO_2/MoS_2 (198 s) at 30 ˚C temperature for NO_2 gas.

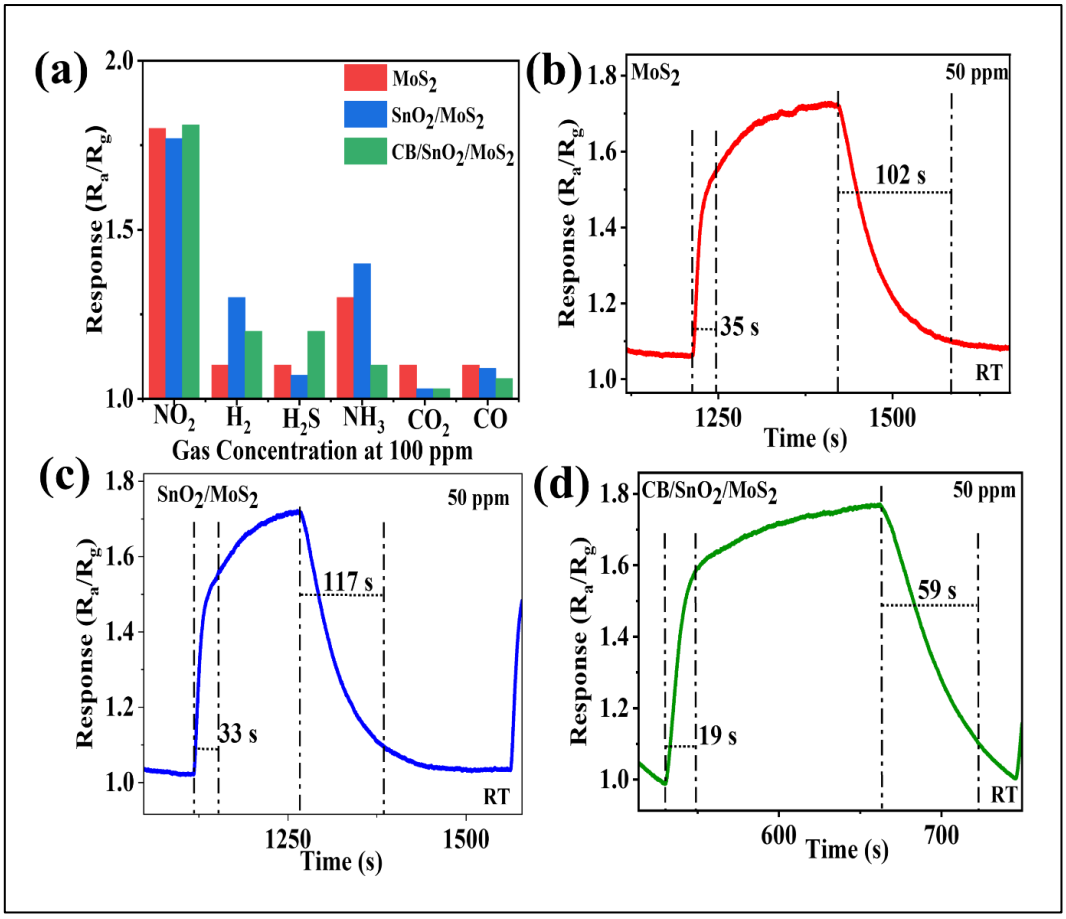

Fig. 4.8: (a) Selectivity response of the nanocomposites-based devices at 100 ppm gas concentration; Response and recovery times of (b) MoS_2; (c) SnO_2/MoS_2; (d) $CB/SnO_2/MoS_2$ based sensors for 50 ppm NO_2

The ternary $CB/SnO_2/MoS_2$ sensor shows better response than bare MoS_2 and binary SnO_2/MoS_2 sensors. Thus, $CB/SnO_2/MoS_2$ displays excellent sensing performance of 46% to 100 ppm NO_2 with a fast response of 26 s with complete recovery near room temperature (30 ˚C). All the above characteristics of $CB/SnO_2/MoS_2$ are competitive with the related reported gas sensors in Table 4.1.

Table 4.1: Comparison of gas sensing properties for MoS_2 nanocomposites toward NO_2 molecules

Sensing Materials	NO_2 (ppm)	Operating temp. (˚C)	ΔR/R (%)	Recover ability	Ref
MoS_2 nanosheets	50	RT	26	-	[41]
MoS_2/SnO_2	5	RT	18.7	Complete	[17]
SnO_2 NC/MoS_2 NSs	10	RT	28	Complete	[42]
MoS_2/Graphene aerogel	0.5	200	9	Complete	[43]
$CB/SnO_2/MoS_2$	100	RT (30˚C)	46	Complete	This work

4.4 Gas Sensing Mechanism

The uncertainty in the mechanism of NO_2 gas sensing with MoS_2 has always been a subject of discussion. Here, MoS_2 as a host material behaves as a sensing layer where the interaction of the gas molecules is detected. NO_2 being an electron acceptor gas takes the electrons from MoS_2 ($NO_2 + e^- \rightarrow NO^-_2$), and an electrical resistance change is observed [44]. As NO_2 gas is exposed to the MoS_2 nanosheets, the electrons are trapped on the surface due to oxidizing gas, and a large number of holes are created when reacted with oxygen species, which causes a decrease in sensor resistance [45]. The defects available on the surface of the sensing material behave as the active sites for NO_2 molecules, and the sensing reaction equations are given as follows [46]:

$$NO_2 + e^- \rightarrow NO^-_2 \quad (1)$$

$$NO_2 + O^-_2 + 2e^- \rightarrow NO^-_2 + 2O^- \quad (2)$$

$$NO^-_2 + V^{++s} \rightarrow NO_2 + h^+ \quad (3)$$

Fig. 4.9 shows the energy band levels of SnO_2, MoS_2, and CB before integration and Fig. 4.10 displays the schematic illustrations of the band diagrams of SnO_2, MoS_2, and CB and junction formation of SnO_2/MoS_2 and $CB/SnO_2/MoS_2$. MoS_2 consisting of an indirect bandgap of 1.3 eV [47] showing p-type semiconducting behavior and its main charge carriers are holes, so after the incorporation of n-type SnO_2 NPs (3.6 eV) [48], the majority of high energy sites available on the surface of MoS_2 are occupied by the nucleation of SnO_2. Upon the exposure of electrophilic NO_2, the decrease in electric resistance in heterostructures depicts that SnO_2/MoS_2 and $CB/SnO_2/MoS_2$ also show p-type semiconducting behaviors. From the resistance curves, it is observed that the initial resistance of MoS_2 is lower than that of SnO_2, which signifies the transfer of holes from p-type MoS_2 to n-type SnO_2 and the direction of flow of electrons in MoS_2 is opposite due to the difference in their respective work functions. During the formation of SnO_2/MoS_2, an equilibrium state is achieved at the heterojunction and a potential barrier is generated by the recombination of electron-hole and bending of the band levels which causes the broadening in the depletion layer that prohibits the transfer of carriers at the p-n heterogeneous region. The adsorption mainly caused by the defects is restricted, and the electronic effect created due to the p-n-junction becomes dominant and electrons from SnO_2 NPs are trapped by NO_2 gas molecules and lower their electron concentration causing the band bending. During adsorption, a larger number of holes gathers at the MoS_2 surface, which significantly depletes the potential barrier and decreases the resistance of SnO_2/MoS_2 heterostructures. For the $CB/SnO_2/MoS_2$ sensor, the sensitivity to NO_2 is significantly greater than SnO_2/MoS_2 and MoS_2, which not merely due to the formation of p-n junction between MoS_2 and SnO_2 but also due to CB, which endows p-type semiconducting behavior with the higher electrical conductivity to the sensing material having bandgap as 1.96 eV [49] and the Schottky barrier between CB and SnO_2 plays a crucial role. Since the work function of SnO_2 (4.85 eV) is higher than CB (4.5 eV), the holes will gather on to the SnO_2 side until the Fermi level reaches equilibrium and a potential barrier is generated at the interface and when the NO_2 molecules contact the $CB/SnO_2/MoS_2$ surface, NO_2 molecules provide electrons to the CB and decrease the potential barrier width causing a dramatic decrease

in the resistance. Based on the discussed sensing mechanisms for NO_2 gas, the p-n heterojunctions amid CB-SnO_2, and MoS_2-SnO_2, and the Schottky barrier between CB and SnO_2/MoS_2 collectively accelerate the sensor response towards NO_2 gas.

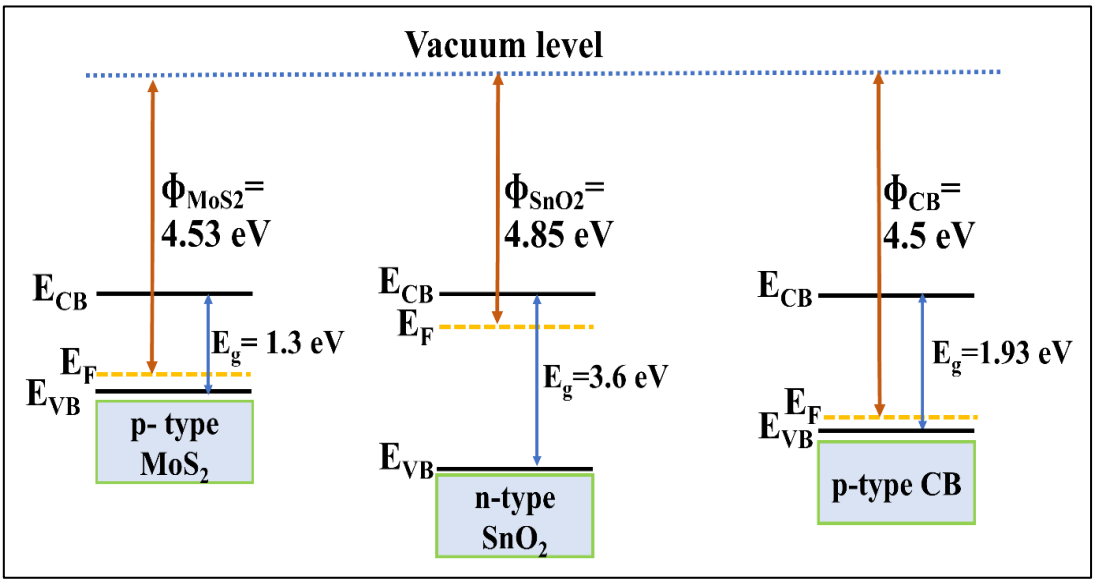

Fig. 4.9: Energy band diagrams of MoS_2, SnO_2, and Carbon black (CB) before functionalization

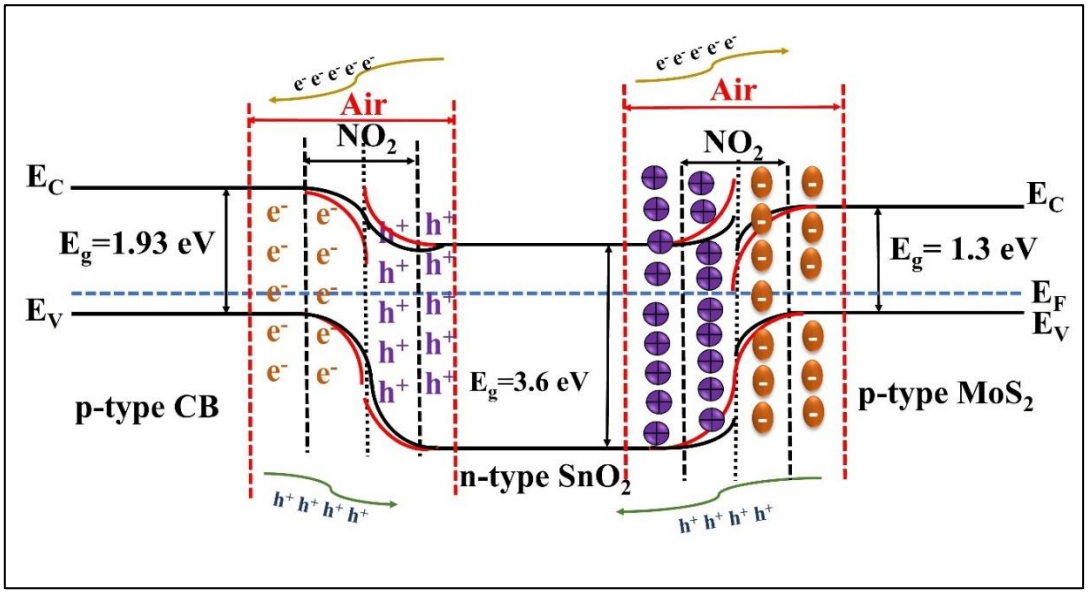

Fig. 4.10: Energy Band alignments and junction formation between $CB/SnO_2/MoS_2$ in the presence of air and NO_2

4.5 Conclusion

In this work, a low-cost synthesis route has been used to prepare a ternary nanocomposite of $CB/SnO_2/MoS_2$. The results indicate that the ternary heterostructure-based gas sensor shows a higher sensing response toward NO_2 about (46%) with a faster response time (26 s) and recovery time (73 s) near room temperature (30 ˚C), which is better than bare MoS_2 and binary SnO_2/MoS_2-based sensors. The transient response curves show the sensor response increased with NO_2 gas concentration from 1 to 100 ppm. The sensing mechanism of the sensors has been explained by chemical and electronic sensitization.

References

[1] L. Tamburino, G. Bravo, Y. Clough, and K. A. Nicholas, "From population to production: 50 years of scientific literature on how to feed the world," *Glob. Food Sec.*, vol. 24, 2020.

[2] Y. Huang *et al.*, "High Sensitivity, Humidity-Independent, Flexible NO_2, and NH_3 Gas Sensors Based on SnS_2 Hybrid Functional Graphene Ink," *ACS Appl. Mater. Interfaces*, vol. 12, no. 1, pp. 997–1004, 2020.

[3] F. Ricciardella *et al.*, "Calibration of Nonstationary Gas Sensors Based on Two-Dimensional Materials," *ACS Omega*, vol. 5, no. 11, pp. 5959–5963, 2020.

[4] B. I. Adamu, P. Chen, and W. Chu, "Role of nanostructuring of sensing materials in the performance of electrical gas sensors by combining with extra strategies," *Nano Express*, vol. 2, no. 4, 2021.

[5] N. Joshi, T. Hayasaka, Y. Liu, H. Liu, O. N. Oliveira, and L. Lin, "A review on chemiresistive room temperature gas sensors based on metal oxide nanostructures, graphene and 2D transition metal dichalcogenides," *Microchim. Acta*, vol. 185, 2018.

[6] J. Shin, S. Han, S. Noh, Y. T. Yu, and J. S. Kim, "Room-temperature operation of light-assisted NO_2 gas sensor based on GaN nanowires and graphene," *Nanotechnology*, vol. 32, no. 50, 2021.

[7] T. Gessner *et al.*, "Metal oxide gas sensor for high-temperature application," *Microsyst. Technol.*, vol. 6, pp. 169–174, 2000

[8] A. Mukherjee, L. R. Jaidev, K. Chatterjee, and A. Misra, "Nanoscale heterojunctions of rGO-MoS_2 composites for nitrogen dioxide sensing at room temperature," *Nano Express*, vol. 1, no. 1, pp. 0–13, 2020.

[9] E. Lee, Y. S. Yoon, and D. J. Kim, "Two-Dimensional Transition Metal Dichalcogenides and Metal Oxide Hybrids for Gas Sensing," *ACS Sensors*, vol. 3, no. 10, pp. 2045–2060, 2018.

[10] G. Deokar *et al.*, "MoS_2 – Carbon Nanotube Hybrid Material Growth and Gas Sensing," vol. 4, Issue 24, 1700801, pp. 1–10, 2017.

[11] X. Liu, T. Ma, N. Pinna, and J. Zhang, "Two-Dimensional Nanostructured Materials for Gas Sensing," *Adv. Funct. Mater.*, vol. 27, no. 37, pp. 1–30, 2017.

[12] S. W. Lee, W. Lee, Y. Hong, G. Lee, and D. S. Yoon, "Recent advances in carbon material-based NO2 gas sensors," *Sensors Actuators, B Chem.*, vol. 255, no. 2, pp. 1788–1804, 2018.

[13] V. Tjoa, W. Jun, V. Dravid, S. Mhaisalkar, and N. Mathews, "Hybrid graphene-metal nanoparticle systems: Electronic properties and gas interaction," *J. Mater. Chem.*, vol. 21, no. 39, pp. 15593–15599, 2011.

[14] S. Yang, C. Jiang, and S. Huai Wei, "Gas sensing in 2D materials," *Appl. Phys. Rev.*, vol. 4, no. 2, 021304, 2017.

[15] Y. Han et al., "Construction of MoS2/SnO2 heterostructures for sensitive NO2 detection at room temperature," Appl. Surf. Sci., vol. 493, pp. 613–619, 2019.

[16] S. Singh, Sukhwinder; Sharma, Shivani; Singh, Ravi Chand ; Sharma, "Hydrothermally synthesized MoS2-multi-walled carbon nanotube composite as a novel room-temperature ammonia sensing platform," *Appl. Surf. Sci.*, vol. 532, p. 147373, 2020.

[17] F. Mendoza, D. M. Hernández, V. Makarov, E. Febus, B. R. Weiner, and G. Morell, "Room temperature gas sensor based on tin dioxide-carbon nanotubes composite films," *Sensors Actuators, B Chem.*, vol. 190, pp. 227–233, 2014.

[18] A. G. Bannov, M. V. Popov, A. E. Brester, and P. B. Kurmashov, "Recent advances in ammonia gas sensors based on carbon nanomaterials," *Micromachines*, vol. 12, no. 2. 2021.

[19] P. Dariyal, S. Sharma, G. S. Chauhan, B. P. Singh, and S. R. Dhakate, "Recent trends in gas sensing via carbon nanomaterials: outlook and challenges," *Nanoscale Advances*, vol. 3, pp. 6514–6544, 2021.

[20] K. Arshak, E. Moore, L. Cavanagh, J. Harris, B. Mcconigly, and C. Cunniffe, "Determination of the electrical behavior of surfactant treated polymer/carbon black composite gas sensors," vol. 36, 4, pp. 487–491, 2005.

[21] T. N. Murakami *et al.*, "Highly Efficient Dye-Sensitized Solar Cells Based on Carbon Black Counter Electrodes," *J. Electrochem. Soc.*, vol. 153, no. 12, 2006.

[22] C. Zhou, G. Xie, X. Du, and P. Sun, "A gas sensor based on polyhexylthiophene-carbon black for NO_2 detection," *2009 Int. Conf. Opt. Instruments Technol. Adv. Sens. Technol. Appl.*, vol. 7508, no. 2, p. 75081B, 2009.

[23] B. Ding, M. Wang, J. Yu, and G. Sun, "Gas sensors based on electrospun nanofibers," *Sensors*, vol. 9, no. 3, pp. 1609–1624, 2009.

[24] H.-M. Liou, Wei-Jen; Lin, "Nanohybrid TiO_2-carbon black sensor for NO2 gas," *China Particuology*, vol. 5, pp. 225–229, 2007.

[25] Z. Chu *et al.*, "3D porous α-$Ni(OH)_2$ nanostructure interconnected with carbon black as a high-performance gas sensing material for NO_2 at room temperature," *RSC Adv.*, vol. 5, pp. 101760–101767, 2015.

[26] M. C. Lonergan, M. S. Freund, E. J. Severin, B. J. Doleman, R. H. Grubbs, and N. S. Lewis, "Array-based vapor sensing using chemically sensitive, polymer composite resistors," *IEEE Aerosp. Appl. Conf. Proc.*, Snowmass, CO, USA, 1997, pp. 583–631.

[27] E. Llobet, "Gas sensors using carbon nanomaterials: A review," *Sensors and Actuators, B: Chemical*, vol. 179. pp. 32–45, 2013.

[28] R. Gómez-Hernández, Y. Panecatl-Bernal, and M. Á. Méndez-Rojas, "High yield and simple one-step production of carbon black nanoparticles from waste tires," *Heliyon*, vol. 5, no. 7, 2019.

[29] F. Khairi, C. Harun, A. M. Jumadi, and N. H. Mahmood, "Gas sensor based on carbon black polymer composite for electronic nose," *Elektr. J. Electr. Eng.*, vol. 13, no. 2, pp. 1–7, 2011.

[30] H. Yan, P. Song, S. Zhang, Z. Yang, and Q. Wang, "Dispersed SnO_2 nanoparticles on MoS2 nanosheets for superior gas-sensing performances to ethanol," *RSC Adv.*, vol. 5, pp. 79593–79599, 2015.

[31] N. Duc *et al.*, "Carbon Nanotubes : Synthesis via Chemical Vapour Deposition without Hydrogen, Surface Modification, and Application," vol. 2019, 2019.

[32] J. D. Benck, Z. Chen, L. Y. Kuritzky, A. J. Forman, and T. F. Jaramillo, "Amorphous molybdenum sulfide catalysts for electrochemical hydrogen production: Insights into the origin of their catalytic activity," *ACS Catal.*, vol. 2, no. 9, pp. 1916–1923, 2012.

[33] N. Xue and P. Diao, "Composite of Few-Layered MoS_2 Grown on Carbon Black: Tuning the Ratio of Terminal to Total Sulfur in MoS_2 for Hydrogen Evolution Reaction," *J. Phys. Chem. C*, vol. 121, no. 27, pp. 14413–14425, 2017.

[34] B. Babu, I. Neelakanta Reddy, K. Yoo, D. Kim, and J. Shim, "Bandgap tuning and XPS study of SnO_2 quantum dots," *Mater. Lett.*, vol. 221, pp. 211–215, 2018.

[35] Y. Zou *et al.*, "Highly efficient gas sensor using a hollow SnO_2 microfiber for triethylamine detection," *ACS Sensors*, vol. 2, no. 7, pp. 897–902, 2017, doi: 10.1021/acssensors.7b00276.

[36] S. Singh, R. M. Sattigeri, S. Kumar, P. K. Jha, and S. Sharma, "Superior Room-Temperature Ammonia Sensing Using a Hydrothermally Synthesized MoS_2/SnO_2 Composite," *ACS Omega*, vol. 6, no. 17, pp. 11602–11613, 2021.

[37] J. Shakya, S. Kumar, D. Kanjilal, and T. Mohanty, "Work Function Modulation of Molybdenum Disulfide Nanosheets by Introducing Systematic Lattice Strain," *Sci. Rep.*, vol. 7, 9576, 2017.

[38] S. Gubbala *et al.*, "Surface properties of SnO_2 nanowires for enhanced performance with dye-sensitized solar cells," *Energy Environ. Sci.*, vol. 2, pp. 1302–1309, 2009.

[39] V. Likholobov and P. Simonov, Physicochemical Aspects of Preparation of Carbon-Supported Noble Metal Catalysts, no. 14, Taylor & Francis Group, LLC, 2003.

[40] S. Kumar *et al.*, "Nanocomposites of Quasicrystal Nanosheets and MoS2 Nanoflakes for NO2 Gas Sensors," *ACS Appl. Nano Mater.*, vol.6, no.7, pp. 5952-5962, 2023.

[41] M. Boomashri *et al.*, "Detection of ammonia gas at room temperature through Sb doped SnO_2 thin films: Improvement in sensing performance of SnO2," *Ceram. Int.*, vol. 49, no. 6, pp. 10096–10106, 2023.

[42] S. Kumar, G. Meng, P. Mishra, N. Tripathi, and A. G. Bannov, "A systematic review on 2D MoS2 for nitrogen dioxide (NO_2) sensing at room temperature," *Materials Today Communications*, vol. 34, 105045, 2023.

[43] M. States *et al.*, "Bandgap, Mid-Gap States, and Gating Effects in MoS_2," *Nano Lett.*, vol.14, no.8, pp. 4628-4633, 2014.

[44] P. Kakoty and M. Bhuyan, "SnO2 based gas sensors: Why it is so popular?," *IEEE Inter. Conference on Electrical, Computer and Communication Technologies (ICECCT)*, Coimbatore, India, 2015.

[45] A. P. S. Chauhan and K. Chawla, "Comparative studies on Graphite and Carbon Black powders, and their dispersions," *J. Mol. Liq.*, vol. 221, pp. 292–297, 2016.

Chapter – 5

Investigation of the Gas Sensing Performance of MoS_2/MoO_3-Based Gas Sensors for NH_3 and NO_2 Gas Simultaneously at Ambient Conditions

CHAPTER – 5

INVESTIGATION OF THE GAS SENSING PERFORMANCE OF MoS_2/MoO_3-BASED GAS SENSORS FOR NH_3 AND NO_2 GAS SIMULTANEOUSLY AT AMBIENT CONDITIONS

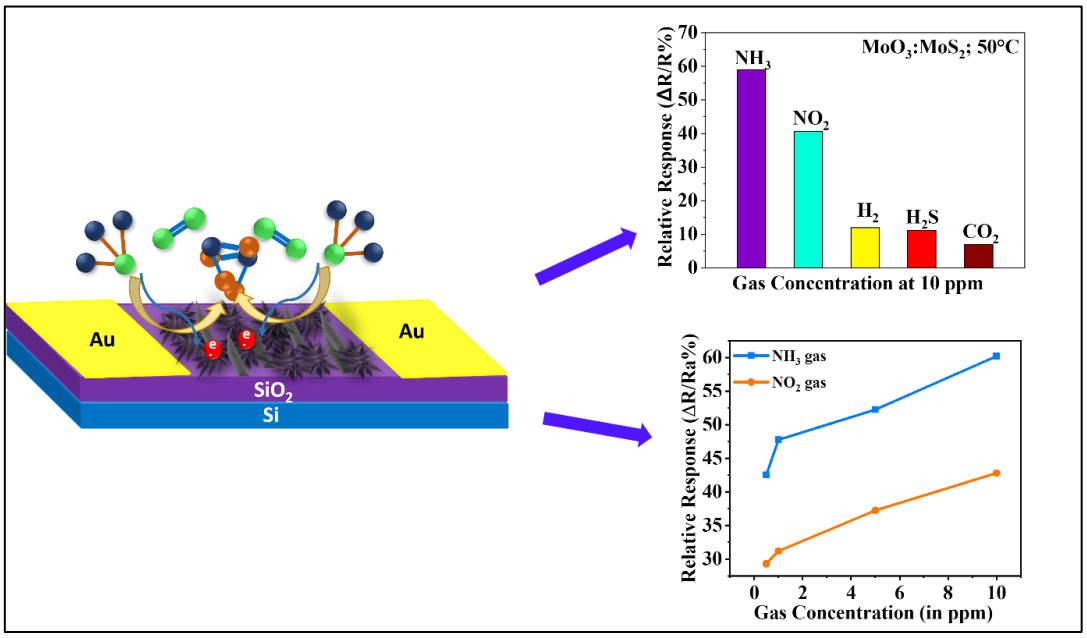

In this chapter, highly sensitive p-MoS_2/n-MoO_3 nanocomposite-based chemo-resistive gas sensors are synthesized by varying the reducing agents using hydrothermal synthesis followed by thermal annealing in an Ar environment for NH_3 and NO_2 detection at 50 ˚C. Structural characterizations confirmed the existence of MoS_2 nanoflakes and MoO_3 nanoplatelets and the appearance of abundant oxygen adsorption sites and sulfur vacancies in the nanocomposites. The MoS_2:MoO_3-based sensor (without any reducing agent) showed preferential detection of NH_3 with 52% sensor response for 5 ppm gas concentration having response/ recovery times of 28 s/97 s with n-type sensing behavior dominated by MoO_3 charge carriers. On the contrary, NO_2 gas attracts electrons from the MoS_2 surface, exhibiting p-type sensing behavior with a sensor response of 42 % consisting of response/recovery times of 56 s/116 s with 5ppm concentration at 50˚C. More interestingly, different adsorption sites and conductive channels play a huge role in the MoS_2:MoO_3 nanocomposite for exhibiting opposite sensing behaviors upon exposure to NH_3 and NO_2 gases. Enhanced sensitivity is

dedicated to synergistic effects appearing due to the construction of p-n heterojunction to strengthen carrier transport by enhancing the sensor response. The present work provides a unique methodology for constructing MoS_2:MoO_3-based sensors and the effect of reducing agents on various MoS_2:MoO_3-based sensors. Moreover, our study recommends the plausible use of the MoS_2:MoO_3 composite-based heterojunctions to provide a constructive strategy for improving the performance of gas sensors.

5.1 Introduction

In modern times, continuously growing energy demand due to increased population and continued economic development is leading to irrevocable environmental deterioration, which has become one of the biggest challenges for human beings. Today, air pollution is a major concern for public and environmental health in the industrialized economies. Effective detection of toxic gases and continuous tracking of hazardous pollutants have become an important concern of intensive research to prevent environmental deterioration [1]. Gas sensors are of paramount importance not only in environmental and industrial monitoring but also for food safety and medical diagnosis [2]. Especially, interest in gas sensors based on traditional resistive metal oxide semiconductors is fomented by their highly desirable attributes such as good sensitivity, low cost, and easy implementation. However, their high operating temperature (100-500 ˚C) and inadequate long-term stability make them unsuitable for selective and energy-efficient gas detection [3], [4]. In this regard, a lot of work goes into creating room temperature-based gas sensors with a variety of detecting materials to achieve low power consumption, cheap cost, and simple implementation; yet, in some environments, the low sensitivity is unable to meet the requirements. Therefore, designing a gas sensor with high sensitivity, strong stability, and improved selectivity near room temperature is crucial.

To date, various low-dimensional materials such as graphene, reduced graphene oxide (rGO) [5], carbon nanotubes (CNTs) [6], and other two-dimensional materials including transition metal dichalcogenides (TMDCs) and their composites [7],[8] have emerged as good gas sensing materials along with traditional metal oxide semiconductors (MOS). In recent years, TMDCs have emerged as analogous to graphene in gas sensing applications. MoS_2, being the most studied material of the

TMDCs family varies its bandgap with respect to the change in layers. Multilayer MoS_2 possesses an indirect bandgap (~1.2 eV) [9] and shows a higher current flow capability than the monolayer due to the availability of a higher density of states [10]. In addition, The potential of chemically synthesized multilayer MoS_2 for improved sensing of NH_3, NO_2, and other volatile gases has been investigated [9]. Due to the huge surface-area-to-volume ratio, low dimensional materials-based sensors have the advantages of high sensitivity and room temperature operation [11]. Nevertheless, the response or recovery times at room temperature are sluggish [10], especially for high adsorption energy gases such as NO_2 which is one of the major components of air pollution that is highly toxic and dangerous, especially targets the human respiratory system and causes severe heart ailments such as heart failure even at very low concentration (sub-ppm) [12]. Along with NO_2, NH_3 is also an irritant to the respiratory system, skin, and eyes [13]. Besides NH_3 is also served as an effective gaseous marker for the putrefaction detection of dairy, pharmaceuticals, and refrigeration facilities [14][15]. Besides all the important usages, as NH_3 is highly reactive and reacts with nitric acid and sulfuric acid in the air to generate aerosols, ammonium nitrate, and ammonium sulfate, respectively, it is classified as an environmental pollutant. [16]. Also, The human body produces both NO_2 and NH_3 as natural biosystem gases, and both can be employed as indicators to identify lung diseases [17]. Therefore, the development of quick and sensitive sensors is essential for detecting low concentrations of NO_2 and NH_3 at room temperature.

In recent years, several approaches, including doping and heterostructure formation using semiconducting materials, have been developed to solve challenges with high operating temperatures and slow response/recovery rates. Such strategies can, in some cases, enhance the performance of gas sensors using the multiple effects of nanostructuring [18] [7]. According to previous research, considerable improvements in sensing performance can be attained by mixing MoS_2 and MOS by developing their composites. Further, temperature-based dual gas sensing using other 2D materials has been reported for H_2/CO and NH_3/NO_2, H_2S/ethanol, etc. *Singh et. al* reported a MoS_2/WO_3 composite fabricated for the detection of H_2S (0.5 ppm) at 320 ˚C and ethanol (5 ppm) at 260 ˚C [19]. In another work, *Huang et. al* reported sulfonated rGO-decorated SnS_2 materials for NO_2 (in ppb) and NH_3 (in ppm) detection at room

temperature [20]. Alternatively, *Perrozzi et. al* reported the temperature-dependent gas sensing properties of WS_2/WO_3 composite for H_2 (1 ppm), NH_3(1ppm), and NO_2 (100 ppm) at 150˚C operating temperature [21]. Regardless of advances in 2D materials for dual detection of gases under a variety of environmental conditions, no previous reports claim dual detection of NO_2 and NH_3 using MoS_2:MoO_3 nanocomposite. The adsorption/desorption capacity of gas molecules and the introduction of oxygen vacancies for more adsorption sites play a critical role in effectively enhancing the response of the gas sensors. This may be possible due to the interaction between the different surface atoms, enabling MoS_2:MoO_3 to be an ideal gas-sensing nanomaterial.

Under inspiration from the above-discussed studies, herein, we report the formation of MoS_2:MoO_3 nanocomposites via a two-step method and have tried to express the effect of reducing agents used for the preparation of MoS_2. Hydrazine Hydrate (HH) and L-ascorbic acid (LA) are the two reducing agents, conventionally used in the hydrothermal synthesis of MoS_2. This article provides a description of the effect of reducing agents on MoS_2 and the effect of thermal annealing to prepare MoS_2:MoO_3 composites has also been demonstrated. Under the thermal annealing effect, the hydrothermally prepared MoS_2 nanoflakes are crystallized by removing extra oxygen and forms maximum amount of heterojunctions after assembly [22]. The thermal annealing results in constructing a hierarchical structure and developing several heterojunctions thereby making use of the geometrical and electronic effects together [23]. The superior sensing properties of MoS_2:MoO_3 gas sensors at room temperature are encouraged by the heterojunctions that occur at the heterostructure interface in terms of the electronic effects. The present research emphasizes the possible application of these heterostructures for the temperature-dependent, selective detection of a variety of harmful gases.

5.2 Experimental Details

5.2.1 Preparation of MoO_xS_y Nanostructures

5.2.1.1 Preparation of MoO_xS_y without any Reducing Agents

1.24 g of Ammonium Molybdate Tetrahydrate (AMT) ($(NH_4)_6Mo_7O_{24}.4H_2O$) and 0.9 g of Thiourea were dissolved in 50 ml of DI water under continuous stirring for 45 min.

Then, the obtained mixture was kept in a Teflon-lined stainless-steel autoclave in the oven at 200 ˚C for 24 h. Later, it was set to cool down to room temperature naturally. The resultant mixture was collected and washed by centrifugation using ethanol and DI water. The obtained precipitates were then dried at 110 ˚C for 12 h.

5.2.1.2 Preparation of MoO_xS_y with Reducing Agents

1.24 g of AMT and 0.9 g of thiourea were dissolved in the same volume of DI water and stirred for 45 min. Next, 8 ml of HH/ 0.02 g of LA was added to the above-mixed solution during stirring. Then, the resultant mixture was put into a 100 ml Teflon-lined stainless-steel autoclave and placed in the oven at 200˚C for 24 h. Later, it was allowed to cool down to room temperature naturally. The final solution was collected and washed multiple times using ethanol and DI water by centrifugation. The obtained precipitates were collected and kept for drying at 110 ˚C for 12 h.

5.2.1.3 Preparation of MoS_2:MoO_3 Nanostructures

As the disulfides of Mo are strongly prone to oxidation, MoS_2 may also be oxidized to trioxides at elevated temperatures [24]. In this work, the preparation of MoS_2:MoO_3 heterostructures was achieved using thermal annealing of MoO_xS_y nanostructures. The synthesized materials underwent thermal treatment and were annealed at 500˚C for 1h in the presence of Ar gas with a flow rate of 80 sccm to form controlled crystallized MoS_2:MoO_3 nanocomposites. The hybrid nanostructures are labeled as MoS_2:MoO_3 (without any reducing agent); HH-MoS_2:MoO_3 and LA-MoS_2:MoO_3 according to the used reducing agents. Figure 5.1 shows the complete synthesis of various MoS_2:MoO_3 nanostructures using hydrothermal synthesis followed by thermal annealing.

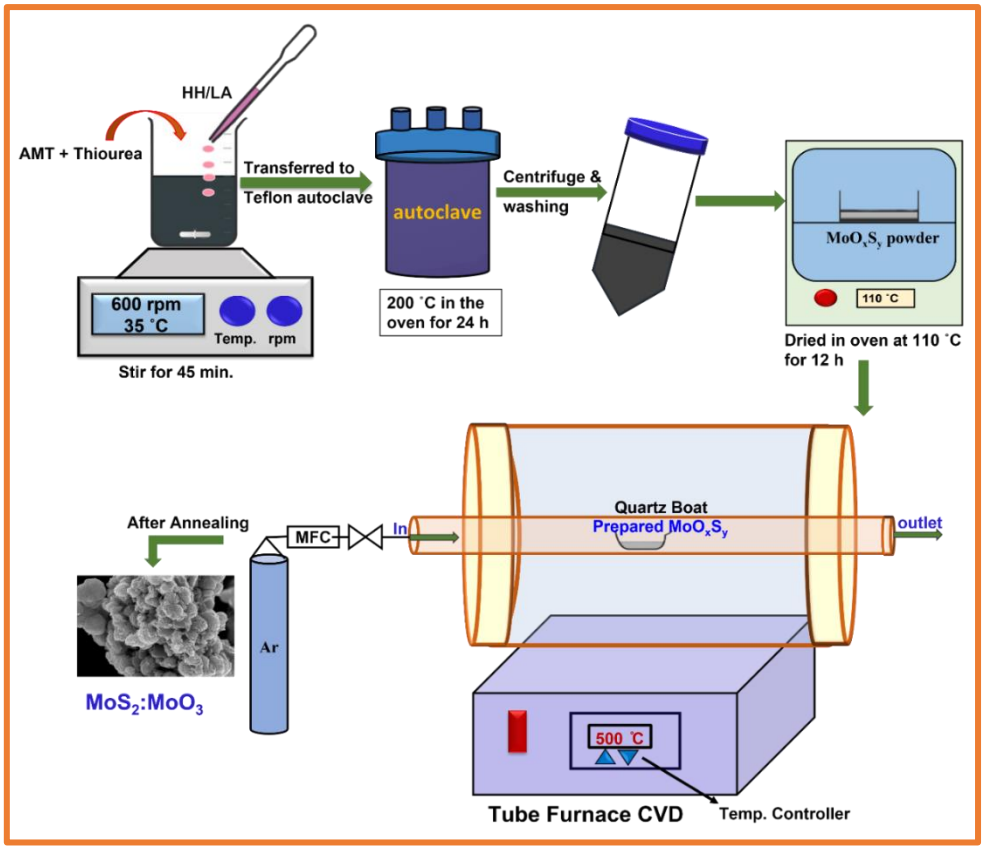

Fig. 5.1: Schematic illustration of the synthesis procedure of MoS_2:MoO_3 composite using hydrothermal method followed by partial thermal annealing

5.2.2 Material Characterizations

The Ultima III Rigaku X-ray diffractometer was used to record X-ray diffraction (XRD) data with Cu Kα1 radiation (1.54 Å) at a scanning rate of 2˚/min over a range of 10-70˚. The morphology of the materials was investigated using transmission electron microscopy (TEM) and scanning electron microscopy (SEM). Raman Spectra with an excitation wavelength of 532 nm were recorded to investigate the vibrational modes. To ascertain the chemical states of constituent elements and the coexistence of MoS_2 and MoO_3 in the composite created after annealing, X-ray photoelectron spectroscopy (XPS, Scientific K-Alpha, Al K_α) was employed.

5.2.3 Sensor Fabrication and Measurements

To fabricate the gas sensors, first, a thermal evaporation technique was employed to prepare the interdigitated gold (Au) electrodes on SiO_2/Si substrates while a shadow

mask was in place. Furthermore, 20 µL of the sensitive material mixture was drop-casted onto the formerly deposited Au interdigitated electrodes (finger width: 100 µm), and the electrodes were dried at 100 ˚C for 20 minutes. as illustrated in Fig. 5.2. These devices were used as NH_3 and NO_2 gas sensors. All gas sensing tests were performed at 50 ˚C. The sensor response (S) of the fabricated sensor was determined using the formula $S = \Delta R/R_a$ %; $\Delta R = R_a - R_g$, in which R_a represents the sensor's initial electric resistance in air and R_g denotes its resistance in the target gas environment and the gas sensing measurements were performed in a static gas sensing chamber. The intervals of time required for the resistance to achieve 90% of its equilibrium resistance following the injection and removal of the target gases, respectively, are referred to as the response and recovery times respectively.

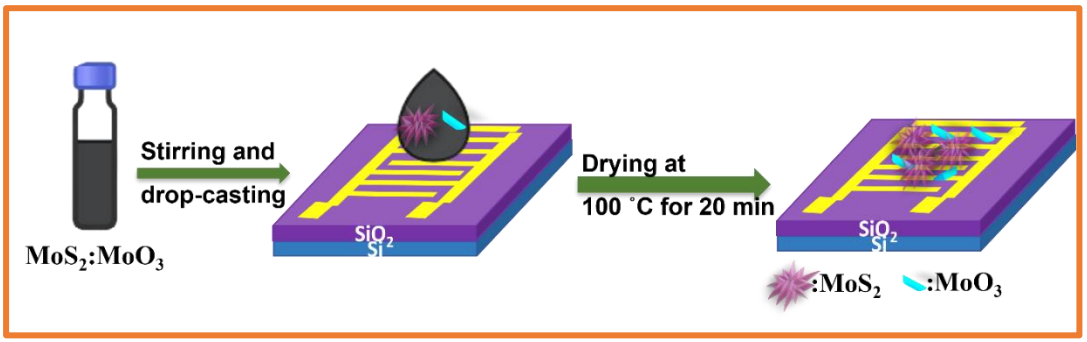

Fig. 5.2: Schematic representation of the MoS_2:MoO_3 based sensing device fabrication using drop-casting approach

5.3 Results and Discussion

5.3.1 Morphology and Microstructures of MoS_2:MoO_3 Composites

The morphology of the prepared samples (MoS_2:MoO_3) using different reducing agents was investigated through SEM imaging and further analyzed via Tunneling electron microscopy (TEM) imaging of the composites. Fig. 5.3(a-c) illustrated the self-assembled interconnected networks of MoS_2 nanoflakes compacted in a flower form for the hydrothermally synthesized samples, and the effect of thermal annealing appeared in the form of solid nano platelet-like structures providing the evidence of MoO_3. Interestingly, after annealing, the MoS_2:MoO_3 sample was found to stack into lamellar morphology of thick MoO_3 along with flower-like morphology for MoS_2. Such small nanoplatelets (NPs) were loosely stacked together to create more adsorption and

desorption sites which favors the gas sensing process. On the other hand, HH- and LA-MoS_2:MoO_3 morphology exhibited closely packed flower-like structures slightly/without the appearance of any additional morphology respectively after annealing, which was detrimental to the sensing performance. The flat lamellar microstructure formation was believed to be initiated by the crystallization of MoO_xS_y due to annealing and subsequent outward growth of the crystalline MoS_2 and amorphous MoO_3 [25][26]. Further insights into the microstructures of the flower like MoS_2 structures and lamellar structures of MoO_3 were obtained by TEM images of the same provided in Fig. 5.3(d-f). The MoS_2 nanoflakes were captured and prominently visible. It is obvious from Fig. 5.3(d-f) that the MoS_2 nanoflakes are self-assembled by sheet-like structures to form the flowers. MoS_2:MoO_3 contained visible variation in the morphology indicating the presence of MoS_2 and MoO_3 structures rather than HH-MoS_2:MoO_3 and LA-MoS_2:MoO_3 [27]. These results also indicated that MoS_2:MoO_3 is more prone to surface oxygen adsorption than HH- and LA-MoS_2:MoO_3.

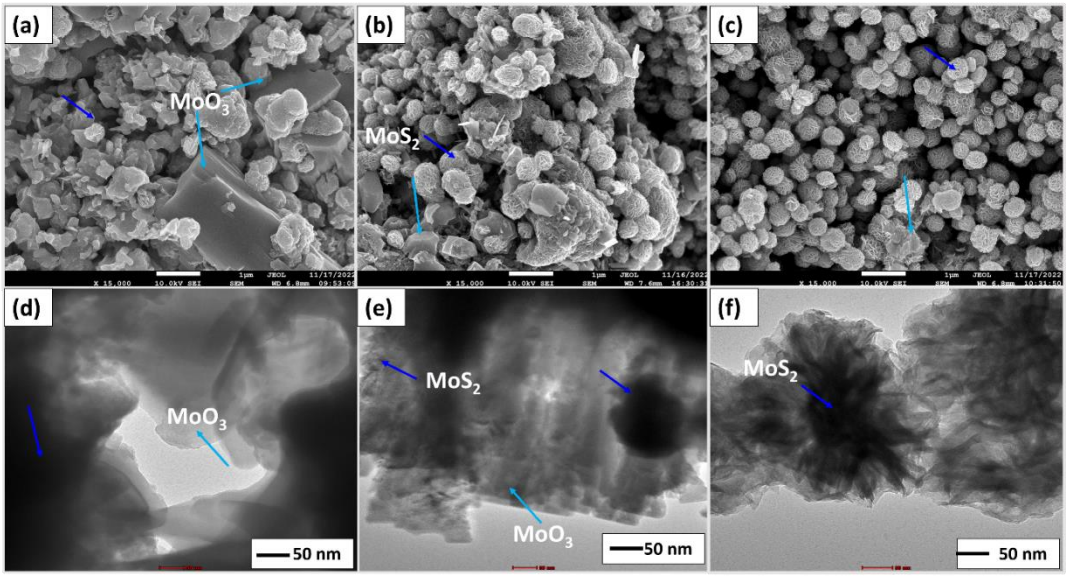

Fig. 5.3: SEM images of (a) MoS_2:MoO_3; (b) HH-MoS_2:MoO_3; (c) LA-MoS_2:MoO_3 and TEM images of (d) MoS_2:MoO_3; (e) HH-MoS_2:MoO_3; (f) LA-MoS_2:MoO_3

Fig. 5.4 (a) compares the XRD patterns of the hydrothermally synthesized samples MoS_2:MoO_3 (without using any reducing agent); HH-MoS_2:MoO_3 and LA-MoS_2:MoO_3 (with reducing agents). The distinct characteristic peaks correspond to the hexagonal phase of MoS_2 and α- phase of MoO_3, without any additional signature of

other heterophases, implying that heterostructures have attained excellent crystallinity. The obtained nanocomposites are composed of (002)-dominated MoS_2 and (040)-dominated α-MoO_3. At 500˚C, the XRD reflections related to MoO_3 became more intense. The crystallization of MoO_3 appeared in the nanocomposite which has been confirmed by the occurrence of a reflection around 26.03˚. MoS_2:MoO_3, HH-MoS_2:MoO_3, and LA-MoS_2:MoO_3 exhibited the same characteristic peaks, which are consistent with the diffraction peaks of MoO_3 and MoS_2. The peaks available at 14.1˚ and 33.7˚ were dedicated to (002) and (103) of MoS_2 and 26.03˚ and 37.4˚ were attributed to (040) and (060) of MoO_3 respectively, indicating the presence of MoS_2 and MoO_3 [28][29]. The peak present at (002) related to MoS_2 belongs to the periodicity along the c-direction indicating the stacking of multilayers in the samples and a decrease in the intensity with a broadened peak indicates the decrease in the sample size. The crystallite size of MoS_2 (002) and MoO_3 (040) for MoS_2:MoO_3, calculated by Scherrer's formula is 0.87 nm, and 2.3 nm and 0.39 nm, and 3.72 nm for HH-MoS_2:MoO_3 and 0.88 nm and 5.29 nm for LA-MoS_2:MoO_3 respectively. Further, the Raman Spectra (Fig. 5.4 (b)) confirmed the evident presence of MoS_2 and MoO_3 phases in the heterostructures. In detail, Raman spectra of MoS_2:MoO_3 contain two main peaks: an in-plane mode (E_1^{2g}) located around 377.5 cm^{-1} and an out-of-plane mode (A_{1g}) around 407.8 cm^{-1}[30]. Apart from these two modes, various Raman active modes were also found attributing to the stretching vibrations of MoO_6 octahedral [31]. The modes available around 663.8 cm^{-1} and 819.9 cm^{-1} corresponded to asymmetric stretching of triply coordinated oxygen (Mo_3-O) and the doubly connected bridge oxygen (Mo_2-O) respectively. The other peaks available at 239.1 cm^{-1}, 283.6 cm^{-1} and 334.9 cm^{-1} have been dedicated to wagging modes of O=Mo=O [32]. The difference between these two modes gives an estimation of the number of layers available in the sample [33]. In MoS_2:MoO_3, the mode separation (Δ) is 31 cm^{-1} which is more than HH-MoS_2:MoO_3 (28 cm^{-1}) and LA-MoS_2:MoO_3 (26.3 cm^{-1}). Apart from this, the Raman Spectra of LA-MoS_2:MoO_3 showed more MoS_2 features in comparison to HH-MoS_2:MoO_3 and MoS_2:MoO_3, indicating tight bonding between Mo-S bonds.

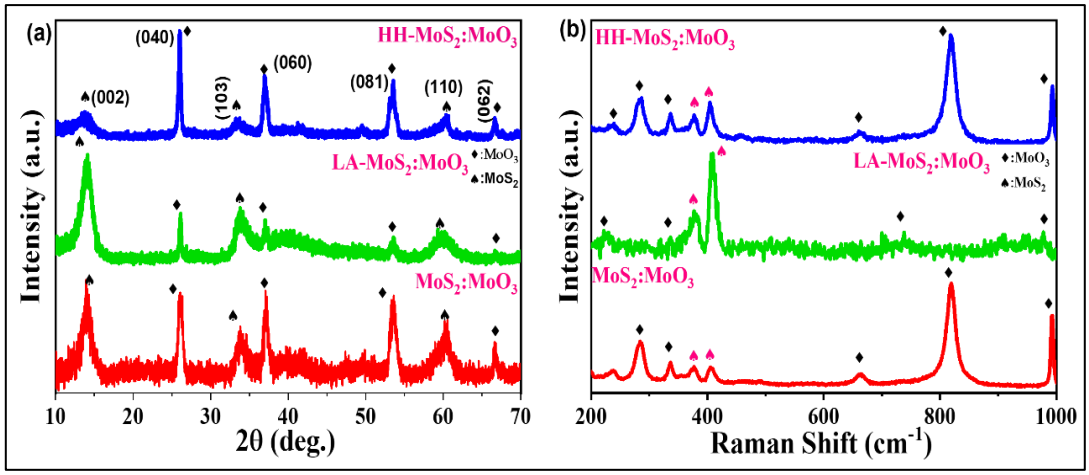

Fig. 5.4: (a) XRD patterns of MoS_2:MoO_3; LA-MoS_2:MoO_3; and HH-MoS_2:MoO_3 and (b) Raman spectra of MoS_2:MoO_3; LA-MoS_2:MoO_3; and HH-MoS_2:MoO_3

The main effect of thermal annealing was investigated by observing the chemical compositions present in the prepared MoS_2:MoO_3 composites by XPS measurements. Fig. 5.5 (a-i) shows the core level spectra of Mo 3d, S 2p, and O 1s of all three samples. The Mo 3d spectrum with the main peaks corresponding to Mo^{4+} situated at 229.1 eV and 232.4 eV dedicated to $3d_{5/2}$ and $3d_{3/2}$ respectively and peaks present at 232.8 eV and 235.8 eV were dedicated to Mo^{6+} related to MoO_3 (Fig. 5.5 (a)). HH- & LA-reduced MoS_2:MoO_3 showed two main peaks (Fig. 5.5 (d & g)) corresponding to Mo^{4+} 3d at 229.1 eV for Mo $3d_{5/2}$ and 232.4 eV for Mo $3d_{3/2}$ [34]. On the other hand, Mo^{6+} spectra corresponding to MoO_3 consist of two peaks for $3d_{5/2}$ at 232.9 eV and $3d_{3/2}$ at 235.9 eV [35]. In Fig. (5.5 (a, d & g)), it was observed that the Mo^{6+} doublet grew significantly indicating the partial conversion of MoO_xS_y under the thermal treatment resulting in MoS_2 and MoO_3 due to the decomposition of the adsorbed oxygen. So, the analysis revealed the presence of two oxidation states of Mo: Mo^{4+} 57.81 % and Mo^{6+} 32.31% in MoS_2:MoO_3. The lowering in intensity of S 2s (226.4 eV) and broadening in the peaks of Mo^{6+} in MoS_2:MoO_3 (Fig. 5.5 (a)) also indicated that MoS_2:MoO_3 prepared without any reducing agent is the least prone to oxidation in comparison to the HH- and LA- reduced MoO_xS_y [24]. In the S 2p regions (Fig. 5.5 (b, e & h)), two main peaks were observed, located around 162 eV and 163.3 eV corresponding to S^{2-} $2p_{3/2}$ and $2p_{1/2}$ respectively [36]. An extra peak available at the higher energy side was noticed in Fig. 5.5 (e & h) which further confirms the Mo^{6+} oxidation state. The unavailability of S^{6+} in Fig. 4b again confirmed less MoO_3 percentage in the

MoS_2:MoO_3 composite [37][38]. Fig. 5.5(c, f & i) shows the core level spectra of O1s where the peak appeared to be asymmetrical and mainly fitted into two distinct peaks, which are located at 530.6 eV corresponding to the main peak (O 1s) which originated from the lattice oxygen (O_L) and the other peak present at 531.6 corresponding to oxygen vacancy (O_v) dedicated to O^{2-} [37]. This may indicate the availability of lattice defects and structural distortions which may be found beneficial for gas sensing [38]. However, to enhance the gas-sensing properties, the adsorptive oxygen plays a significant part by forming the oxygen vacancies on the surface, which results in the generation of electron donors on the surface and causes an increase in electron concentration near the surface of the gas-sensing material, which affects the gas sensing properties of the samples [39]. There is another peak available at 532.5 eV corresponding to surface adsorbed oxygen (14.84%) present only in HH-MoS_2:MoO_3 in Fig. 5.5 (f) confirming that HH-MoS_2:MoO_3 is highly prone to oxidation in comparison to other samples.

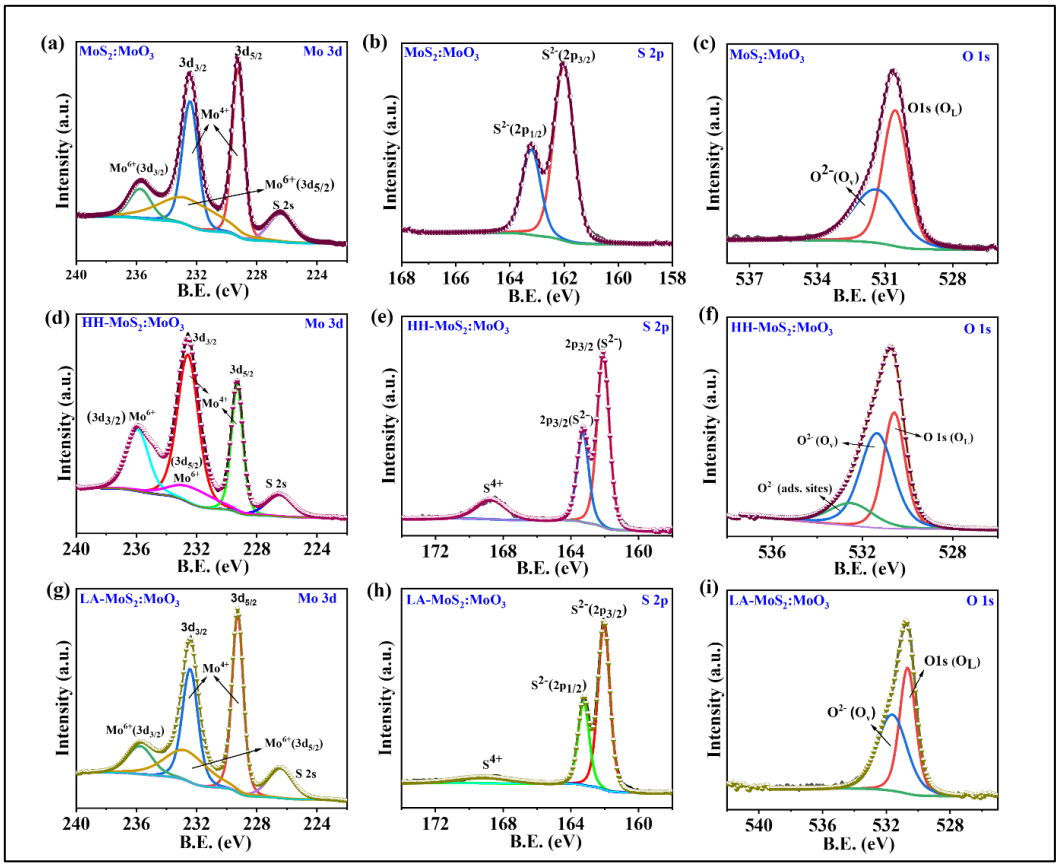

Fig. 5.5: XPS core level spectra of (a, d, g) Mo 3d; (b, e, h) S 2p and (c, f, i) O 1s of MoS_2:MoO_3; HH-MoS_2: MoO_3; LA-MoS_2: MoO_3

5.3.2 Gas Sensing Measurements

The performance of the gas sensors based on the MoS_2:MoO_3 (without reducing agent), LA-MoS_2:MoO_3, and HH-MoS_2:MoO_3 can be evaluated by their sensing response, response, and recovery time. The composition of the target gas molecules and the behavior of dominant charge carriers available in the sensing material will influence the behavior of the resistance. The gas-sensing properties of different MoS_2:MoO_3 composites were evaluated toward NH_3 at 50 ˚C at varying concentrations to understand the response transitions as illustrated in Fig. 5.6 (a-c). When NH_3 was added to the testing chamber, the resistance of the produced MoS_2:MoO_3-based sensor slowly decreased until it eventually achieved a low equilibrium value. This investigation revealed n-type sensing behavior towards NH_3, which is consistent with previous research on MoS_2:MoO_3-based sensors. The reducing gases act as electron donors, lowering the resistance of the sensing layers. [40]. From Fig. 5.7(a-c), it has been concluded that the obtained sensing response toward NH_3 gas followed the order of HH-MoS_2:MoO_3 > LA-MoS_2:MoO_3 > MoS_2:MoO_3. On the contrary, out of these three composites, only MoS_2:MoO_3 provided the complete recovery for the NH_3 gas. It has already been proven that the interaction of gas molecules on the upper surface of the gas-sensing material stimulates the sensor's gas response [41]. This can be explained by following the XPS spectra, which indicated that HH-MoS_2:MoO_3 has more oxygen vacancies and contains more adsorption sites, implying fast adsorption resulting in a higher sensing response (Fig. 5.7 (g)) but less desorption from the oxygen sites results in incomplete recovery [37].

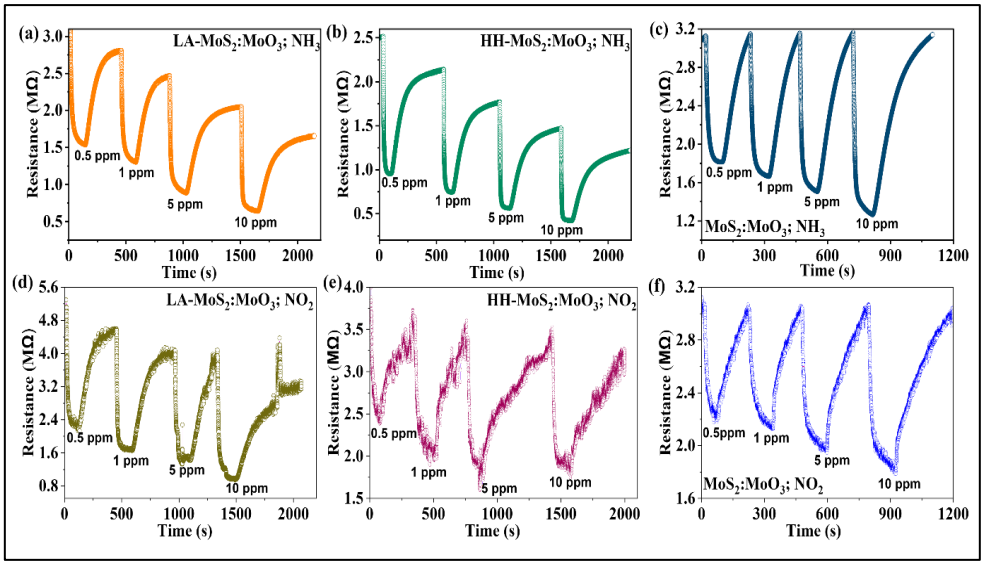

Fig. 5.6: Sensor resistance transient curves of different gas sensors for NH_3 gas at 50˚C including (a) MoS_2:MoO_3, (b) HH-MoS_2:MoO_3, and (c) LA-MoS_2:MoO_3; resistance transient curves of different gas sensors for NO_2 gas at 50˚C including (d) MoS_2:MoO_3, (e) HH-MoS_2:MoO_3, and (f) LA-MoS_2:MoO_3

The sensing behavior of MoS_2:MoO_3 composites to NO_2 gas at 50 ˚C was also investigated and shown in Fig. 5.7(d-f). For all three sensors, the sensor responses for NO_2 gas are smaller than that of NH_3 gas. The relative response of the MoS_2:MoO_3 sensor to 10 ppm NO_2 gas (Fig. 5.7 (h)) is 42.2%, for LA-MoS_2:MoO_3 is 81%, and for HH-MoS_2:MoO_3 is 48%. Besides the better relative responses, LA- and HH-MoS_2:MoO_3-based sensors faced the same issue related to incomplete recovery due to the less desorption of NO_2 molecules.

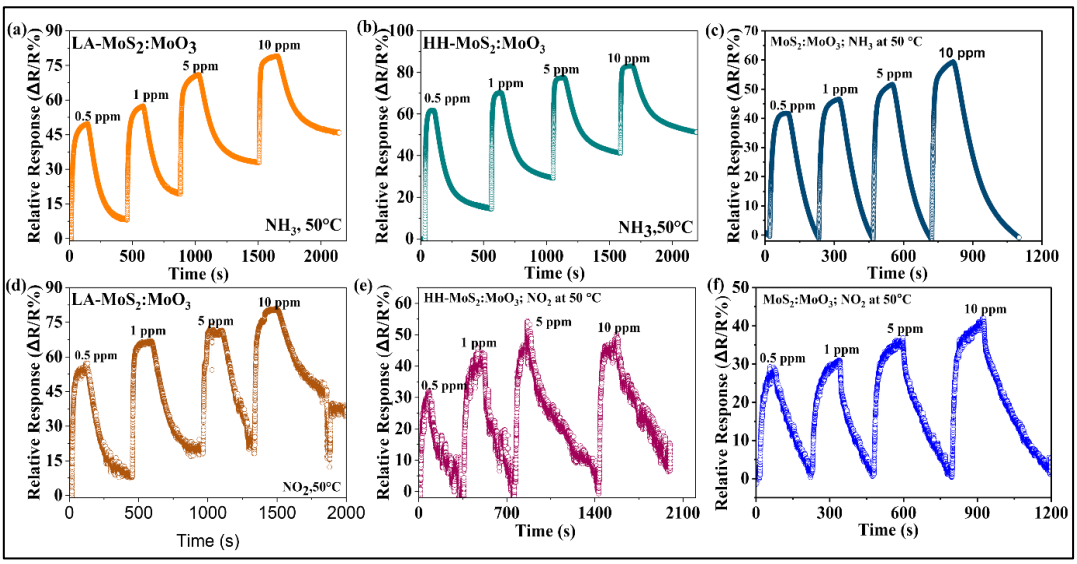

Fig. 5.7: Relative response curves of different gas sensors including (a) MoS_2:MoO_3, (b) HH-MoS_2:MoO_3, and (c) LA-MoS_2:MoO_3 for NH_3 gas; (d) MoS_2:MoO_3, (e) HH-MoS_2:MoO_3, and (f) LA-MoS_2:MoO_3 for NO_2 gas at 50˚C

To determine the performance of the sensor, cross-sensitivity becomes an essential criterion that a sensor is required to fulfill. The preferential behavior towards a specific gas concerning other gases is used to determine this. The sensing response to various gases was examined and displayed in Fig. 5.8 (a). The response to 10 ppm concentration of NH_3, NO_2, H_2, H_2S, and CO_2 at 50 ˚C are found to be 59 %, 40.9%, 12.26%, 11.68%, and 7.37% respectively, indicating a higher selectivity towards NH_3 gas. Further Fig. 5.8 (b & c) shows the comparative relative responses of all fabricated sensing devices for NH_3 and NO_2 gases respectively.

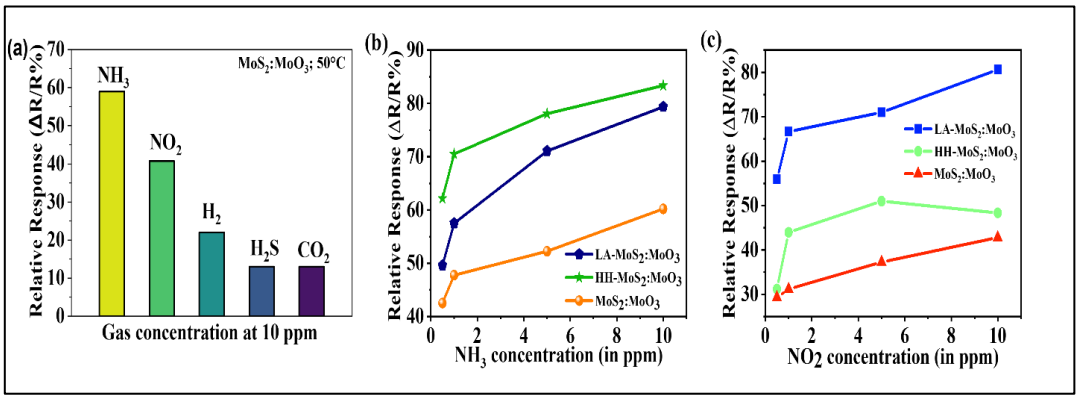

Fig. 5.8: (a) Selectivity response of MoS_2:MoO_3 based sensor for various gases at 10 ppm concentration each; (b) Comparative relative responses for NH_3 gas concentrations; (c) Comparative relative responses for NO_2 gas concentrations

To further unveil the sensing behavior of MoS_2:MoO_3, the response and recovery times (Fig. 5.9 (c & d)) of the sensing process to 5ppm NH_3 and NO_2 gases at 50 ˚C have been estimated. For MoS_2:MoO_3 sensors, the combination of electron transport and heterostructure leads to a significantly enhanced sensing response. The sensor resistances for NH_3 gas sensing reduce after NH_3 injection and return to their base value (Fig. 5.6 (c)) and the ejection of NH_3 indicates an n-type sensing behavior, suggesting that MoO_3 is a primary source of adsorption sites for NH_3. The response and recovery time of MoS_2:MoO_3 for NH_3 gas to 5ppm concentration can be calculated as 28 s and 97 s respectively as shown in Fig. 5.9 (c). Ideally, for n-type MoS_2, the resistance should increase with gas injection for NO_2 sensing, but in our case, the resistances of the MoS_2:MoO_3 sensors also decrease with exposure to NO_2 gas, indicating p-type sensing behavior (Fig. 5.6 (f)). This is in contrast to the behavior of NH_3 gas sensing, which may be made possible by the p-type semiconducting behavior of MoS_2, and suggests

that sulfur vacancies are essential for the adsorption of NO_2 molecules. For a 5 ppm NO_2 gas concentration, the response and recovery times can be calculated as 56 s and 116 s, respectively (Fig. 5.9(d)). The distinct adsorption sites for NH_3 and NO_2 on the surface of the sensing material may be the cause of this unusual behavior. The repeatability of the MoS_2:MoO_3 sensor has been performed for NH_3 and NO_2 at 10 ppm for 10 cycles as displayed in Fig. 5.9 (a & b). The sensors showed no obvious changes in the response for ten cycles of injecting and ejecting of NH_3 and NO_2 gases.

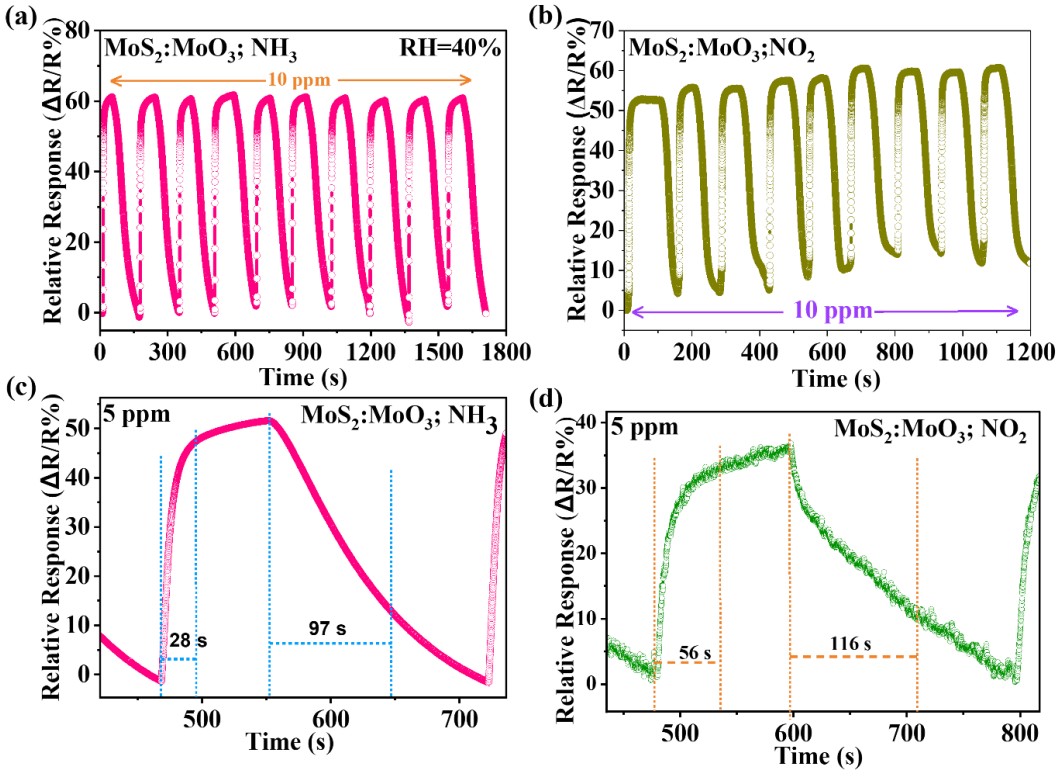

Fig. 5.9: Repeatability curves of MoS_2:MoO_3 for (a) NH_3 gas; (b) NO_2 gas at 10 ppm gas concentration at 50 ˚C each; Response and recovery time curves of MoS_2:MoO_3 at 5 ppm concentration of (c) NH_3 gas; (d) NO_2 gas

Table 5.1: Compared gas sensing performance of MoS_2/MoO_3 heterostructures with other MoS_2-based heterostructures towards NH_3 and NO_2 around room temperature

S. No.	Sensing Material	Analyte	Conc.	Sensor Response	Response/ Recovery Time	Ref.
1.	MoS_2/ZnO	NH_3	50 ppm	46.2 %	-	[42]
2.	MoS_2/CuO	NH_3	100 ppm	47%	17/26 s	[40]
3.	MoS_2/SnO_2 QDs	NH_3	100 ppm	(R_a/R_g) 8.6	6/21 s	[43]
4.	MoS_2/MWCNTs	NH_3	150 ppm	35 %	65/70 s	[44]
5.	MoS_2/WO_3	NH_3	200 ppm	207 %	80/70 s	[45]
6.	MoS_2/MoO_3	NH_3	30-40 ppm	56.2 %	60/70 s	[37]
7.	MoS_2/MoO_3	NO_2	10 ppm	33.6 %	-	[31]
8.	MoS_2/SnO_2	NO_2	100 ppm	40 %	52/198 s	[46]
9.	MoS_2/ZnO ZIF	NO_2	50 ppm	(R_a/R_g) 35	-	[47]
10.	MoS_2/MoO_3	NO_2	5 ppm	36	56/116 s	This work
11.	MoS_2/MoO_3	NH_3	5 ppm	52.3	28/97 s	This work

5.4 Gas Sensing Mechanisms

5.4.1 NH_3 Sensing Mechanism

The gas-sensing performance of metal oxides usually depends on the variations in charge concentration under the effect of air or target analytes. The main reason for the change in the electrical resistance of the sensor material is the adsorption/desorption that occurs on the sensor surface. At first, ambient oxygen molecules adsorb on the MoS_2:MoO_3 surface (eq. 1), and disintegrate into O atoms, with oxygen atoms extracting electrons from MoO_3 in the form of eq. 2. As a result, an electron depletion region generates close to the surface of n-type MoO_3. The number of electrons in MoO_3 increases as a result of a reaction between gas molecules and physically adsorbed $O_{2(ads.)}^-$ gas molecules upon exposure to a reducing gas, such as NH_3. This reaction releases the trapped electrons back into the conduction band (as shown in eq. 3), causing a shrink in the electron depletion layer for MoO_3 at the MoS_2:MoO_3 interface. As a result, a decrease in the resistance is noticed in the MoS_2:MoO_3 sensor, indicating an n-type sensing behavior of MoS_2:MoO_3 composites when exposed to NH_3, similar to

the sensing transience Fig.5.6(a-c) [42]. The resistance variation revealed that MoO_3 dominated the NH_3 gas sensing process in composites, as instead of MoS_2. The enhanced NH_3-sensing performance was related to the superposition effect induced by hetero-interface and surface modification. The sensing mechanism representation of MoS_2:MoO_3 nanocomposites for NH_3 gas can be explained as follows [45],

$$O_{2\,(gas)} \rightarrow 2O_{(ads.)} \quad (1)$$

$$O_{2(gas)} + e^-_{(from\ MoO3)} \rightarrow O_{2(ads)}^- \quad (2)$$

$$2NH_3 + 3O_{(ads)}^- \rightarrow N_2 + 3H_2O + 3e^-_{to\ MoO3} \quad (3)$$

5.4.2 NO_2 Sensing Mechanism

The gas sensing performances of MoS_2:MoO_3 nanocomposites-based sensors exhibited p-type characters as displayed in Fig. 5.6(d-f). For MoS_2:MoO_3-based NO_2 gas sensors, these results indicate that MoS_2 nanoflakes serve as the primary carriers of charge. When n-type MoO_3 NPs are incorporated with p-type MoS_2 nanoflakes, most of the high-energy binding sites on the MoS_2 surface are occupied by the nucleation of MoO_3 [46]. Defect-dominated adsorption is limited by nucleation, and the electronic effect produced by p-n junction generation becomes prominent. A depletion layer builds towards the MoO_3 side, and a charge accumulation layer forms on the surface of MoS_2, as a result of the electrons of n-type MoO_3 transferring p-type MoS_2. As a result, electron-hole diffusion proceeds until the fermi level achieves an equilibrium state. Since different types of gases have varied electron transport properties, the area nearer the p-n junction interaction serves as a potential barrier that either facilitates or inhibits electron movement. When NO_2 gas is exposed to the sensor, as shown in (Fig. 5.10 (d & g)), NO_2 molecules extract electrons from MoO_3 and decrease their charge concentration, which makes the extra holes return to MoS_2 without any further restrictions until the equilibrium is attained. During this adsorption process, additional holes accumulate on the MoS_2 nanoflakes' surface, reducing the width of the depletion layer of the heterojunction. Therefore, the improved sensor response is facilitated by the decrease in resistance values [48]. Hence, an excellent sensing performance is the outcome of changes in the energy barrier of the MoS_2:MoO_3 composite produced by NO_2 adsorption. The large surface area of MoS_2 nanoflakes and the deposited oxygen

further enhance the gas-sensing response. [49]. The gas sensing mechanism representation for NO_2 gas can be explained as follows [50]:

$$NO_2\ (gas) + e^- \rightarrow NO_2^- \quad (4)$$

$$NO_2^- + O_2^- + 2e^- \rightarrow NO_2^- + 2O^- \quad (5)$$

$$NO_2^- + V^{++} \rightarrow NO_2 + h_{VB}^+ \quad (6)$$

To establish the energy band diagrams, as shown in Fig. 5.10 (a-d), the reported bandgap energy (E_g) and work function of isolated MoS_2 and MoO_3 are used. MoO_3 is an n-type semiconductor with a wide band gap of ~ 3.40 eV [51] and MoS_2 is a p-type semiconductor with a bandgap of 1.23 eV [52]. The work function of MoS_2 is 4.6 eV and MoO_3 is 6.9 eV [53]. Due to the lower work function of MoS_2 in comparison to MoO_3, the electrons will move from MoS_2 to MoO_3 until the two semiconductors attain a uniform fermi level. As a result, due to the difference in their distinct work functions, p-n junctions developed at the interface between MoS_2 and MoO_3. A depletion layer forms at the MoS_2 and MoO_3 intersection as a result of this process [54]. When the MoS_2:MoO_3 surface is exposed to air, atmospheric oxygen interacts and converts into oxygen ions after extracting an electron from MoO_3 (Fig.5.10 (b)). When NH_3, an electron-donating gas, is introduced, it first reacts with the oxygen that has been adsorbed on the surface, removing it from the surface and also returning an electron to the semiconductor. This causes the MoO_3 side to have a higher electron concentration, which causes the energy band to bend downward and simultaneously attracts more oxygen ions to the MoO_3 surface (Fig. 5.10 (c)) concurrently attracting more oxygen ions on the MoO_3 surface. Therefore, more interaction of oxygen ions with NH_3 gas molecules would result in releasing more electrons, leading to a shrink in the depletion region, resulting in a decrease in resistance and a higher sensing response at a lower operating temperature (50˚C), indicating the n-type behavior of MoS_2:MoO_3 composite [55]. In the case of NO_2 (electron-accepting gas), NO_2 molecules extract electrons from MoO_3 NPs and lower the electron concentration, and extra holes start drifting towards MoS_2 until equilibrium is reached. During this adsorption process, the width of the heterojunction decreases (Fig. 5.10 (d)), and the sensor resistance decreases resulting in an enhancement in sensor response at 50 ˚C.

Next, for the heterojunction barriers, where MoO_3 NPs appeared on the MoS_2 surface (MoS_2:MoO_3, LA-MoS_2:MoO_3, and HH-MoS_2:MoO_3), as shown in Fig. (5.3 (a-c)), the use of different reducing agents during preparation has impacted the distribution which significantly responsible for the variation in the sensor responses. For nanocomposites, adsorption sites were exposed, enabling an improved response. However, the higher amount of O_v and $O_2^-{}_{(ads.\ sites)}$ in HH-MoS_2:MoO_3 and LA-MoS_2:MoO_3 unfavorably resulted in accumulation on the MoO_3 surface, making it more difficult to desorb from the MoO_3 surface, resulting in dissatisfied sensitivity and incomplete recovery despite having enhanced sensor response concerning MoS_2:MoO_3. In addition, XPS results (Fig. 5.5 (c, f & i)) showed more oxygen vacancies in HH-reduced MoS_2:MoO_3 than in MoS_2:MoO_3.

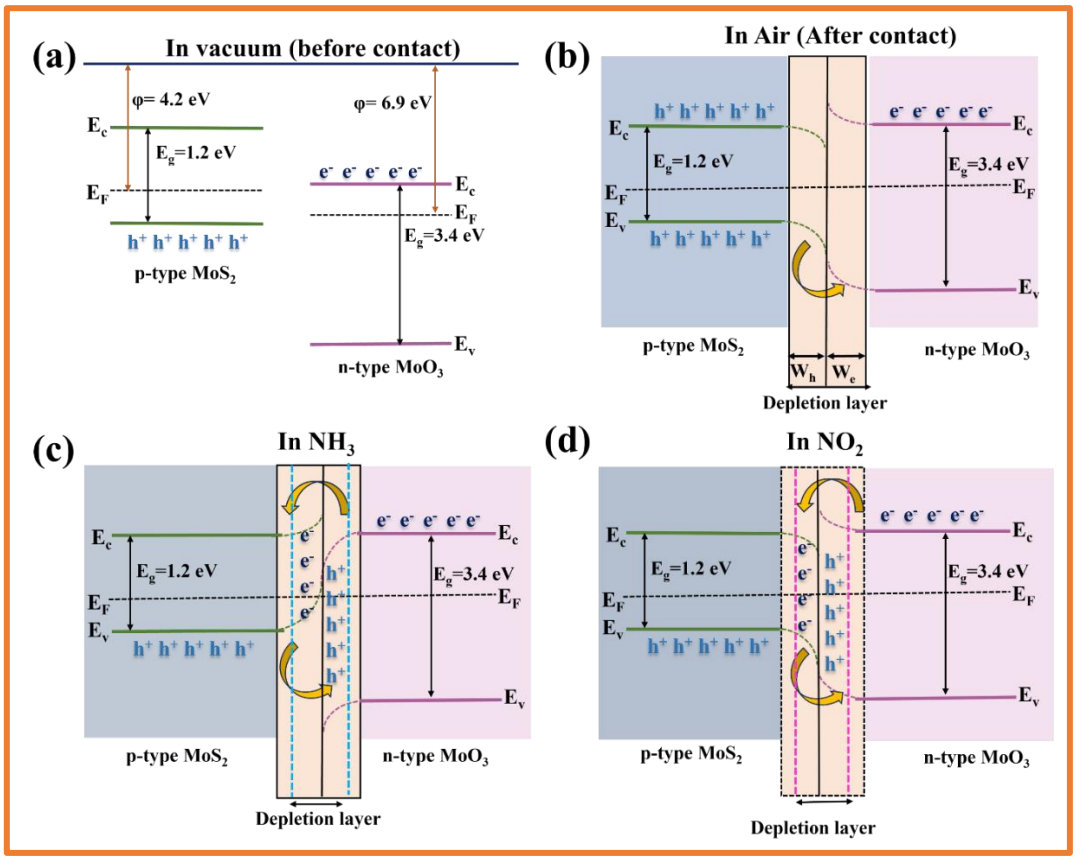

Fig. 5.10: Schematic illustration of energy bands within MoS_2:MoO_3 composites processes (a) before contact; (b) in air; (c) in NH_3; (d) in NO_2 environment

5.5 Conclusion

A simple hydrothermal method followed by thermal annealing in the Ar gas environment has been used to prepare MoS_2:MoO_3 nanocomposites to investigate their gas-sensing properties. Various characterizations such as SEM and XPS confirmed the formation of nanocomposites and the availability of abundant oxygen vacancies in the composite, inducing the gas adsorption of target gases on the surface. Based on our experimental investigations, the MoS_2:MoO_3-based sensor shows a better response of 52 % towards NH_3 gas and 37 % towards NO_2 gas at 5 ppm with fast response times of 28 s and 56 s respectively with complete recovery. In contrast, the HH-MoS_2:MoO_3-based sensor exhibited the higher sensitivity for NH_3 and NO_2 at the ppm level but incomplete recovery doesn't make them suitable for sensing. Importantly, one single sensing surface has contributed to the selective detection of NH_3 and NO_2 at 50˚C. Additionally, because distinct adsorption sites were available, the single sensing device exhibited opposing sensing behaviors towards reducing and oxidizing gases. According to the sensing reports, NO_2 is primarily adsorbed on the surface of MoS_2 whereas NH_3 is mostly adsorbed on the MoO_3 sites of the heterojunction, interacting with surface-adsorbed oxygen to draw electrons. The formation of p-n heterojunction between MoO_3 and MoS_2 has been attributed to the improved sensing performance.

References

[1] S. Dhall, B. R. Mehta, A. K. Tyagi, and K. Sood, "A review on environmental gas sensors: Materials and technologies," *Sensors Int.*, vol. 2, no. May, 2021, doi: 10.1016/j.sintl.2021.100116.

[2] X. Tian, X. Cui, Y. Xiao, T. Chen, X. Xiao, and Y. Wang, "Pt/MoS_2/Polyaniline Nanocomposite as a Highly Effective Room Temperature Flexible Gas Sensor for Ammonia Detection," *ACS Appl. Mater. Interfaces*, 2022, doi: 10.1021/acsami.2c20299.

[3] J. Zhang, X. Liu, G. Neri, and N. Pinna, "Nanostructured Materials for Room-Temperature Gas Sensors," *Advanced Materials*, vol. 28, no. 5. pp. 795–831, 2016, doi: 10.1002/adma.201503825.

[4] S. Kumar, R. Chaurasiya, M. A. Khan, G. Meng, J. S. Chen, and M. Kumar, "Enhancement of H_2S sensing performance of rGO decorated CuO thin films: experimental and DFT studies," *J. Phys. Condens. Matter*, vol. 35, no. 6, 2023, doi: 10.1088/1361-648X/aca37e.

[5] A. Lipatov, A. Varezhnikov, P. Wilson, V. Sysoev, A. Kolmakov, and A. Sinitskii, "Highly selective gas sensor arrays based on thermally reduced graphene oxide," *Nanoscale*, vol. 5, no. 12, pp. 5426–5434, 2013, doi: 10.1039/c3nr00747b.

[6] A. Boyd, I. Dube, G. Fedorov, M. Paranjape, and P. Barbara, "Gas sensing mechanism of carbon nanotubes: From single tubes to high-density networks," *Carbon N. Y.*, vol. 69, no. 2, pp. 417–423, 2014, doi: 10.1016/j.carbon.2013.12.044.

[7] E. Lee, Y. S. Yoon, and D. J. Kim, "Two-Dimensional Transition Metal Dichalcogenides and Metal Oxide Hybrids for Gas Sensing," *ACS Sensors*, vol. 3, no. 10, pp. 2045–2060, 2018, doi: 10.1021/acssensors.8b01077.

[8] S. Kumar *et al.*, "1T and 2H mixed phase WS2 nanoflakes decorated with quasicrystal nanosheets for NO_2 sensors," *J. Mater. Chem. C*, vol. 11, no. 43, pp. 15119–15129, 2023, doi: 10.1039/d3tc02524a.

[9] D. J. Late, Y. Huang, B. Liu, J. Acharya, S. N. Shirodkar, and J. Luo, "Sensing Behavior of Atomically Thin-Layered MoS_2 Transistors," no. 6, pp. 4879–4891, 2013, doi: 10.1021/nn400026u.

[10] R. Kumar, N. Goel, and M. Kumar, "UV-Activated MoS_2 Based Fast and Reversible NO_2 Sensor at Room Temperature," *ACS Sensors*, vol. 2, no. 11, pp. 1744–1752, 2017, doi: 10.1021/acssensors.7b00731.

[11] G. Ko, H. Y. Kim, J. Ahn, Y. M. Park, K. Y. Lee, and J. Kim, "Graphene-based nitrogen dioxide gas sensors," *Curr. Appl. Phys.*, vol. 10, no. 4, pp. 1002–1004, 2010, doi: 10.1016/j.cap.2009.12.024.

[12] M. W. Frampton *et al.*, "Nitrogen dioxide exposure: Effects on airway and blood cells," *Am. J. Physiol. - Lung Cell. Mol. Physiol.*, vol. 282, no. 1 26-1, pp. 155–165, 2002, doi: 10.1152/ajplung.2002.282.1.l155.

[13] H. Y. Li, C. S. Lee, D. H. Kim, and J. H. Lee, "Flexible Room-Temperature NH_3 Sensor for Ultrasensitive, Selective, and Humidity-Independent Gas Detection," *ACS Appl. Mater. Interfaces*, vol. 10, no. 33, pp. 27858–27867, 2018, doi: 10.1021/acsami.8b09169.

[14] S. Giddey, S. P. S. Badwal, and A. Kulkarni, "Review of electrochemical ammonia production technologies and materials," *International Journal of Hydrogen Energy*, vol. 38, no. 34. pp. 14576–14594, 2013, doi: 10.1016/j.ijhydene.2013.09.054.

[15] D. Zhang *et al.*, "UV illumination-enhanced ultrasensitive ammonia gas sensor based on (001)TiO_2/MXene heterostructure for food spoilage detection," *J. Hazard. Mater.*, vol. 423, no. August 2021, 2022, doi: 10.1016/j.jhazmat.2021.127160.

[16] B. Timmer, W. Olthuis, and A. Van Den Berg, "Ammonia sensors and their applications - A review," *Sensors Actuators, B Chem.*, vol. 107, no. 2, pp. 666–677, 2005, doi: 10.1016/j.snb.2004.11.054.

[17] A. A. Buszewski B., Kesy M., Ligor T., "Human exhaled air analytics: biomarkers of diseases," *Biomed. Chromatogr.*, vol. 21, pp. 553–566, 2007, doi: 10.1002/bmc.835.

[18] B. I. Adamu, P. Chen, and W. Chu, "Role of nanostructuring of sensing materials in performance of electrical gas sensors by combining with extra strategies," *Nano Express*, vol. 2, no. 4, 2021, doi: 10.1088/2632-959X/ac3636.

[19] S. Singh and S. Sharma, "Temperature-Based Selective Detection of Hydrogen Sulfide and Ethanol with MoS_2 /WO_3 Composite," *ACS Omega* 2022, 7, 7, 6075–6085, doi: 10.1021/acsomega.1c06471.

[20] Y. Huang *et al.*, "High Sensitivity, Humidity-Independent, Flexible NO_2 and NH_3 Gas Sensors Based on SnS_2 Hybrid Functional Graphene Ink," *ACS Appl. Mater. Interfaces*, vol. 12, no. 1, pp. 997–1004, 2020, doi: 10.1021/acsami.9b14952.

[21] F. Perrozzi, S. M. Emamjomeh, V. Paolucci, G. Taglieri, L. Ottaviano, and C. Cantalini, "Thermal stability of WS_2 flakes and gas sensing properties of WS_2/WO_3 composite to H_2, NH_3 and NO_2," *Sensors Actuators, B Chem.*, vol. 243, no. 2, pp. 812–822, 2017, doi: 10.1016/j.snb.2016.12.069.

[22] Y. Han *et al.*, "Hierarchical WS_2-WO_3 Nanohybrids with P-N Heterojunctions for NO_2 Detection," *ACS Appl. Nano Mater.*, vol. 4, no. 2, pp. 1626–1634, 2021, doi: 10.1021/acsanm.0c03094.

[23] M. Ikram *et al.*, "Rational Design of MoS_2/C_3N_4 Hybrid Aerogel with Abundant Exposed Edges for Highly Sensitive NO_2 Detection at Room Temperature," *Chem. Mater.*, vol. 32, no. 17, pp. 7215–7225, 2020, doi: 10.1021/acs.chemmater.0c01468.

[24] T. Y. Ko *et al.*, "On-stack two-dimensional conversion of MoS_2 into MoO_3," *2D Mater.*, vol. 4, no. 1, 2017, doi: 10.1088/2053-1583/4/1/014003.

[25] S. Duraisamy *et al.* "One-Step Hydrothermal Synthesis of Phase-Engineered MoS_2/MoO_3 Electrocatalysts for Hydrogen Evolution Reaction," *ACS Appl. Nano Mater.*, vol. 4, no. 3, pp. 2642–2656, 2021, doi: 10.1021/acsanm.0c03274.

[26] Y. Liu, S. Yang, Y. Lu, N. V. Podval'naya, W. Chen, and G. S. Zakharova, "Hydrothermal synthesis of h-MoO_3 microrods and their gas sensing properties to ethanol," *Appl. Surf. Sci.*, vol. 359, pp. 114–119, 2015, doi: 10.1016/j.apsusc.2015.10.071.

[27] X. Zheng, Y. Zhu, Y. Sun, and Q. Jiao, "Hydrothermal synthesis of MoS_2 with different morphology and its performance in thermal battery," *J. Power Sources*, vol. 395, pp. 318–327, 2018, doi: 10.1016/j.jpowsour.2018.05.092.

[28] A. Chithambararaj and A. C. Bose, "Hydrothermal synthesis of hexagonal and orthorhombic MoO_3 nanoparticles," *J. Alloys Compd.*, vol. 509, no. 31, pp. 8105–8110, 2011, doi: 10.1016/j.jallcom.2011.05.067.

[29] A. Liu *et al.*, "The gas sensor utilizing polyaniline/MoS_2 nanosheets/SnO_2 nanotubes for the room temperature detection of ammonia," *Sensors Actuators, B Chem.*, vol. 332, pp. 129444, 2021, doi: 10.1016/j.snb.2021.129444.

[30] N. T. Thang *et al.*, "Controlled synthesis of ultrathin MoS_2 nanoflowers for highly enhanced NO_2 sensing at room temperature," *RSC Adv.*, vol. 10, no. 22, pp. 12759–12771, 2020, doi: 10.1039/d0ra00121j.

[31] R. Kumar *et al.*, "Growth of MoS_2–MoO_3 Hybrid Microflowers via Controlled Vapor Transport Process for Efficient Gas Sensing at Room Temperature," *Adv. Mater. Interfaces*, vol. 5, no. 10, pp. 1–9, 2018, doi: 10.1002/admi.201800071.

[32] W. Y. Ou Y, Niu W, Zhou Y, Guo Y, Gao C, "Mesoporous WS_2/MoO_3 Hybrids for High-Performance Trace Ammonia Detection.," *ACS Appl Mater Interfaces*, vol. 14, no. 34, pp. 39062–39071, 2022.

[33] R. Khatri and N. K. Puri, "Electrochemical study of hydrothermally synthesised reduced MoS_2 layered nanosheets," *Vacuum*, vol. 175, no. February, p. 109250, 2020, doi: 10.1016/j.vacuum.2020.109250.

[34] M. A. Baker, R. Gilmore, C. Lenardi, and W. Gissler, "XPS investigation of preferential sputtering of S from MoS_2 and determination of MoS_x stoichiometry from Mo and S peak positions," *Appl. Surf. Sci.*, vol. 150, no. 1, pp. 255–262, 1999, doi: 10.1016/S0169-4332(99)00253-6.

[35] D. Xiang, C. Han, J. Zhang, and W. Chen, "Gap States Assisted MoO_3 Nanobelt Photodetector with Wide Spectrum Response," *Sci. Rep.*, vol. 4, pp. 1–6, 2015, doi: 10.1038/srep04891.

[36] P. P. Kumar and V. Singh, "Effect of Precursors ' Concentration on Structural and Electronic Properties of Ammonium Ions (NH^{4+}) Intercalated 1T/2H Phase

MoS_2," vol. 30, no. October, pp. 719–723, 2023, doi: 10.56042/ijems.v30i5.6872.

[37] S. Singh, J. Deb, U. Sarkar, and S. Sharma, "MoS_2/MoO_3 Nanocomposite for Selective NH_3 Detection in a Humid Environment," *ACS Sustain. Chem. Eng.*, vol. 9, no. 21, pp. 7328–7340, 2021, doi: 10.1021/acssuschemeng.1c01527.

[38] N. M. D. Brown, N. Cui, and A. McKinley, "An XPS study of the surface modification of natural MoS_2 following treatment in an RF-oxygen plasma," *Appl. Surf. Sci.*, vol. 134, no. 1–4, pp. 11–21, 1998, doi: 10.1016/S0169-4332(98)00252-9.

[39] L. Cai *et al.*, "Highly sensitive H_2 sensor based on PdO-decorated WO_3 nanospindle p-n heterostructure," *Int. J. Hydrogen Energy*, vol. 45, no. 55, pp. 31327–31340, 2020, doi: 10.1016/j.ijhydene.2020.08.109.

[40] S. Sharma, A. Kumar, N. Singh, and D. Kaur, "Excellent room temperature ammonia gas sensing properties of n-MoS_2/p-CuO heterojunction nanoworms," *Sensors Actuators, B Chem.*, vol. 275, pp. 499–507, 2018, doi: 10.1016/j.snb.2018.08.046.

[41] L. Wang *et al.*, "Enhanced sensitivity and stability of room-temperature NH_3 sensors using core-shell CeO_2 nanoparticles@cross-linked PANI with p-n heterojunctions," *ACS Appl. Mater. Interfaces*, vol. 6, no. 16, pp. 14131–14140, 2014, doi: 10.1021/am503286h.

[42] D. Zhang, C. Jiang, and Y. Sun, "Room-temperature high-performance ammonia gas sensor based on layer-by-layer self-assembled molybdenum disulfide/zinc oxide nanocomposite film," *J. Alloys Compd.*, vol. 698, pp. 476–483, 2017, doi: 10.1016/j.jallcom.2016.12.222.

[43] J. Bai *et al.*, "Flower-like MoS_2 hierarchical architectures assembled by 2D nanosheets sensitized with SnO_2 quantum dots for high-performance NH_3 sensing at room temperature," *Sensors Actuators B Chem.*, vol. 353, no. November 2021, 2022, doi: 10.1016/j.snb.2021.131191.

[44] S. Singh, S. Sharma, R. C. Singh, and S. Sharma, "Hydrothermally synthesized MoS_2-multi-walled carbon nanotube composite as a novel room-temperature

ammonia sensing platform," *Appl. Surf. Sci.*, vol. 532, 2020, doi: 10.1016/j.apsusc.2020.147373.

[45] S. Singh, J. Deb, U. Sarkar, and S. Sharma, "MoS_2/WO_3 Nanosheets for Detection of Ammonia," *ACS Appl. Nano Mater.*, vol. 4, no. 3, pp. 2594–2605, 2021, doi: 10.1021/acsanm.0c03239.

[46] P. P. Kumar, S. Kumar, M. Kumar, and V. Singh, " Utilization of Active Carbon Black with SnO_2 /MoS_2 Nanocomposites for the Efficient Detection of NO_2 Molecules ," *IEEE Sens. J.*, vol. 23, no. 23, pp. 1–1, 2023, doi: 10.1109/jsen.2023.3326495.

[47] M. Ikram, H. Lv, Z. Liu, K. Shi, and Y. Gao, "Hydrothermally derived p-n MoS_2-ZnO from p-p MoS_2-ZIF-8 for an efficient detection of NO_2 at room temperature," *J. Mater. Chem. A*, vol. 9, no. 26, pp. 14722–14730, 2021, doi: 10.1039/d1ta03578a.

[48] Y. Han *et al.*, "Design of Hetero-Nanostructures on MoS_2 Nanosheets to Boost NO_2 Room Temperature Sensing," *ACS Appl. Mater. Interfaces*, vol. 10, no. 26, pp. 22640–22649, 2018, doi: 10.1021/acsami.8b05811.

[49] S. Park, H. Ko, S. Kim, and C. Lee, "Role of the interfaces in multiple networked one-dimensional core-shell nanostructured gas sensors," *ACS Appl. Mater. Interfaces*, vol. 6, no. 12, pp. 9595–9600, 2014, doi: 10.1021/am501975v.

[50] S. Kumar *et al.*, "Nanocomposites of Quasicrystal Nanosheets and MoS_2 Nanoflakes for NO_2 Gas Sensors," *ACS Appl. Nano Mater.*, vol. 6, no. 7, pp. 5952–5962, 2023, doi: 10.1021/acsanm.3c00346.

[51] A. V. Moholkar, A.A. Mane, "Orthorhombic MoO_3 nanobelts based NO_2 gas sensor," *Appl. Surf. Sci.*, vol. 405, pp. 427–440, 2017, doi: 10.1016/j.apsusc.2017.02.055.

[52] D. Sahoo, B. Kumar, J. Sinha, S. Ghosh, S. S. Roy, and B. Kaviraj, "Cost-effective liquid phase exfoliation of MoS_2 nanosheets and photocatalytic activity for wastewater treatment enforced by visible light," *Sci. Rep.*, vol. 10, no. 1, pp. 1–12, 2020, doi: 10.1038/s41598-020-67683-2.

[53] Z. Yuan, Y. Liu, J. Zhang, F. Meng, and H. Zhang, "Rose-Like MoO_3/MoS_2/rGO Low-Temperature Ammonia Sensors Based on Multigas Detection Methods," *IEEE Transactions on Instrumentation and Measurement,* vol. 70, pp. 9506109, 2021, doi: 10.1109/TIM.2021.3060566.

[54] S. Singh, R. M. Sattigeri, S. Kumar, P. K. Jha, and S. Sharma, "Superior Room-Temperature Ammonia Sensing Using a Hydrothermally Synthesized MoS_2/SnO_2 Composite," *ACS Omega*, vol. 6, no. 17, pp. 11602–11613, 2021, doi: 10.1021/acsomega.1c00805.

[55] D. R. Miller, S. A. Akbar, and P. A. Morris, "Nanoscale metal oxide-based heterojunctions for gas sensing: A review," *Sensors and Actuators, B: Chemical*, vol. 211. pp. 569–570, 2015, doi: 10.1016/j.snb.2015.02.086.

Chapter – 6

Conclusion and Future Prospectives

CHAPTER – 6

CONCLUSION AND FUTURE PROSPECTIVES

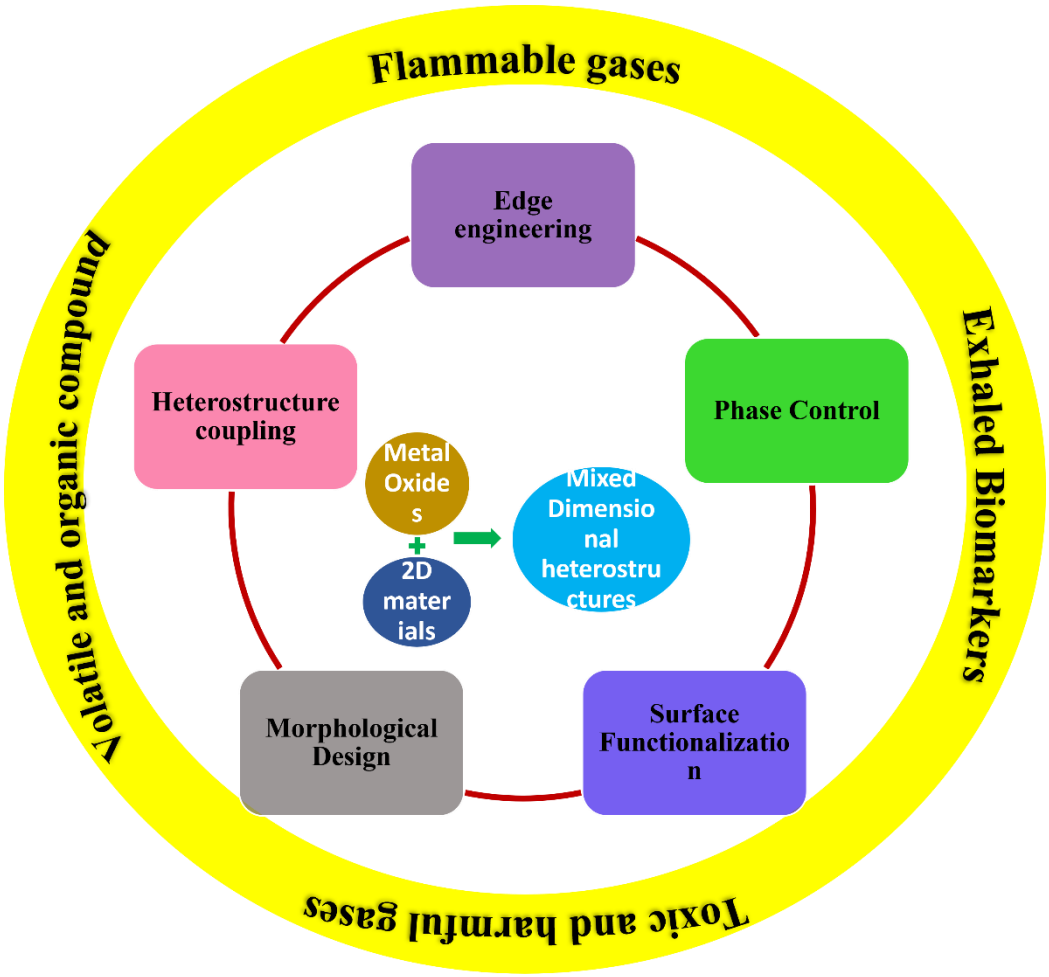

The main aim of this chapter is to summarize the outcomes of the research work carried out to fulfill the objectives of the thesis. This chapter highlights the key observations, findings, and conclusions that emerged during the research. The prospects and directions that have been concluded as a result of the research have been explored in the following section of this chapter, which will be a decisive plan of action for us.

6.1 Conclusions

This present thesis focuses on the synthesis of MoS_2 (Molybdenum disulfide) nanostructures and their use in gas sensing systems. Throughout this work, we have demonstrated the significance of different nanostructures such as metal oxides incorporated

with MoS_2 to improve the gas sensing performance of MoS_2-based gas sensors. We have shown that combinations of these nanostructures to MoS2 increase its performance for gas sensors in ambient conditions without any external aid. In this study, we have successfully fabricated heterostructures that provided gas sensing performance for both NO_2 and NH_3 gas simultaneously near room temperature. When compared to the individual impacts, the heterostructure systems perform much better. The main outcomes obtained from this investigation will be expanded in the following parts:

1. The hydrothermal technique has been mainly used for the synthesis of MoS_2 and various heterostructures such as 1T/2H-MoS_2, SnO_2/MoS_2, and CB/SnO_2/MoS_2. Thermal chemical vapor deposition has also been employed at certain stages of the synthesis part to obtain the desired nanostructures such as CB and MoS_2/MoO_3 using thermal annealing. Detailed structural, morphological, and chemical studies have been investigated using XRD, Raman, SEM, TEM, and XPS techniques.

2. The effect of precursors' concentration on the synthesis and characteristics of 1T/2H-MoS_2 has been studied. It was found that during the synthesis of MoS_2, reaction time, precursors' concentration, and precursors used during reaction play a vital role and are responsible for the variation in the electronic and chemical properties of the resultant. By varying the concentration of the ammonium molybdate tetrahydrate, the difference in the morphology, and bandgap has been observed with the appearance of the mixed phase of MoS_2. The concentration has been increased in the order of 1 M, 1.4 M, and 1.8 M. With the increase in concentration, NH^{4+} intercalation is also observed to be increased. The morphology has changed from separated flower and pin-like structure to agglomerated bundles and an increase in absorbance has appeared due to an increase in metallic character in the mixed 1T/2H-MoS_2. For 1.8 M, the absorbance is higher and the bandgap has reduced from 1.9 eV to 1.5 eV. From the XPS studies, it has been observed that when the precursor concentration increased from 1 to 1.8 M, the 1T character has developed from 27.9 % to 45.8 % respectively. As a result of an increase in concentrations, the incomplete

sulfurization of Mo precursor has also been observed. From the obtained results, this study concluded a feasible, economical approach to synthesize a stable mixed phase of 1T/2H-MoS_2 using NH^{4+} intercalation, which can further be utilized in the gas sensing application.

3. To further understand the role of hybridization/heterostructures, we have fabricated SnO_2/MoS_2 and $CB/SnO_2/MoS_2$ heterostructures on the MoS_2 surface. The variation in the gas sensing performance of various synthesized heterostructures-based sensors has been studied and compared with pristine MoS_2 gas sensors. It was found that the gas sensing response of $CB/SnO_2/MoS_2$-based gas sensor has greatly enhanced in comparison to pristine MoS_2 and SnO_2/MoS_2 for NO_2 gas around room temperature. The $CB/SnO_2/MoS_2$-based gas sensor achieved a sensing response of around 46% with 26 s of recovery time which is much shorter than the pristine MoS_2 gas sensor showing a sensor response of around 40 % with a response time of 61 s for 50 ppm of NO_2 gas. The improved sensing response of the fabricated $CB/SnO_2/MoS_2$-based sensor is due to the larger exposed surface area and increase in the number of active sites available on the sensing layer surface, which play a prominent role in the higher amount of gas adsorption on the surface, result in an increased sensing response. In addition, the higher electrical conductivity of CB in comparison to the SnO_2 and MoS_2 and the formation of p-n heterojunction at the interface increase the charge transport mechanism causing a dramatic decrease in the potential barrier width, which amplifies the gas sensing properties in the ternary composite $CB/SnO_2/MoS_2$.

4. To further determine the efficiency of the MoS_2-based gas sensor, MoS_2/MoO_3 nanostructures were synthesized using different reducing agents with a hydrothermal method followed by thermal annealing at 500˚C in an Ar environment for 1 h. Hydrazine Hydrate (HH) and L-ascorbic acid (LA) were used as the reducing agents and the synthesized materials were compared with the sample prepared without using any reducing agent. In this chapter, the dual gas detection for NH_3 and NO_2 gas of the synthesized

materials (MoS_2:MoO_3, HH-MoS_2:MoO_3, and LA-MoS_2:MoO_3) has been obtained. The gas sensing performance of the MoS_2-based gas sensors for NH_3 gas has considerably improved with the incorporation of MoO_3 nanoparticles. MoS_2:MoO_3 showed a good recovery for NH_3 (52 % with 28 s response time) and NO_2 gas (37 % with 56 response time) at 50 ˚C with a better sensor response in comparison to HH- and LA-MoS_2:MoO_3. It has already been proven that the interaction of gas molecules on the upper surface of the gas-sensing material stimulates the sensor's gas response. The XPS spectra indicated that HH-MoS_2:MoO_3 has more oxygen vacancies and contains more adsorption sites, implying fast adsorption resulting in a higher sensing response but less desorption from the oxygen sites results in incomplete recovery. In the case of NO_2 gas sensing, LA-MoS_2:MoO_3 showed a higher response for NO_2 gas. Besides the better relative responses, LA- and HH-MoS_2:MoO_3-based sensors faced the same issue related to incomplete recovery due to the less desorption of NO_2 molecules. Under the exposure of NH_3 gas, the resistance decreased indicating the n-type behaviour. Ideally, when the same material should come in contact with the gas, the conductivity behavior should be the same. But in our case, when the prepared materials were exposed to NO_2 gas, the resistance decreased indicating the p-type behavior. This major difference in conductivity has been caused by the different adsorption sites playing the role of conductive channels for different gases. The distinct adsorption sites for NH_3 and NO_2 on the surface of the sensing material have appeared due to the difference in the conducting behavior, which maybe the cause of this unusual behavior. The resistance variation revealed that MoO_3 dominated the NH_3 gas sensing process in composites, instead of MoS_2. The enhanced NH_3-sensing performance was related to the superposition effect induced by hetero-interface and surface modification. However, the higher amount of O_v and $O_2^{-}{}_{(ads.\ sites)}$ in HH-MoS_2:MoO_3 and LA-MoS_2:MoO_3 unfavorably resulted in accumulation on the MoO_3 surface, making it more difficult to desorb from the MoO_3 surface, resulting in dissatisfied sensitivity and incomplete recovery despite having enhanced sensor response concerning MoS_2:MoO_3.

6.2 Scope for Future Work

1. The selection of material and the geometry of the fabricated gas sensors is very crucial to effectively utilize the gas sensor for different applications including biomedical, environmental monitoring, smart homes, and wearable sensors etc. To achieve the specific outcome for a particular application, various crucial parameters, such as stability, flexibility, humidity resistance, limit of detection, and operating temperature need to be taken care of wisely, hence further studies are required.
2. For a gas sensor, the exposed surface area is very important for gas adsorption. With the change in surface morphologies with small-sized flakes such as quantum dots, the number of active sites available on the surface also changes, resulting in variation in gas adsorption sites and the charge transport between the contacts. Greater will be active sites and greater adsorption of the target gases resulting in faster charge transport causing a rise in the sensor response. These modifications can be done via synthesized thin films using ion irradiation techniques for uniform deposition with controlled thickness of the sensing material.
3. In the present work, we have enhanced the sensor performance of the MoS_2 by combining the other phases of MoS_2 or other 2D metal oxide structures. There is a plethora of 2D materials, so there is a vast scope to enhance the performance by metal doping, MXenes, silicene, etc. Integrated gas phase synthesis is very efficient in synthesizing various core-shell nanoparticles. The enhancement in the gas sensing performance of the 2D materials as a function of the size of the metal nanoparticles incorporated on its surface can further be studied.
4. In this work, the response and recovery times are relatively sluggish for implementation in practical applications. Further work should be conducted to minimize the response and recovery time with better sensing response using a practical setting, for example, injecting a gas into a chamber for a shorter duration to mimic the real environment.

BIO-DATA

Priya is a research scholar at Delhi Technological University, Delhi pursuing her research in the Department of Applied Physics since December 2018. Before this, she completed her Master's in Physics from the Department of Physics, Central University of Haryana, Jant-Pali, Mahendergarh (Haryana) in the year 2018 and her Bachelor of Science from Miranda House, University of Delhi, New Delhi in the year 2015. She was a recipient of a Junior Research Fellowship (January 2019- December 2022) from the Delhi Technological University, Delhi. Her research interests include the synthesis and development of two-dimensional materials and devices for environmental gas-sensing applications.